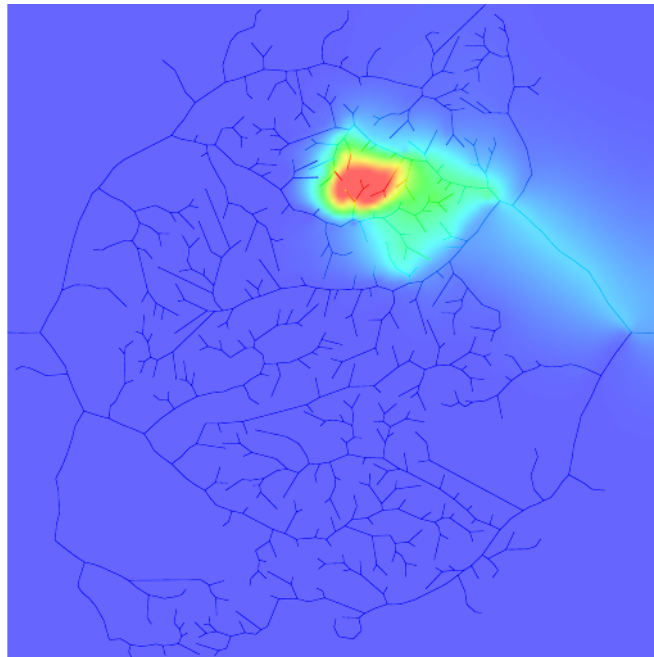


Universität Duisburg–Essen, Campus Duisburg  
Institut für Mathematik

**Diplomarbeit**

**Numerical Simulation  
of  
Transport and Diffusion  
in  
Drainage Media**

Lars Ole Schwen



corrected reprint  
April 1, 2010

## **Abstract**

In this thesis we develop the numerical tools to simulate heat diffusion in a tissue domain (liver) with a pair of blood vessel trees, coupled with heat advection through these vessels. This problem arises as part of the simulation of radio-frequency ablation of tumors.

We develop our methods for a two-dimensional geometry to keep testing and visualization simple while being able to focus on the numerical properties of the methods. Since planar organs are a purely artificial problem, we first need to generate suitable geometries which can be used for our computations.

Then we first consider the problem of heat diffusion in the tissue while the vessel trees are viewed as stationary sources of energy. We use finite elements to numerically solve this problem. Next we present a method to simulate advection in the vessel trees while the surrounding tissue is viewed as a stationary source. For this problem, we develop and use an ELLAM scheme. Finally, these two processes are coupled such that conservation of energy is locally satisfied.

## **Zusammenfassung**

In der vorliegenden Arbeit entwickeln wir Werkzeuge zur numerischen Simulation von Wärmediffusion in einem Gebiet von (Leber-)Gewebe, das von einem Paar von Blutgefäß-Bäumen durchsetzt ist, gekoppelt an Wärmetransport durch diese Blutgefäße. Dieses Problem tritt auf als Teil der Simulation von Radiofrequenz-Ablation von Tumoren.

Wir entwickeln diese Methoden für eine zweidimensionale Geometrie, um die Visualisierung und das Testen einfach zu halten und uns konzentrieren zu können auf die numerischen Eigenschaften der Methoden. Da ebene Organe ein rein künstliches Problem sind, müssen wir zunächst eine für unsere Rechnungen passende Geometrie generieren.

Dann betrachten wir zuerst das Problem der Wärmeleitung im Gewebe, wobei die Blutgefäße als stationäre Energiequelle angesehen werden. Um dieses Problem numerisch zu lösen, benutzen wir finite Elemente. Anschließend präsentieren wir eine Methode zur Simulation des Transportes durch die Gefäßbäume, wobei das umgebende Gewebe als stationäre Quelle angesehen wird. Für dieses Problem entwickeln und benutzen wir ein ELLAM-Verfahren. Schließlich werden diese beiden Prozesse so gekoppelt, dass lokal Energieerhaltung erfüllt ist.



# Contents

<b>1</b>	<b>Introduction</b>	<b>5</b>
1.1	Medical Background . . . . .	5
1.2	Our Model . . . . .	5
<b>2</b>	<b>Vessel Trees in 2D</b>	<b>7</b>
2.1	Notation . . . . .	7
2.2	Computer Generation of Vessel Trees . . . . .	10
2.3	Implementation of Vessel Trees . . . . .	18
2.4	Vessel Trees and Grids . . . . .	19
2.5	Determining Flow Splitting Ratios . . . . .	19
<b>3</b>	<b>Heat Conduction in Tissue</b>	<b>31</b>
3.1	Continuous and Weak Problem . . . . .	31
3.2	Discretization . . . . .	33
3.3	Steady State . . . . .	36
3.4	Implementation and Results . . . . .	38
<b>4</b>	<b>Advection in Vessel Trees</b>	<b>43</b>
4.1	Continuous and ELLAM Formulation . . . . .	44
4.2	ELLAM on a Single Segment . . . . .	52
4.3	ELLAM on Bifurcations . . . . .	62
4.4	Treatment of Terminal Segments . . . . .	84
4.5	ELLAM on Vessel Trees . . . . .	90
<b>5</b>	<b>Coupling Transport and Diffusion</b>	<b>97</b>
5.1	Problem Formulation . . . . .	97
5.2	Heating by the RF Probe . . . . .	103
5.3	Implementation and Results . . . . .	104
<b>6</b>	<b>Mathematical Background</b>	<b>117</b>
6.1	Numerical Integration . . . . .	117
6.2	Sobolev Spaces . . . . .	118
6.3	Finite Elements . . . . .	123
<b>7</b>	<b>Conclusions and Outlook</b>	<b>125</b>

## *Contents*

# 1 Introduction

## 1.1 Medical Background

The treatment of liver carcinoma is an important problem in medicine. A standard technique is surgical resection, but it can be problematic as entire segments of the liver may need to be removed, in many cases it is even impossible due to the size or location of the tumor relative to the key vessel [34].

A schematic image of a human liver (from [20]) is shown in Figure 1.1.

Minimally invasive RF ablation is an alternative: An *RF probe* consisting of two electrodes is inserted into the organ, it uses AC current of about 500 kHz. This current leads to a heating due to the Ohm resistance of the tissue. At a temperature of about 320 K (45 – 50 °C), intracellular proteins denature and cell membranes are destroyed [34, 25, 26].

A more complex RF probe (from [34]) is shown in Figure 1.2.

The problem with this method of treatment is that strictly local heating is not possible, thermal energy is distributed to regions other than the tumor by heat conduction through the tissue and blood flow through blood vessels. One is interested in optimizing the treatment such that the tumor is destroyed but damage to the surrounding organ is minimized, for this purpose, simulations of the heat distribution are necessary.

The setting is schematically shown in Figure 1.3 where an RF probe is inserted into a tumor located near a bifurcating blood vessel. This image was taken from [25].

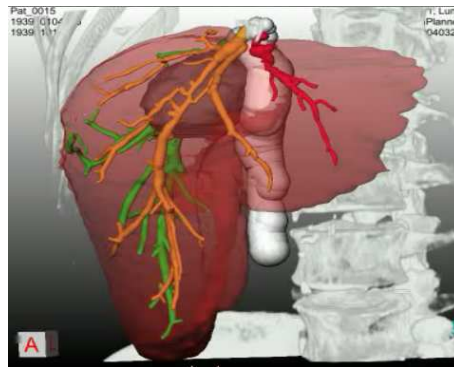


Figure 1.1: Schematic image of a human liver with blood vessels, from [20].

## 1.2 Our Model

We present a two-dimensional model of part of the physical effects involved. The model involves a square domain of tissue with an arterial and a venous vessel tree, binary trees consisting of one-dimensional straight line segments that are self- and mutually intersection free.

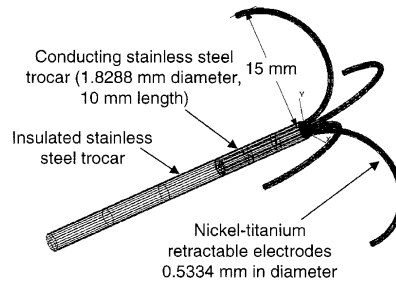


Figure 1.2: Structure of a four-tine RF probe for hepatic tumor ablation, from [34].

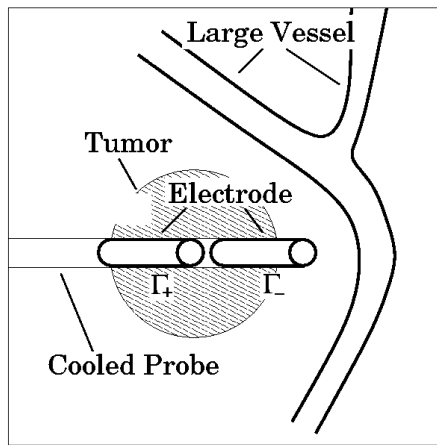


Figure 1.3: Schematic sketch of an RF probe inserted into a tumor near a large blood vessel, from [25].

Tissue and vessels are viewed as one closed system with respect to energy. We have inflow and outflow of blood through the root segments of the two vessel trees and external heating of the tissue (but not the vessels) by the RF probe. Internally, we model heat conduction (but no blood flow) in the tissue and blood flow but no heat conduction in the vessel trees. Between those two geometries, heat conduction between tissue and the non-terminal segments of the vessel trees and outflow / inflow along the terminal segments of the trees into / out of the tissue will be modeled.

For the tissue domain, we have a two-dimensional diffusion problem with Neumann boundary values and both area (probe heating) and line sources (heat exchange with the vessels), for the vessel trees, we have one-dimensional advection with line sources on a branching structure.

A suitable geometry, that is a pair of vessel trees within a square two-dimensional domain of tissue, does not appear in nature, so the first step towards our simulation is to generate such vessel trees. The trees are generated to obtain a homogeneous supply of blood for the tissue to some extent, velocities of blood flow through the individual segments are balanced to minimize the dissipation of kinetic energy in the tissue.

## 2 Vessel Trees in 2D

In this chapter, we introduce notation for vessel trees, explain how suitable data structures for such trees can be implemented and what tools we need to discretize the individual segments of the trees compatible to a rectangular discretization of the underlying tissue domain.

Then, we present a method to generate two-dimensional vessel trees suitable for our purposes. This involves two optimization procedures.

### 2.1 Notation

#### 2.1.1 Binary trees

We use the notation of [28] for binary trees that describe the topological structure of our vessel trees.

**Definition 2.1.1.** A *directed graph* is a pair  $(N, A)$  with the following properties:

1.  $N$  is a finite, nonempty set,
2.  $\emptyset \neq A \subset N \times N$  and
3.  $a = (k_i, k_t) \in A \implies k_i \neq k_t$ .

The elements  $k$  of  $N$  are called *nodes*, the elements  $a$  of  $A$  are called *arcs*. If  $a = (k_i, k_t) \in A$ ,  $k_i$  and  $k_t$  are the *initial* and *terminal node*, respectively.

**Definition 2.1.2.** The *multiplicity* of a node  $k \in N$  in a directed graph  $(N, A)$ ,  $m(k)$ , is defined to be the number of arcs leaving  $k$ :

$$m(k) := |\{a \in A \mid a = (k, \tilde{k}) \text{ for some } \tilde{k} \in N\}|$$

**Definition 2.1.3.** If  $k$  is a node,  $p$  is a segment with terminal node  $k$  and  $d$  is a segment with initial node  $k$ ,  $p$  is called the *parent segment* of  $d$ ,  $d$  is called the *daughter segment* of  $p$ .

If  $d$  and  $e$  are the two distinct segments with the same initial bifurcation node  $k$ , they are called *siblings*.

**Definition 2.1.4.** A (positive) *path* from  $k_0 \in N$  to  $k_r \in N$  is a  $P = (k_0, a_1, k_1, a_2, \dots, a_r, k_r)$  where  $k_\rho \in N \forall \rho = 0, \dots, r$  and  $a_\rho = (k_{\rho-1}, k_\rho) \in A \forall \rho = 1, \dots, r$ .

**Definition 2.1.5.** A *binary tree* is a directed graph satisfying:

1. there is exactly one node  $r \in N$  called *root* that has no incoming arc: there is no  $\tilde{k} \in N$  with  $(\tilde{k}, r) \in A$ ,
2. for each node  $k \in N$ , there is a unique path from the root  $r$  to  $k$ ,

3. each node  $k \in N$  has multiplicity at most two

*Remark 2.1.6.* 2. implies that the tree is connected, 3. means that there are no multifurcations, at most bifurcations.

There are three possible values for the multiplicity of a node  $k$ :

1.  $m(k) = 0$ : leaves
2.  $m(k) = 1$ : intermediate nodes that may be used for subdividing arcs
3.  $m(k) = 2$ : bifurcation nodes

Bifurcations are denoted by  $(p \prec d, e)$  or  $(d, e \succ p)$  if  $p$  is the parent and  $d, e$  are the daughters, depending on the type of tree (see below).

### 2.1.2 Geometric Binary Trees

Other than the purely topological information of a binary tree, we also need to store geometric information and further data for the nodes and arcs. We now describe the data structure necessary for this as well as further geometric restrictions. Part of the terminology here is based on [17].

**Definition 2.1.7.** A *node* in the context of vessel trees is a node that has two coordinates  $x, y \in \mathbb{R}$ , its location, and a level  $l \in \mathbb{N} \cup \{0\}$ .

The *level* is the number of bifurcation points on the (unique) path from the root (included when counting) to the node (not included when counting), the root always has level 0.

**Definition 2.1.8.** A *segment* of a vessel tree is an arc that is viewed as a one-dimensional closed line segment (i. e. containing initial and terminal point) from its initial node to its terminal node. In some situations (where necessary from a physical point of view), we view the segment as a two-dimensional object, so we assign a radius  $r \in [0, \infty)$ . As we consider flows through the vessel trees, we assign a constant velocity  $v \in [0, \infty)$  to the segment.

Later, we assign one-dimensional grids to each segment to discretize functions on the segment.

**Definition 2.1.9.** A *terminal node* is a leaf in a vessel tree, a *terminal segment* is a segment terminating in a leaf.

Note that level and generation are different concepts: Along a path in the tree, generation (of segments) strictly increases whereas level (of nodes) increases at bifurcation nodes but stays constant at intermediate nodes.

### 2.1.3 Vessel Trees

We only consider binary trees for which the root node has multiplicity one, i. e. there is a unique *root segment*.

**Definition 2.1.10.** A *vessel tree* is a binary tree with root node of multiplicity one for which nodes and segments have the additional data described above and for which no two segments intersect geometrically except for connected segments that may (and do) intersect at the connecting point. We consider an *arterial tree* and a *venous tree*.

In the arterial tree, blood flow is directed from the root to the leaves, in the venous tree, it is directed from the leaves to the root node. This explains why we do not allow negative velocities.

A tree with  $n$  terminal segments is called  $n$ -tree for short.

We identify a tree with the union of its segments indexed in such a way that the root node always has index 0 and the root segment always has index 0 as well:  $T = \bigcup_i S_i$ .

Moreover, the tree of arteries,  $T_a$ , and the tree of veins,  $T_v$ , in our model may not touch at all, not even in a single (connection) point. This means  $T_a \cap T_v = \bigcup_i S_{a_i} \cap \bigcup_j S_{v_j} = \emptyset$ . This is called a *valid pair of trees*.

For a segment  $s$  (or with index  $s$ , this will be clear from the context), we write

- $r_s$  for its radius
- $A_{\emptyset,s}$  for its *cross section area* (in 2D, this is the *diameter*:  $A_{\emptyset,s} = 2r_s$ ).
- $\ell_s$  for its length
- $v_s$  for the velocity of its blood flow
- $\theta_s = \frac{v_s A_{\emptyset,s}}{v_p A_{\emptyset,p}}$  for the *flow splitting ratio* from parent segment  $p$  to  $s$ .

Later in Chapter 4, we want to treat vessel trees as one-dimensional objects, despite their branching structure. For this purpose, we identify a vessel tree with a finite union of closed intervals in  $\mathbb{R}$ :

Let  $T = \bigcup_i S_i$ ,  $K \in \mathbb{N} : K > l_i \forall i$ , then identify  $T$  with  $\bigcup_i [iK, iK + \ell_i]$ . On an arterial tree,  $iK$  corresponds to the initial node of arc  $i$ , on a venous tree,  $iK$  corresponds to the terminal node of segment  $i$ . This representation is shown in Figure 2.1. The connectivity structure of the tree is then represented by relations between boundary points.

In case of the arterial tree, we consider a flow from the root to the leaves with splitting at bifurcations ( $p \prec d, e$ ), for the venous tree, flows originate at the leaves and flow towards the root being combined at bifurcations ( $d, e \succ p$ ).

Let  $f : T \rightarrow \mathbb{R}$  be a function defined on the arterial tree and ( $p \prec d, e$ ) be a bifurcation, then there is some relation between

$$\begin{aligned} f(p_{\text{term}}) &= f(pK + \ell_p), \\ f(d_{\text{init}}) &= f(dK) \text{ and} \\ f(e_{\text{init}}) &= f(eK) \end{aligned}$$

that is typically derived from some physical conservation law.  $p_{\text{term}}$  denotes the terminal node of  $p$ , similarly  $d_{\text{init}}$  and  $e_{\text{init}}$  are the initial nodes of  $d$  and  $e$ . This is the same (bifurcation) node viewed as part of each of the segments.

We use the same notation for both representations of trees,  $f : T \subset \mathbb{R}^2 \rightarrow \mathbb{R}$  and  $f : T \subset \mathbb{R} \rightarrow \mathbb{R}$ .

In case of a bifurcation ( $d, e \succ p$ ) in the venous tree, relations are between

$$\begin{aligned} f(p_{\text{term}}) &= f(pK), \\ f(d_{\text{init}}) &= f(dK + \ell_d) \text{ and} \\ f(e_{\text{init}}) &= f(eK + \ell_e). \end{aligned}$$

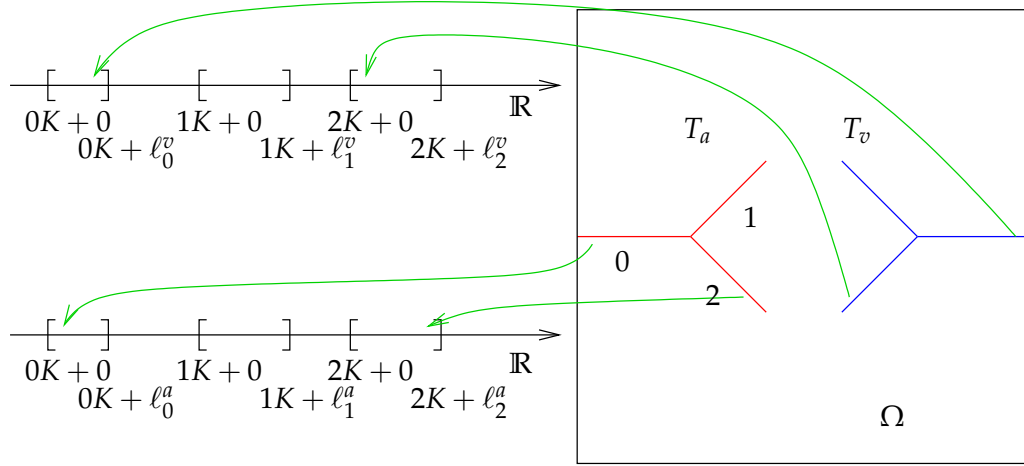


Figure 2.1: Tissue, vessels and one-dimensional representation of the vessel trees used for our computations.

Note that initial and terminal node refer to the connectivity structure of the tree and parent segments always terminate in a bifurcation node whereas the 1D interval representation is different on arterial and venous tree.

Under the identification above, we have a mapping  $\psi$  of coordinates between 1D and 2D as follows:

$$\begin{aligned} \psi : (x, y) &\mapsto \Lambda = K \cdot s + \lambda \quad s \in \mathbb{N}, \lambda \in [0, \ell_s] \\ \psi^{-1} : \Lambda = K \cdot s + \lambda &\mapsto (x, y) \end{aligned} \tag{2.1}$$

such that

$$\begin{bmatrix} x \\ y \end{bmatrix} = k_{s,\text{init}} + \lambda(k_{s,\text{term}} - k_{s,\text{init}}).$$

For  $\psi$  to be uniquely defined on bifurcation points, we view a bifurcation point as part of the parent segment and not of the daughters<sup>1</sup>.

Values that are constant for each segment can then be viewed as functions constant on the corresponding intervals.

For our computations we use the setting shown in Figure 2.1: a valid pair of arterial tree and venous tree branching into the domain  $\Omega = [0, 1]^2$  from the left respectively the right boundary.

## 2.2 Computer Generation of Vessel Trees

Figure 2.2 is a photograph of a tree. This shows both the motivation for defining a concept of geometric trees and a problem when dealing with a two-dimensional model.

Real-world data for vessel trees is inherently three-dimensional. In general, projection of three-dimensional trees leads to loops and taking a cross-section results in non-connectedness.

<sup>1</sup>this is consistent with the way we discretize vessel trees in Section 4.3

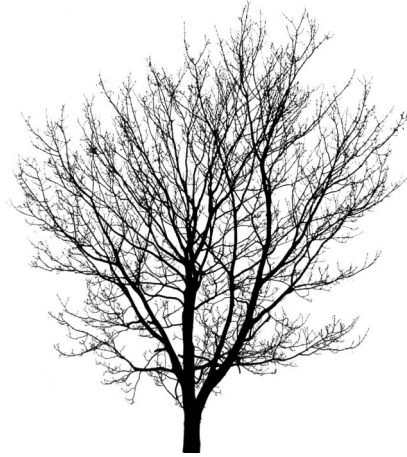


Figure 2.2: A tree in Brandenburg in winter

Leaves and very thin parts of the body (the authors of [41] mention rabbit ears, frog mesentery, rat cremaster muscles and hamster cheek pouches) may be viewed as an approximation in some sense of a two-dimensional tree, but for our purposes, we use computer-generated trees.

Schreiner, Neumann et. al. developed a method to generate a two-dimensional vessel tree in a specified domain, [30, 23], but this was a single tree only. We need to adapt their model to the case of generating a pair of trees.

Note that there is a fundamental difference from a pair of trees in three dimensions: in two dimensions, vessel segments (line segments) have codimension 1, so few segments of one tree can stop the other tree from branching into substantially large regions of the domain. In three dimensions, segments of the two trees can quite easily “wind around each other”.

### 2.2.1 Motivation for Constrained Constructive Optimization

The authors of [30] consider the problem of finding a tree that supplies a domain of tissue as homogeneously as possible with blood, minimizing the volume of the vessel tree. The root node is assumed to be lying on the boundary of the domain since supply of blood requires inflow from the outside.

Other than the root and the terminal nodes, all nodes are bifurcation nodes.

The radii of the segments satisfy the power law [40, 23]:

$$r_{\text{parent}}^3 = r_{\text{daughter 1}}^3 + r_{\text{daughter 2}}^3. \quad (2.2)$$

For real vessel segments with two-dimensional cross section area in 3D, this radius ratio leads to decreasing velocity when flow is split at bifurcations.

The radii of terminal segments are assumed to be a fixed value. This is reasonable because the authors assume homogeneous supply by a fixed number of homogeneously distributed terminal nodes.

If  $\ell_s$  is the length of a segment  $s$  and  $A_{\mathcal{O},s}$  is the cross section area, the total volume is the sum over all segments in the tree

$$\sum_s \ell_s \cdot A_{\mathcal{O},s}. \quad (2.3)$$

Analytically, this is an optimization problem:

**Proposition 2.2.1.** *Given*

- the geometric location of the root node on the boundary of the domain
- the number of terminal nodes as well as their (mutually distinct) geometric location,
- a terminal radius  $r_{\text{term}} \in \mathbb{R}$  for all terminal segments and other radii satisfying (2.2) at all bifurcations,
- a sufficiently small  $\delta \in \mathbb{R}$ ,

there is a vessel tree with bifurcations only satisfying

$$\text{dist}(s, s') \geq \delta \text{ for all (1D line) segments } s, s' \text{ that are not connected} \quad (2.4)$$

that has minimal total volume.

*Proof.* For a finite number of terminal nodes, there is only a finite number of topologies of binary geometric trees, not necessarily for all of these a valid (satisfying (2.4)) vessel tree can be found.

For sufficiently small  $\delta$ , there is at least one topology for which we get a valid vessel tree, this is shown in Lemma 2.2.2.

Fix one topology for which a valid vessel tree can be found. Then the radii (and thus the cross section areas) of the segments are can be computed by enforcing (2.2) at each bifurcation.

The total volume  $V_{\text{tot}}$  is a function of the location of the bifurcation nodes (for  $n$  terminal nodes, there are  $(n - 1)$  bifurcation nodes. The feasible set for  $V_{\text{tot}}$  is

$$\left\{ (x_1, y_1, \dots, x_{n-1}, y_{n-1}) \in \mathbb{R}^{2(n-1)} \mid \text{the tree with these bifurcation nodes satisfies (2.4)} \right\}.$$

If  $\delta$  is small enough, this set is nonempty, due to the  $\geq$  condition in (2.4) it is closed and obviously it is bounded.

Lengths of the segments depend continuously on the geometric location of the endpoints, so  $V_{\text{tot}}$  is a continuous function.

A continuous function attains its minimum on a nonempty compact set, so there is an optimal tree for the fixed topology.

So finally, we need to find a tree with minimal volume among the optimal trees for each of the finitely many topologies (need not be unique).  $\square$

**Lemma 2.2.2.** *For a finite number of nodes and a given root node, there exists a vessel tree which has exactly these nodes as terminal nodes and which satisfies the minimum distance condition in Proposition 2.2.1 for some sufficiently small  $\delta$ .*

*Proof.* The idea how to find one is given in Figure 2.3 Without loss of generality assume that the root node lies on the left boundary (otherwise rotate). First connect the root node to a rightmost node, if another nodes lies on the connecting straight line, make a detour.

Then connect all other nodes to this first line by vertical segments, again making detours whenever two or more nodes lie on a horizontal line on the same side of the first line.

Since the number of nodes is finite, it is possible to satisfy the minimum distance condition for sufficiently small  $\delta$ .  $\square$

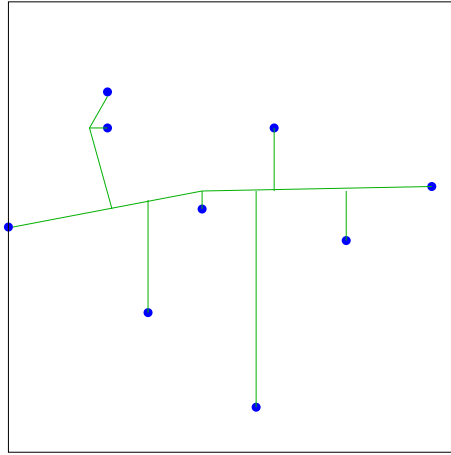


Figure 2.3: Finding a valid tree connecting a finite number of terminal nodes

Note that even for a moderate number of terminal nodes, the number of topologies becomes very large and the minimization for each fixed topology becomes quite complex, so this approach does not work in practice.

Instead, the authors use a procedure that adds terminal nodes to the tree one-by-one, each time finding an optimal bifurcation. The location of the terminal nodes is random to some extent.

### 2.2.2 CCO for a Single Tree

First we explain the method of Schreiner, Neumann et. al. [30], afterwards we will explain how we extended this procedure to generate a valid pair of vessel trees.

First, a random terminal node is chosen and connected to the root node of A by a single segment of radius  $r_{\text{term}}$ .

Further terminal nodes are added to the tree according to the following procedure:

1. Repeat choosing new random points until one is sufficiently far away from currently existing segments in the tree (the threshold is taken proportional to  $(\# \text{ segments})^{-1/2}$  and slowly decreases with each attempt of choosing a new point).

This results in a rather uniform distribution of the terminal nodes, much more uniform than if they were chosen at random.

2. For each existing segment, consider the local subtree obtained by connecting the new point to the center of the existing segment. Change the radius of the new local parent segment so that the power law (2.2) is satisfied in the subtree.

Now optimize the position of the bifurcation point to minimize the volume of the subtree. We use a *steepest descent method* with *Armijo step size rule* ([4], see Section 2.5.3) until the decrease in one step is less than some threshold (e. g. 0.1 %).

Subtracting the volume of the original segment from the volume of the optimized subtree gives a volume increase.

Looping over all segments in the tree finds a segment with least increase.

3. Now plug this back into the full tree if the tree is still valid afterwards. It is interesting to note that (as in the authors found in [30]), self-intersections do not occur. If a new connection to one segment produces an intersection with another segment, then connecting the new node to that other segment produces less increase in volume.
4. Since we only adapted the radius locally, we finally need to adapt the radii of the segments between the root and the new bifurcation point to ensure the power law for all bifurcations in the tree. Also, levels of nodes have changed, so these need to be updated as well.

Note that increasing the number of terminal nodes produces trees of similar overall geometric structure when using the same random seed. Segments added at a later stage of growth only lead to small geometric displacements of already existing segments.

### 2.2.3 CCO for a Pair of Trees

For a pair of trees, existence of an optimal tree cannot be proven as in Proposition 2.2.1. Even for mutually distinct geometric positions of nodes for both trees, there need not exist a valid pair of vessel trees having these nodes as terminal nodes.

In our generating procedure, this is no problem: If one point cannot be connected to the tree under consideration, we discard this point and try another one.

When generating a pair of arterial tree  $A$  and venous tree  $V$ , we add segments to  $A$  and  $V$  in turn. Two things need to be changed:

1. In 1, we consider the total number of segments for the threshold. The distribution of terminal nodes is not uniform in the whole domain for each tree.
2. For the first node of  $V$  and in 3, we always need to make sure that the pair of trees is remains valid. In particular,  $A$  and  $V$  must not intersect.

As we are interested in trees that branch into each other to some extent, we started our growing procedure with the initial configuration shown in Figure 2.4.

With these changes, the trees do not touch but other effects may occur:

1. long segments at an early stage of growth in one tree may stop the other tree from reaching substantial parts of the domain.
2. trees “almost touch”, i. e. arterial and venous segments have a “very small” distance, this would require a very fine discretization of the underlying tissue later on
3. segments may become “very short”, which would require a small time step later on
4. segments may become “very long”, this is unnatural for thin segments away from the root

There are two ways to avoid this: Either by postprocessing and modifying problematic segments after the generation or directly during the generation process.

As modifying the tree afterwards may have substantial side effects, we decided to use the second method and made sure that adding a new terminal node and a bifurcation to the tree

1. preserves a certain minimum distance between the two trees, the threshold is relative to the length of the arcs under consideration.

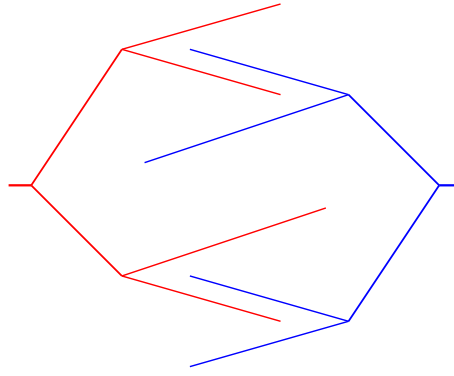


Figure 2.4: Initial tree we started the CCO growing procedure with. The arterial tree (left) is shown in red, the venous tree in blue.

2. no segment affected by the new bifurcation becomes shorter than an threshold  $\eta$ .
3. the new terminal segment is shorter than  $\frac{\text{constant}}{\sqrt{\text{number of arcs present}}}$ .

This may still lead to neighboring long segments that should be connected to minimize volume but where the connection would violate one of these conditions. However, this does not happen too often and can be tolerated for our purposes.

The pairs of trees generated by this method are still random to some extent, so we cannot expect all trees with different random seeds to look equally “nice”. So we first generate trees with 64 terminal segments for different random seeds, pick one that looks most appropriate and generate more complex trees out of this.

As for a single tree, the procedure above does not significantly change the coarse geometric structure of the trees when terminal nodes are added later on, see Figure 2.5.

As the radius of all terminal segments needs to be fixed in advance, even if we use different numbers of terminal segments, one step of postprocessing may be necessary: To obtain constant inflow and outflow of blood for different trees, we can rescale the radii of all segments at the end so that the root segment has a fixed radius. This preserves (2.2).

This is shown below in Figure 2.5. where we computed pairs of trees with 8, 16, 32, 64, and 512 terminal nodes each according to the method above, starting with the same random seed.

Computation times on a desktop PC with 1 GHz Athlon CPU are listed in Table 2.1.

A few more pairs of 64-trees generated with different random seeds are shown in Figure 2.6.

The pairs of trees generated by this procedure have a sufficiently complex and realistic structure for our purposes. As this generating procedure is not the main focus of this thesis, we did not geometric properties of a pair of trees generated by this procedure to those of real three-dimensional vessel trees in [39, 40] and we did not refine this rather crude procedure to systematically produce even more realistic trees.

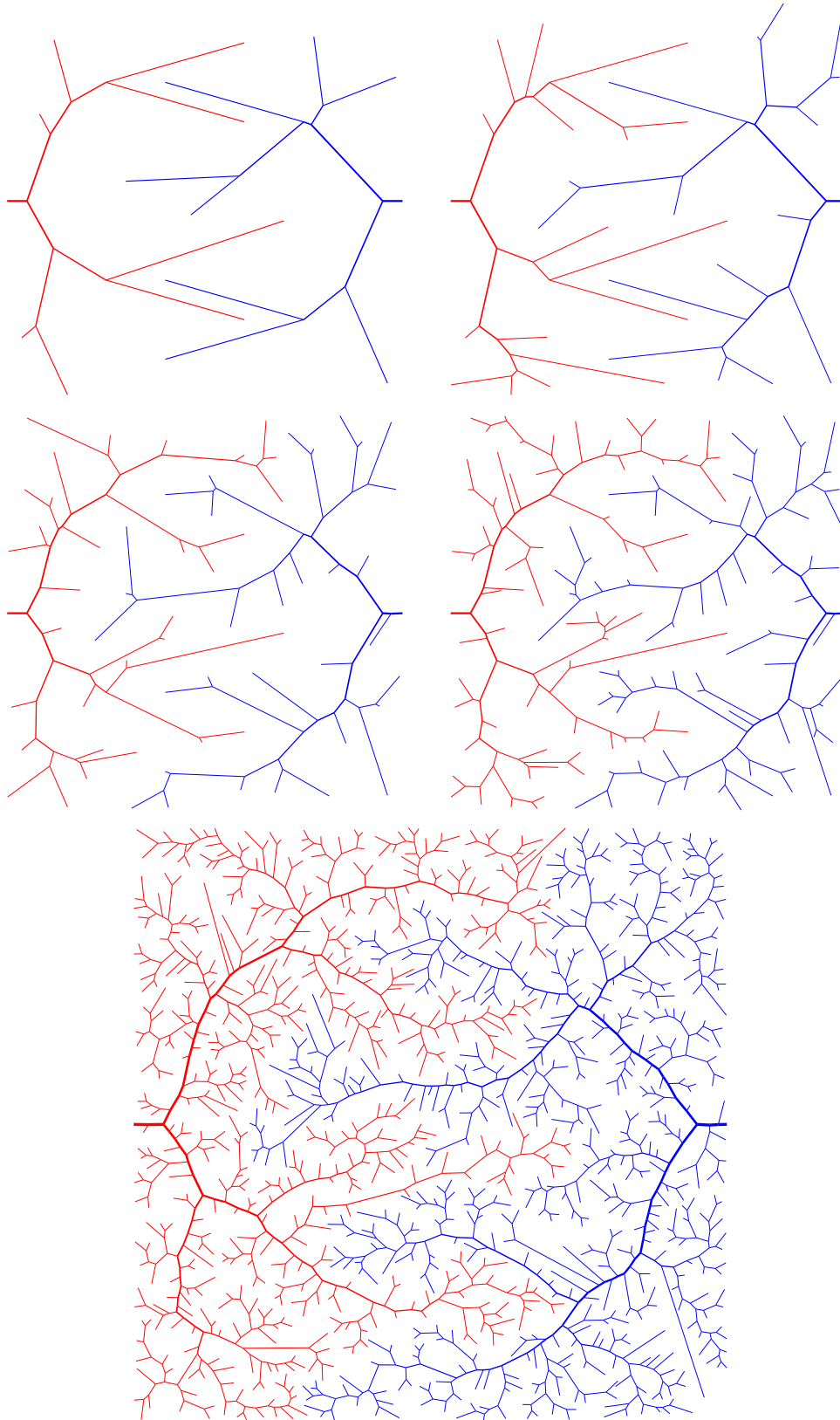


Figure 2.5: A sequence of pairs of trees with 8, 16, 32, 64 and 512 terminal segments each. Arteries are shown in red, veins in blue, thickness of the lines represents thickness of the vessels.

number of terminal segments	cputime (s)
8	0.05
16	0.50*
32	3.88
64	20.30*
128	318
512	14 580

Table 2.1: Cputime to generate pairs of vessel trees of different complexity. The starred values are approximate times.

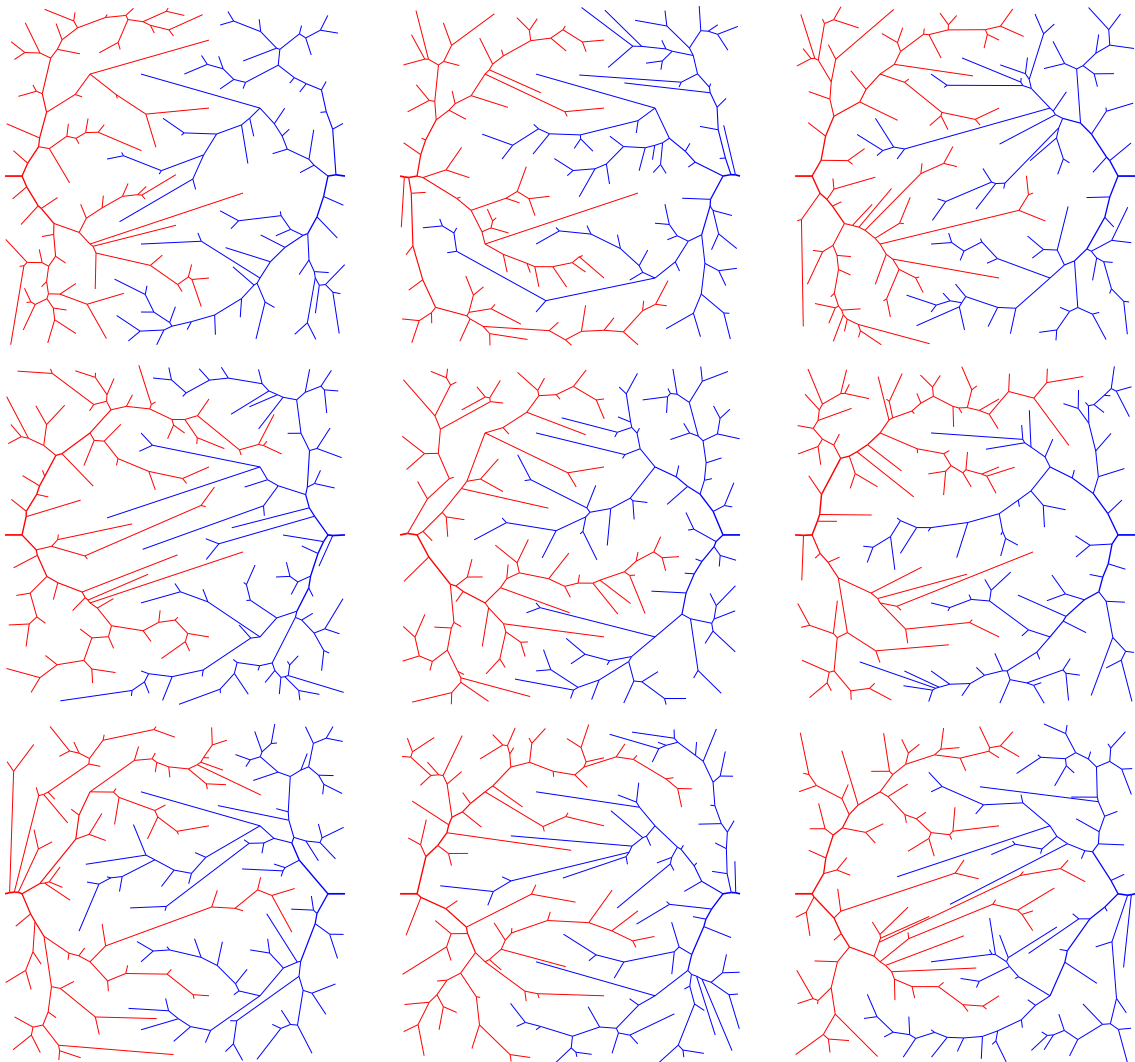


Figure 2.6: Pairs of 64-trees generated with different random seeds.

Also, few such pairs of trees are sufficient for our purposes and we do not need a large set of different trees, so we did not put much effort into optimizing the implementation of this generating procedure.

Later on, in three dimensions, we will be able to (and we will probably want to) use real-world data for the trees, see e. g. [13].

## 2.3 Implementation of Vessel Trees

### 2.3.1 Data Structures

For a geometric tree, we store an STL vector of nodes and an STL vector of arcs.

The class `node` has the following member variables:

- two floating point numbers for the coordinates of the node
- one integer for the level of the node,

the class `arc` has

- two integers for the indices of initial and terminal node
- four integers for the indices of parent, two daughter and sibling segment
- one float for the radius  $r$  of the segment
- one float for the velocity  $v$  of blood flowing through
- one float for the flow splitting ratio  $\theta$  to its parent arc, see Section 2.1.3.

and it provides functions to compute length  $\ell$  and cross section area  $A_{\emptyset}$ .

### 2.3.2 Feasibility of Arcs and Nodes

Determining whether an arc may be added to the tree or whether it intersects or gets too close to other arcs is an easy geometrical problem since we are dealing with straight line segments and the coordinates of their end points are known.

We do not explain this in detail here.

### 2.3.3 File Format

Once generated, we want to save vessel trees for later use. We use separate files for the arterial and venous tree, each file has the following format:

- first line: integer `nn`: number of nodes
- second line: integer `na`: number of segments
- next `nn` lines: two floats  $x$  and  $y$ , coordinates of the node in  $[0, 1]^2$
- next `na` lines: two integers: indices of initial node and terminal node, two floats: radius of the segment and flow velocity

The lines describing the nodes and arcs may contain further data in the line after the values described. This may be useful to store additional information like level of nodes or constant values on segments, but in this case it is necessary to use appropriate save and load routines.

Information about the level of nodes and parent, sibling and daughters of segments are redundant information if data as above is given, hence they can be computed at runtime (if necessary) and are not saved.

## 2.4 Vessel Trees and Grids

### 2.4.1 Vessel Segments and Grid Cells

In our numerical computations we have a square domain divided into grid cells together with a pair of vessel trees. We need to know which segments lie partially in a given grid cell. In this context, segments are viewed as one-dimensional objects, i. e. identified with their center lines.

For each grid cell we store a list of arcs intersecting it with the following information:

- the index of the arc intersecting the cell
- local coordinates (relative to the grid cell) of the initial node and the terminal node projected onto the grid cell along the segment. Those points are either the initial or terminal node of the segment if this node lies within the grid cell or they are the intersection points of the segment and the boundary of the grid cell.
- local coordinate (relative to the segment) of those two points

Conversely, for each segment we store a list of grid cells (grid cell indices) intersected by the segment together with the local coordinates mentioned before.

Determining the grid cells intersected by a given segment and the local coordinates of the points described above is a technical but easy geometric problem if we start at the initial node of the segment and trace which grid cells are passed on the way towards the terminal segment.

A discretization of a squared domain is of *level*  $d$  if it has  $(2^d + 1) \times (2^d + 1)$  grid points. In this case, the *grid spacing* is  $h = 2^{-d}$ .

For complex trees (512-trees) and a fine discretization of both tissue (level 7) and vessels used in Chapter 5, these lists only require some 100 kB of memory.

## 2.5 Determining Flow Splitting Ratios

In Section 2.2, we generated a pair of trees determining the geometric location of the segments and their radii. We now need reasonable velocities of the blood flow in each segment.

In [22], results about the pressure gradients in segments of 3D vessel trees can be found, [35] explains Poiseuille's law relating flow and pressure.

However, we can not simply adapt these results from 3D to 2D. If we ignore the boundary of our domain of tissue and the fact that there are regions where there are only arteries or veins, wide-range components of the flow could dominate the transport through tissue.

Our approach is to balance the flow through the vessel trees such that dissipation of kinetic energy by friction is minimized.

### 2.5.1 Model

Assume that there is a fixed inflow rate of blood, say  $c$ , into the root segment of the arterial tree equal to the outflow out of the root segment of the venous tree. Blood flows out of the arterial tree all along the terminal segments (and only these) at a constant rate on each segment, similarly it flows from the tissue into the venous tree all along the terminal segments of the venous tree (and only these) at a constant rate on each segment.

#### Pressure in a Porous Medium

We assume isotropic incompressible flow through a *porous medium* with zero Neumann boundary conditions at the outer boundary. The terminal segments (and only these) of the arterial and venous tree are 1D line sources and sinks for the flow, respectively. The diffusion coefficient is set to 1.

This is modeled by the same boundary value problem as the steady state of heat conduction, see Section 3.3. The methods used to solve this PDE numerically are better explained in that context which also is the main focus of this thesis, so we only quote results here.

Our steady state boundary value problem is to find  $p$ , the *pressure* of fluid in a porous medium, satisfying

$$\begin{aligned} -\Delta p &\stackrel{*}{=} f && \text{in } \Omega \\ \partial_\nu p &= 0 && \text{on } \partial\Omega \\ \int_{\hat{\Omega}} p &= 0 \end{aligned} \tag{2.5}$$

where  $f$  is nonzero only on the terminal segments of the arterial and venous tree and the equation is meant in a distributional sense, see Section 3.3.

The weak form of the problem with line source terms  $f \in H^{-1}(\Omega)$  is to find  $p \in V = \{v \in H^1(\Omega) \mid \int_{\Omega} v = 0\}$  such that

$$+ \int_{\Omega} \nabla p \cdot \nabla v \, dx = \int_{T_a \cup T_v} f v \, d\gamma = \int_{T_a} f_a v \, d\gamma + \int_{T_v} f_v v \, d\gamma \quad \forall v \in V \tag{2.6}$$

where  $dx$  denotes integration in  $\mathbb{R}^2$  whereas  $d\gamma$  denotes line integration along 1D lines in  $\mathbb{R}^2$ . Here,

$$f_a := f|_{T_a}, \quad f_v := f|_{T_v}$$

By assumption,  $\int_{T_a \cup T_v} f = 0$ . Requiring  $\int_{\Omega} p = 0$ , by Proposition 3.3.1, there is a unique solution  $p = -\Delta^{-1} f$ ,  $p \in H^1(\Omega)$ ,  $\int_{\Omega} p = 0$  to problem (2.6).

Let  $m, n$  be the number of terminal segments in the arterial and venous tree, respectively,  $z = m + n$ . Let

$$S = (a_1, \dots, a_m, v_1, \dots, v_n) \in \mathbb{R}^z$$

be the vector of source terms where  $a_\mu$  is the flow out of the  $\mu$ th terminal segment of the arterial tree divided by the length of the segment (similarly  $v_\nu$  the flow into the  $\nu$ th terminal segment of the venous tree divided by the length of the segment).

$$l_a = (\ell_1^a, \dots, \ell_m^a, 0, \dots, 0) \in \mathbb{R}^z, \quad l_v = (0, \dots, 0, \ell_1^v, \dots, \ell_n^v) \in \mathbb{R}^z$$

are vectors containing the length of the terminal segments. Then we can write  $f = f[S]$  and

$$p(x) = -\Delta^{-1} f[S](x) = p[S](x).$$

### Dissipation of Kinetic Energy by Friction

In our case, the rate of *dissipation of kinetic energy by friction* for a fluid flowing through a porous medium is given by (see [24])

$$E(p) = \int_{\Omega} \nabla p \cdot \nabla p$$

and we want to minimize this quantity depending on the outflows and inflows  $S$  subject to the constraints

$$\begin{aligned} l_a \cdot S &= c \\ l_v \cdot S &= c \\ S &\in \mathbb{R}_+^z. \end{aligned}$$

The first two constraints representing the total flow condition is denoted  $S \in \Lambda_c$  for short, the third condition is nonnegativity of the flow:  $\mathbb{R}_+^z = [0, \infty)^z$ .

So write  $E$  in terms of  $S$ :

$$\begin{aligned} E(S) &= \int_{\Omega} \nabla p[S](x) \cdot \nabla p[S](x) \, dx \\ &= \int_{\Omega} p[S](x) \cdot (-\Delta p[S](x)) \, dx \\ &= \int_{\Omega} p[S](x) \cdot f[S](x) \, dx \longrightarrow \min! \end{aligned} \tag{2.7}$$

where  $p$  is the solution to problem (2.6).

So we have the problem of minimizing the function  $E : \mathbb{R}^z \rightarrow \mathbb{R}, S \mapsto E(S)$  over  $\Lambda_c \cap \mathbb{R}_+^z$ .

$\Lambda_c$  is an affine subspace of codimension 2, for strictly positive lengths  $\ell_1^a, \dots, \ell_m^a, \ell_1^v, \dots, \ell_n^v$  its intersection with  $\mathbb{R}_+^z$  is a bounded convex polyhedron of dimension  $(z - 2)$  in  $\mathbb{R}^z$ .

**Proposition 2.5.1.**  *$E$  as in (2.7) attains its minimum in  $\Lambda_c \cap \mathbb{R}_+^z$ .*

*Proof.*  $p = -\Delta^{-1}f \in H^1$  depends continuously on  $f \in H^{-1}(\Omega)$ , so in total  $E(S)$  is a composition of continuous functions, thus depends continuously on  $S$ , the feasible set for  $S$  is closed and bounded (and finite dimensional, thus compact), so the minimum of  $E$  is attained somewhere in  $\Lambda_c \cap \mathbb{R}_+^z$ .  $\square$

#### 2.5.2 Discretization

We use the same finite element discretization as in Section 3.3 and use  $F$  for the grid approximation to  $f$  on a grid with  $N$  grid points.

We can write

$$F = A \cdot S$$

for an appropriate matrix  $A \in \mathbb{R}^{N \times t}$  mapping the inflow vector to the  $L^2$  scalar product of constant inflow on segment and appropriate base function:

$$\begin{aligned} A_{k,j} &= S_j \int_{\text{segment } j} \varphi_k \\ &= \sum_{\text{grid cell } g} S_j \int_{g \cap j \cap \text{supp}(\varphi_k)} \varphi_k. \end{aligned}$$

These entries are computed in a similar way as in Section 3.3. The function (flow) values are constant on each segment. The basis functions  $\varphi$  are piecewise bilinear, so the integrand is a second order polynomial (piecewise bilinear function on straight line segment), so three-point Lobatto quadrature used for assembling  $A$  is exact.

The discrete energy function can be written as

$$E(S) = \bar{P}(S) \cdot L\bar{P}(S) = \bar{P}(S) \cdot F(S)$$

so minimizing  $E$  is equivalent to minimizing

$$\begin{aligned} h(S) &= \bar{P}(S) \cdot F(S) \\ &= L^{-1}\bar{P}(S) \cdot F(S) \\ &= L^{-1}AS \cdot AS \\ &= A^T L^{-1}AS \cdot S \\ &=: HS \cdot S. \end{aligned}$$

Here,  $L^{-1}$  is the discrete solution operator for the discretization of problem (2.6), the extended system as in (3.12).

So our discrete problem is to minimize the quadratic function  $h(S)$  over a convex polyhedron  $\Lambda_c \cap \mathbb{R}_+^z$ .  $h$  is continuous, so analytically this problem has a solution.

We use a feasible direction method for the numerical optimization because we want to avoid inequality constraints in a Lagrangian approach and because projection onto  $\Lambda_c \cap \mathbb{R}_+^z$  is not easy which excludes projection methods.

### 2.5.3 Conditional Gradient Method for the Quadratic Optimization Problem

In a *feasible direction method*, we start with some *initial guess*  $S^0$  of the minimum and then compute a sequence  $(S^k)_k$  where  $S^{k+1} = S^k + \alpha^k d^k$ .  $d^k$  is a feasible descent direction and  $\alpha^k$  is some positive stepsize.

**Definition 2.5.2.** Let  $S^k \in \Lambda_c \cap \mathbb{R}_+^z$ .

$d^k$  is a *feasible direction* :  $\iff \exists \epsilon_0 : S^k + \epsilon d^k \in \Lambda_c \cap \mathbb{R}_+^z \ \forall \epsilon < \epsilon_0$ .

$d^k$  is a *descent direction* :  $\iff \exists \epsilon_0 : h(S^k + \epsilon d^k) < h(S^k) \ \forall \epsilon < \epsilon_0$ .

#### $S^0$ : Initial Guess

At this stage, we have no information about what might be a good starting point, so we take the uniform distribution having the same total flow out of each terminal arterial segment and the same total flow into each terminal venous segment:

$$S^0 = \left( \frac{c}{m \cdot \ell_{a,1}}, \dots, \frac{c}{m \cdot \ell_{a,m}}, \frac{c}{n \cdot \ell_{v,1}}, \dots, \frac{c}{n \cdot \ell_{v,n}} \right).$$

#### $d^k$ : Feasible Descent Direction

For generating descent directions, we use the *conditional gradient method*, also known as *Frank-Wolfe method*: See [4], Section 2.2.

Let  $d^k = \tilde{S}^k - S^k$  where

$$\begin{aligned} \tilde{S}^k &= \operatorname{argmin}_{S \in \Lambda_c \cap \mathbb{R}_+^z} \nabla h(S^k) \cdot (S - S^k) \\ &= \operatorname{argmin}_{S \in \Lambda_c \cap \mathbb{R}_+^z} \nabla h(S^k) \cdot S \end{aligned} \quad (2.8)$$

because  $\nabla h(S^k) \cdot S^k$  is constant.

For  $h$  defined above,  $\nabla h(S) = 2A^T L^{-1} AS$ .

This subproblem is a linear optimization problem over a (convex) polyhedron. A linear function always attains its minimum over a bounded polyhedron at a vertex of the polyhedron. The minimum need not be unique, but for the conditional gradient method, any minimum works.

The vertices of  $\Lambda_c \cap \mathbb{R}_+^z$  are

$$\left\{ \left( \frac{c}{\ell_{a,i}} e_i + \frac{c}{\ell_{v,j}} e_j \right) \mid i \in \{1, \dots, m\}, j \in \{m+1, \dots, m+n\} \right\}$$

where  $e_i$  is the canonical basis vector of  $\mathbb{R}^z$ , so we need to find the minimum over  $mn$  vertices.

Due to the form of the vertices, the function evaluation for (2.8) only takes two multiplications, finally one vector subtraction needs to be computed, so in total finding a descent direction takes  $O(mn)$  flops. Typically,  $m$  and  $n$  are approximately  $\frac{z}{2}$ , so it takes  $O(z^2)$  flops to find each descent direction.

Note that due to  $\tilde{S}^k \in \Lambda_c$  and  $S^k \in \Lambda_c$ ,  $d^k$  is a feasible direction.

### $\alpha^k$ : Stepsize

The stepsize is chosen according to the *Armijo step size rule* [4]: for given parameters  $s > 0, \beta \in (0, 1), \sigma \in (0, 1)$  let  $\alpha^k = s \cdot \beta^m$  where  $m$  is the smallest nonnegative integer satisfying  $S^k + s\beta^m d^k \in \Lambda_c \cap \mathbb{R}_+^z$  for which

$$\frac{h(S^k + s\beta^m d^k) - h(S^k)}{s\beta^m} \leq \sigma \nabla h(S^k) \cdot d^k$$

$$\iff |\text{secant slope}| \geq \sigma |\text{tangent slope}|.$$

Function evaluation is the expensive part of the computation. For each  $m$ , we need to evaluate  $h$  once, this requires

- mapping from  $\mathbb{R}^z$  to  $\mathbb{R}^N$ :  $S \mapsto AS$
- solving a linear system in  $\mathbb{R}^N$ :  $AS \mapsto \bar{P} = L^{-1} AS$  (in fact, the system has one additional equation and unknown due to  $\int_{\Omega} p = 0$ , see Section 3.3).
- computing the dot product of a vector in  $\mathbb{R}^N$  with itself:  $\bar{P} \mapsto \bar{P} \cdot \bar{P}$ .

Since the grid discretizing the domain should resolve the segments sufficiently well,  $N = (2^j + 1)^2$  is typically large compared to  $t$ . “Fine” trees we use have  $z = 1024$ , for a “moderately fine” grid,  $z = 8$  implies  $z = 66,049$ .

Mapping between the different dimensions is only a matrix-vector multiplication, setting up and solving the linear system in between is the most expensive part of this, not only in terms of cputime, but also in terms of memory. Our implementation, see Section 2.5.4, needs 20 MB of memory for  $g = 8$ , 80 MB for  $g = 9$  and so on, increasing  $g$  by 1 increases the size of the system, thus the memory requirement, by a factor of four.

### Stopping Criterion

We stop the optimization as soon as the relative decrease in one step  $\frac{h(S^k)}{h(S^{k-1})}$  is bigger than some threshold, e. g. 0.999, i. e. the improvement is less than 0.1 %.

### Convergence

**Proposition 2.5.3.** *For the sequence  $(S^k)$  generated by the conditional gradient method with Armijo stepsize, every limit point is a stationary point of the objective function  $h$ .*

*Proof.* For a proof and a detailed discussion of feasible direction methods, we refer to [4], Section 2.2. □

Unfortunately, not only each step is expensive, but also convergence is slow. There is no guarantee of even linear convergence [4].

### Improvement by a Cascadic Approach

When trying to find a good starting point for solving this problem for a fine discretization of  $\Omega$ , it seems plausible that a solution for a coarser discretization is a better starting point than the uniform distribution described above. This is also what the idea of *multigrid methods* ([6, 33]) is based on.

Note that we are optimizing a function defined on the terminal segments of the trees and not on the grid, so restriction and prolongation of the solution are not necessary.

Here, we can use this idea as follows:

1. Start with a coarse grid (e. g. grid level  $g = 2$ ), solve the optimization problem for this grid
2. Refine the grid by a factor of 2 (increase  $g$  by 1), take the solution from the step before as an initial guess to solve the optimization problem on the current grid
3. Repeat step 2 until a sufficiently fine grid is reached (e. g.  $g = 8$ ).

Typically, the finest grid level here is the grid level on which further computations will be carried out.

To make sure that this cascadic approach does not worsen things, in each step we can check whether the solution on a coarser grid is a better starting value than the uniform initial guess.

## 2.5.4 Implementation and Results

### Implementation

We solve the steady-state problem as in the heat-conduction case using the quocmesh library.

For and  $A^T L^{-1} A$ , we implemented the composition of operators where domain and range have different dimension. This requires storing temporary vectors of appropriate size.  $L^{-1}$  is implemented in the same way as in Section 3.3.

The feasible direction method and Armijo step size search were implemented to perform the computations described above.

level	# steps	16-tree		64-tree	
		cputime (s)	# steps	cputime (s)	
2	95	0.15	530	4.59	
3	102	0.31	349	3.89	
4	30	0.45	150	3.39	
5	14	1.58	81	9.08	
6	13	27.21	21	46.20	
7	4	88.34	16	322.27	
8	3	359.24	15	1457.80	

Table 2.2: Number of optimization steps and computation times for the flow splitting optimization on the trees with 16 and 64 terminal segments

## Results

We present the results of applying this method to a tree with 8 terminal segments where we ran the optimization from grid level 2 to 8. The parameters for the Armijo rule were  $s = 0.2, \beta = 0.4, \sigma = 0.5$ , no more than 50 steps were carried out ( $k \leq 50$ ), if no descent was found within 50 steps of the Armijo rule, we set  $S^{k+1} = S^k$ . This is reasonable because  $0.4^{50} \approx 1.2 \cdot 10^{-20}$ . Our relative stopping criterion was 0.9995.

In Figure 2.7, we show the results for an optimization on a tree with 16 terminal segments on grid levels 2 to 8, where the flow velocities are color-coded on a logarithmic color scale shown in Figure 2.10 where red corresponds to velocity 1 and blue to  $1/1024$ . All lower velocities are also shown in this blue.

The pressure is also shown, the same scaling was used for all four pressure plots for the same tree where the same colors scale is now used as a linear color scale: red corresponds to maximal pressure, green to zero pressure and blue to minimal pressure.

We used the same parameters and grid levels 4 to 8 for a tree with 64 terminal segments, the result is shown in Figure 2.8.

The computation was carried out on a desktop PC with a 1 GHz Athlon CPU, computation times and the number of successive optimization steps on each grid level are shown in Table 2.2.

We can see that the flow velocities decrease as we go down the tree (this follows from flow conservation and equation (2.2)) and that velocities on the terminal segments, thus the outflow, behave as expected: terminal segments close to terminal segments of the other tree have significantly more out/inflow than those further apart.

Moreover, at least for these trees, grid level 6 resolves the pressure problem very well so that the (expensive) computation on finer grid levels is not necessary. However, it may be necessary to use even finer grids if we deal with more complex trees.

## Limitations

We can also see two limitations of our model: Short segments only have a small influence on the pressure distribution, so the optimization of the corresponding variables only happens at a very late state of the overall optimization.

Segments pointing from one tree towards the other tree (those can be seen in the center of both trees) are assigned a lower velocity than one might expect. This is due to the fact that

we assumed constant outflow and inflow on each terminal segment. It would be necessary to refine the model to obtain more realistic flow velocities. In the three-dimensional application however, flow velocities will be given, moreover the results are acceptable for our purposes, so we did not refine this model any further.

### Improvement by a Cascadic Method

Finally, we were interested in whether our cascadic approach really is an improvement of the method. As a measure for this, we plotted the logarithm of the function value  $h(S^k)$  versus the time it took to attain this value. From a theoretical point of view, the number of function evaluations might be more interesting, but the function is evaluated with respect to different grids, and as we did not investigate the theoretical properties of the cascadic method, from a practical point of view the cputime is more interesting to us.

To check whether our cascadic approach above really helps, we compared running our method on the tree with 16 terminal segments and the same Armijo parameters as above and a stopping threshold of 0.999 on level 5 only compared to solving it on level 4 and using the solution as a starting point for the optimization on level 5. We repeated this for levels 5 and 6.

The same comparison was run for the tree with 64 terminal segments, the same threshold and the same grid levels.

In Figure 2.9, we plotted cputime vs logarithm of value of  $h$  attained at that time. The green curve is for a computation on one level only whereas the red curve shows the behavior for a computation on two levels. (1) and (3) compare level 5 only to levels 4 and 5, (2) and (4) compare level 6 only to levels 5 and 6.

The jumps in case of our cascadic method are due to the fact that evaluating  $h$  requires solving a pressure problem on a grid of the corresponding grid level, so different grids lead to different solutions.

We can see that the cascadic approach speeds the computation up to some extent. Solving on levels 4 and 5 instead of 5 only for the 64-tree did not help, this might be due to the fact that a grid of level 4 cannot resolve this tree appropriately.

The non-smoothness of the curves show that different steps of the minimization take different amounts of cputime and lead to different decreases in the function value.

Further experiments and analysis will be necessary to determine if and in which case it makes sense to use this approach in general. We will also need to investigate whether using finer grid discretizations leads to a convergence of  $L^{-1}AS$  to a continuous pressure distribution and of  $h(S)$  to the continuous energy function.

Finally, Figure 2.11 shows the flow velocities determined for the trees shown in Figure 2.5 in the same color code as above. The trees with these velocities will be used later on.

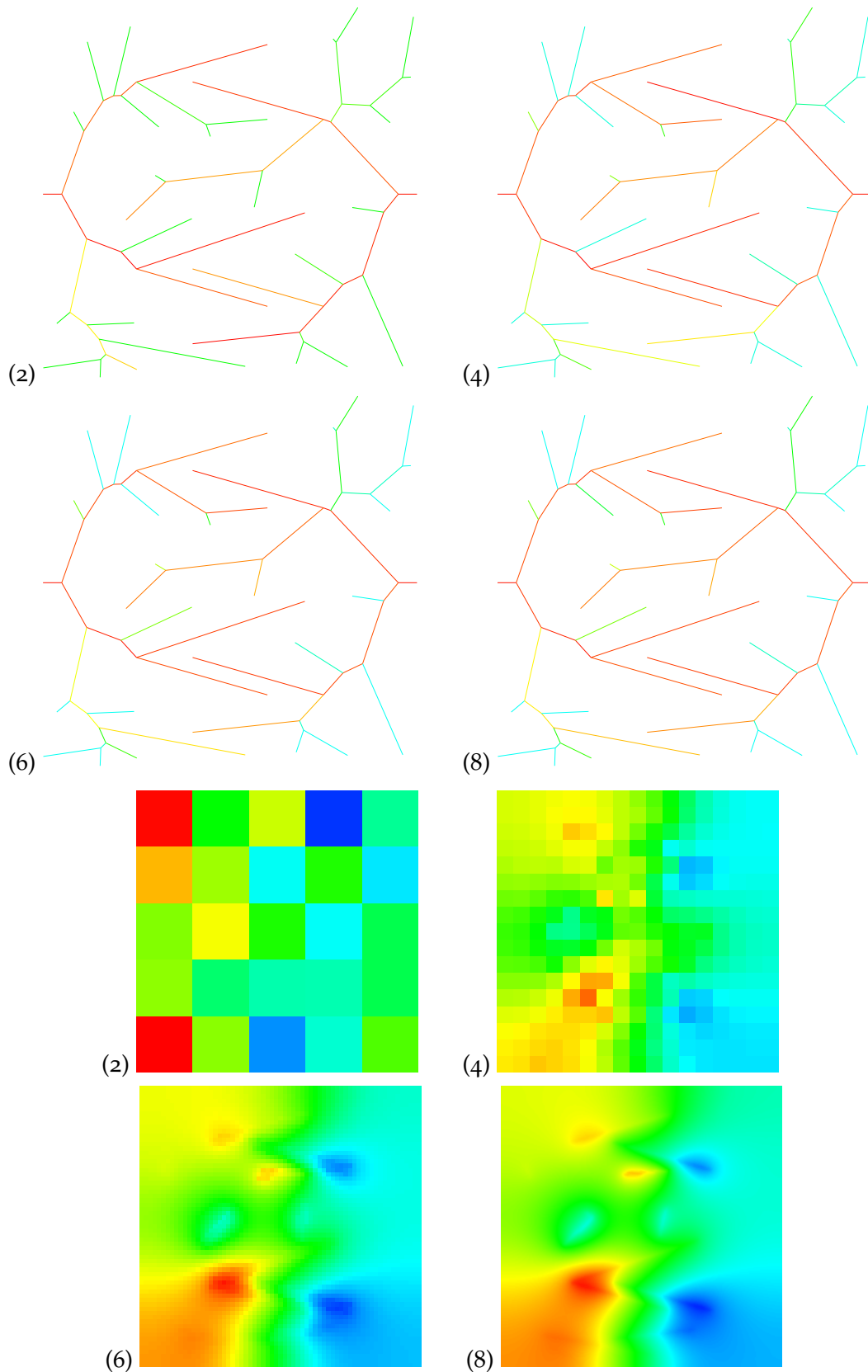


Figure 2.7: Determining flow velocities via a pressure model, successive optimization on grid levels 2, 4, 6 and 8: Flow velocities and pressure distributions for a tree with 16 terminal segments

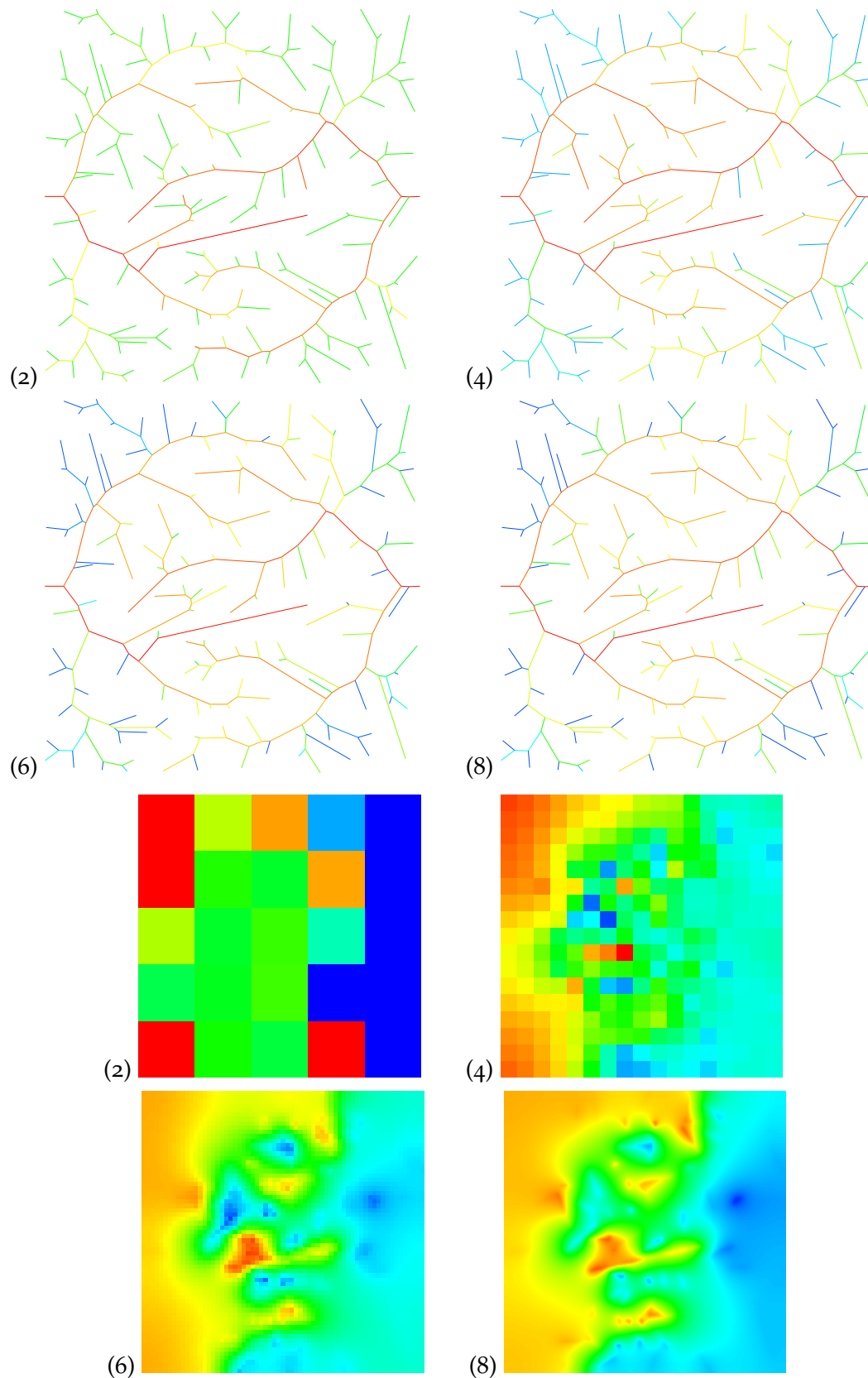


Figure 2.8: Determining flow velocities via a pressure model, successive optimization on grid levels 2, 4, 6 and 8: Flow velocities and pressure distributions for a tree with 64 terminal segments

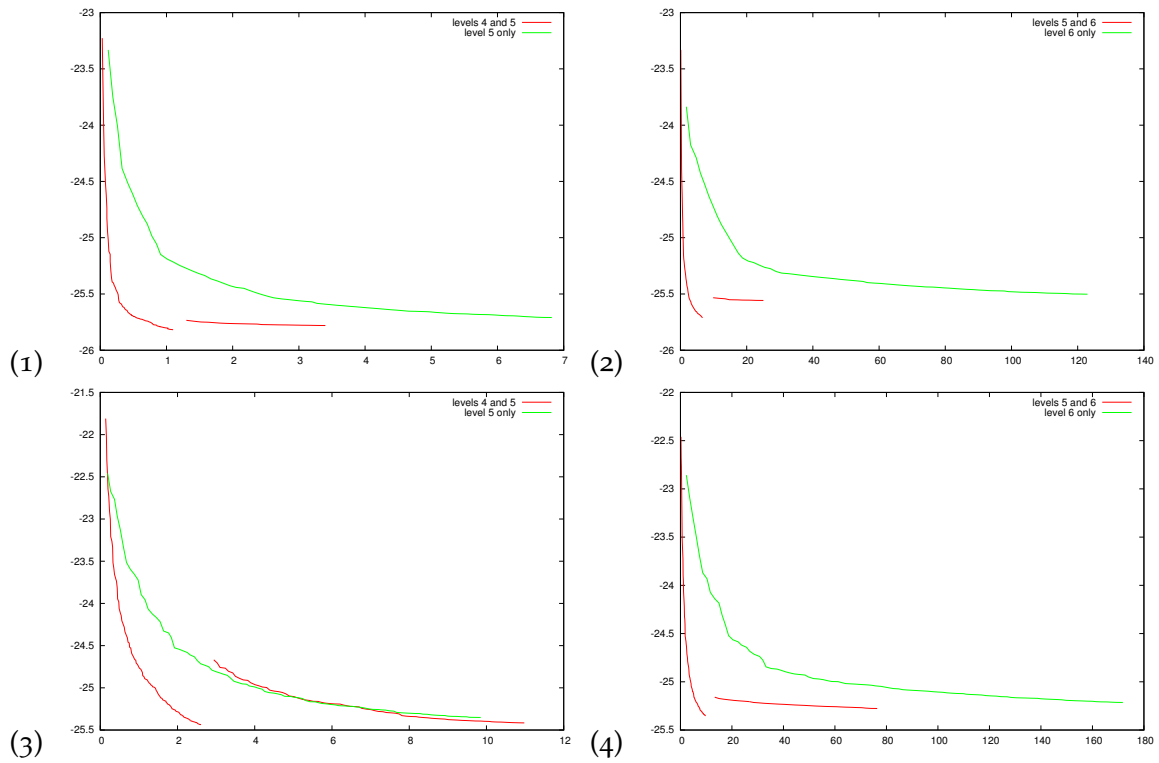


Figure 2.9: Comparison of computation time versus log value of  $h$  attained, one level only vs. computing initial guess on coarser grid, for the 16-tree (1,2) and 64-tree (3,4)



Figure 2.10: The color scale used in our plots: Red (left) corresponds to maximal values, blue (right) to minimal values with a hsv transition in between.

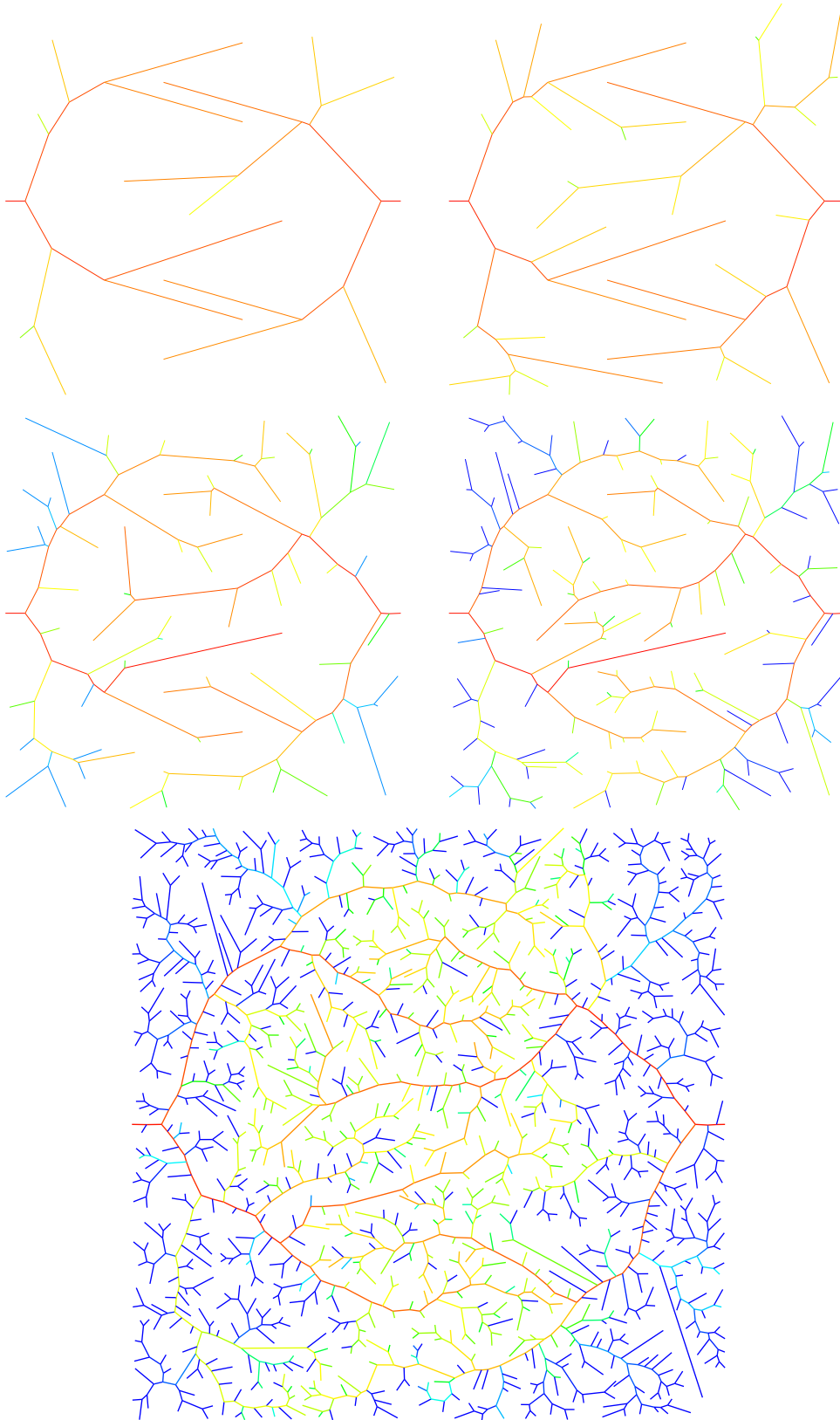


Figure 2.11: Flow velocities (color coded) determined for the trees shown in Figure 2.5.

## 3 Heat Conduction in Tissue

As a first computational problem we consider *isotropic heat conduction* in the domain of tissue  $\Omega = [0, 1] \times [0, 1] \in \mathbb{R}^2$  during the time interval  $[0, T]$  with constant heating / cooling by the two vessel trees and perfectly insulated boundary of the domain. For simplicity, the heat conduction coefficient is assumed to be 1. Also, we ignore external heating by the RF probe at first.

We view the trees as line sources, the source term on the arterial tree  $T_a$  is called  $f_a$ , similarly the source term on the venous tree  $T_v$  is  $f_v$ . In the continuous model, this is only possible if the source terms are understood in a distributional sense.  $f_a$  is constant and positive on each segment of the arterial tree and proportional to the cross section area  $A_{\mathcal{O},s}$ ,  $f_v$  negative, constant on each segment of the venous tree and proportional to the cross section area (corresponding to heating / cooling with fixed constant temperatures on the two trees). In particular,  $f_a$  and  $f_v$  are constant in time.

### 3.1 Continuous and Weak Problem

#### 3.1.1 Continuous Formulation

Heat conduction with a source term and Neumann boundary conditions in general is modeled by the following initial-boundary value problem, see [27, Chapter 11] for  $u : [0, T] \times \Omega \rightarrow \mathbb{R}$ ,  $u(t, \cdot) \in C^{0,1}(\Omega)$ ,  $u(\cdot, x) \in C^0((0, T))$ :

$$\begin{aligned} \partial_t u(t, x) - \Delta_x u(t, x) &\stackrel{*}{=} f(t, x) && \text{in } (0, T) \times \Omega \\ \partial_\nu u(t, x) &= 0 && \text{on } (0, T) \times \partial\Omega \\ u(0, x) &= u_0(x) && \text{on } \Omega. \end{aligned} \quad (3.1)$$

where  $\Delta_x = (\frac{\partial^2}{\partial x_1^2} + \frac{\partial^2}{\partial x_2^2})$  denotes the Laplacian in space and  $\partial_\nu$  is the derivative with respect to the outer normal of the domain. Here, our initial condition is  $u_0(x) = 0$  such that  $u_0 \in L^2(\Omega)$  and  $\int_\Omega u_0 = 0$ .

The starred equation is to be understood in a distributional sense with  $f(t, \cdot) \in H^{-1}(\Omega)$ , as in equation (3.4) below.

#### 3.1.2 Weak Formulation

First define the following function spaces:

$$\begin{aligned} V &:= \left\{ v \in H^1(\Omega) \mid \int_\Omega v = \int_\Omega u_0 = 0 \right\} \subset H^1(\Omega) \\ L^2((0, T); V) &:= \left\{ u : (0, T) \rightarrow V \mid u \text{ is measurable} \wedge \|u(t, \cdot)\|_{H^1(\Omega)} \in L^2((0, T)) \right\} \\ C^0([0, T]; L^2(\Omega)) &:= \left\{ u : [0, T] \rightarrow V \mid u \text{ is measurable} \wedge u(\cdot, x) \in C^0([0, T]) \forall x \in \Omega \right\}. \end{aligned} \quad (3.2)$$

$v \in V \subset H^1(\Omega)$  has a trace on  $T_a \cup T_v \subset \Omega$ ,  $\tilde{v} \in L^2(T_a \cup T_v)$ . We omit the tilde and use  $v$  for both functions.

$\Omega \setminus (T_a \cup T_v)$  does not have Lipschitz boundary, but still a trace theorem holds, the proof is similar to the proof of the trace theorem in [2, Section A5].

Hence  $f : v \mapsto \int_{T_a \cup T_v} f \cdot v$  is a linear map from  $V$  to  $\mathbb{R}$  so  $f$  can be viewed as an element  $f \in DV$ , the dual space of  $V$ .  $V$  is a subspace of  $H^1\Omega$ , so  $H^{-1}(\Omega)$  is a subspace of  $DV$ , see Section 6.2.2.

So for  $f(t, \cdot) \in H^{-1}(\Omega)$  and  $f(\cdot, x)$  constant (in time), we have  $f \in L^2((0, T); DV)$ .

The weak form of our heat conduction problem is:

Given  $f \in L^2((0, T); DV)$  as above, find  $u : [0, T] \times \Omega \rightarrow \mathbb{R}$ ,  $u \in L^2((0, T); V) \cap C^0([0, T]; L^2(\Omega))$  so that  $\forall v \in V, t \in [0, T]$ :

$$\begin{aligned} \int_{\Omega} \partial_t u(t, x) \cdot v(x) \, dx + \int_{\Omega} \nabla u(t, x) \nabla v(x) \, dx &= \int_{T_a} f_a(t, x) \cdot v(x) \, d\gamma + \int_{T_v} f_v(t, x) \cdot v(x) \, d\gamma \\ u(0, x) &= u_0(x) = 0 \end{aligned} \quad \forall x \in \Omega. \quad (3.3)$$

For sufficiently smooth  $u$ , we can combine the integrations over the trees

$$\begin{aligned} \int_{\Omega} \partial_t u(t, x) \cdot v(x) + \nabla_x u(t, x) \cdot \nabla_x v(x) \, dx &= \int_{T_a} f_a(t, x) \cdot v(x) + \int_{T_v} f_v(t, x) \cdot v(x) \\ &= \int_{T_a \cup T_v} f(t, x) \cdot v(x) \, d\gamma \end{aligned}$$

$\forall v \in V, t \in [0, T]$ , apply partial integration in space and obtain:

$$\begin{aligned} \int_{\Omega} (\partial_t u(t, x) - \Delta_x u(t, x)) \cdot v(x) \, dx + \int_{T_a \cup T_v} [\nabla u(t, x) \cdot n(x)] \cdot v(x) \, d\gamma &= \int_{T_a \cup T_v} f(t, x) \cdot v(x) \, d\gamma \\ \int_{\Omega} (\partial_t u(t, x) - \Delta_x u(t, x)) \cdot v(x) \, dx &= \int_{T_a \cup T_v} f(t, x) \cdot v(x) - [\nabla u(t, x) \cdot n(x)] \cdot v(x) \, d\gamma \end{aligned} \quad (3.4)$$

$\forall v \in V, t \in [0, T]$ , where  $[\dots]$  in the integration denotes the jump in the spatial normal derivative of  $u(t, x)$  across the vessel segments.  $n(x)$  is the normal on the vessel segment oriented the same way as the jump, so this expression is well-defined.

This is the distributional interpretation in problem (3.1).

### 3.1.3 Existence of Weak Solutions

To prove the existence of weak solutions, we need the following lemmas:

**Lemma 3.1.1.** *The bilinear form  $a : V \times V \rightarrow \mathbb{R}$ ,  $(u, v) \mapsto \int_{\Omega} \nabla u(x) \cdot \nabla v(x) \, dx$  is continuous.*

*Proof.*

$$\begin{aligned} |a(u, v)|^2 &= \left| \int_{\Omega} \nabla u \cdot \nabla v \right|^2 \\ &\leq \|\partial_x u \partial_x v + \partial_y u \partial_y v\|_{L^1(\Omega)}^2 \\ &\leq 2 \left( \|\partial_x u \partial_x v\|_{L^1(\Omega)}^2 + \|\partial_y u \partial_y v\|_{L^1(\Omega)}^2 \right) \end{aligned}$$

by Hölder's inequality, see Lemma 6.2.8,

$$\begin{aligned}
&\leq 2 \left( \|\partial_x u\|_{L^2(\Omega)}^2 \|\partial_x v\|_{L^2(\Omega)}^2 + \|\partial_y u\|_{L^2(\Omega)}^2 \|\partial_y v\|_{L^2(\Omega)}^2 \right) \\
&\leq 2 \cdot \left( \|u\|_{L^2(\Omega)}^2 + \|\partial_x u\|_{L^2(\Omega)}^2 + \|\partial_y u\|_{L^2(\Omega)}^2 \right) \cdot \left( \|v\|_{L^2(\Omega)}^2 + \|\partial_x v\|_{L^2(\Omega)}^2 + \|\partial_y v\|_{L^2(\Omega)}^2 \right) \\
&= \|u\|_{H^1(\Omega)}^2 \|v\|_{H^1(\Omega)}^2.
\end{aligned}$$

□

**Lemma 3.1.2.** *a is coercive.*

*Proof.* For our  $\Omega$ , we have Lemma 6.2.7:

$$\|v\|_{H^0(\Omega)} \leq C \left( \bar{v} + |v|_{H^1(\Omega)} \right) \quad \forall v \in H^1(\Omega)$$

where  $\bar{v} = \frac{1}{\text{vol}\Omega} \int_{\Omega} v$ . For  $v \in V$ ,  $\bar{v} = 0$ , so

$$\begin{aligned}
&\|v\|_{H^0} \leq C|v|_{H^1} \\
&\Rightarrow \|v\|_{H^0}^2 \leq C^2|v|_{H^1}^2 \\
&\Rightarrow |v|_{H^1}^2 + \|v\|_{H^0}^2 \leq (1 + C^2)|v|_{H^1}^2 \\
&\Rightarrow \|v\|_{H^1}^2 \leq (1 + C^2)|v|_{H^1}^2 \\
&\Rightarrow |v|_{H^1}^2 \geq \frac{1}{1 + C^2} \|v\|_{H^1}^2 \\
&\Rightarrow \int_{\Omega} \nabla v \cdot \nabla v \geq \frac{1}{1 + C^2} \|v\|_V^2.
\end{aligned}$$

□

Now we can apply an existence theorem for weak solutions [27, theorem 11.1.1 and remark 11.1.1] for this type of problem:

**Proposition 3.1.3** (Existence of a Weak Solution). *Problem (3.3) has a unique solution.*

*Proof.* By the preceding Lemmas 3.1.2 and 3.1.1, we know that  $a$  is a coercive and continuous bilinear form on  $V$ .

We assumed  $f \in L^2((0, T); DV)$  and  $u_0 \in L^2(\Omega)$ , so the existence theorem can be applied.

For the proof and a more detailed discussion, we refer to [27, Section 11.1]. □

## 3.2 Discretization

We first discretize the weak problem in space using finite elements to obtain a system of coupled ODEs, then we apply a time stepping method to also achieve temporal discretization.

### 3.2.1 Discretization in Space

Let  $V_h = \text{span}(\varphi_j)$  be the space of piecewise bilinear finite elements for a uniform quadratic grid with grid size  $h$  and  $(\varphi_j)$  be the standard basis of  $V_h$ , see Section 6.3.

The discrete problem is to find  $U \in V_h$  such that

$$\begin{aligned} \partial_t \int_{\Omega} U(t, x) V(x) dx + \int_{\Omega} \nabla_x U(t, x) \cdot \nabla_x V(x) dx &= \int_{T_a} f_a V + \int_{T_v} f_v V \quad \forall V \in V_h \\ U(0, \cdot) &= U_0(\cdot) \end{aligned} \quad (3.5)$$

where  $U_0(x)$  is the discretization of the initial data  $u_0(x)$ .

It is sufficient if this holds for all basis functions  $\varphi_j$ :

$$\begin{aligned} \partial_t \sum_i U_i \underbrace{\int_{\Omega} \varphi_i \varphi_j}_{=: M_{i,j}} + \sum_i U_i \underbrace{\int_{\Omega} \nabla \varphi_i \cdot \nabla \varphi_j}_{=: L_{i,j}} &= \underbrace{\int_{T_a} f_a \varphi_j}_{=: F_j} + \int_{T_v} f_v \varphi_j \quad \forall j \\ \partial_t M \bar{U} + L \bar{U} &= F \end{aligned} \quad (3.6)$$

where  $M := (M_{i,j})_{i,j}$  and  $L := (L_{i,j})_{i,j}$  are the 2D FE mass and stiffness matrices, respectively, see Section 6.3. This is a system of coupled ODEs. Since  $M$  is symmetric and positive definite, there is a unique solution  $U$  to the corresponding initial value problem ([15], Section 49):

$$\begin{aligned} \partial_t z(t) + M^{-1} L z(t) &= M^{-1} F(t) \quad t \in (0, T) \\ z(0) &= z_0. \end{aligned} \quad (3.7)$$

### 3.2.2 Discretization in Time

For temporal discretization, we apply the *Backward Euler time stepping* method [19, Section 6.2] to (3.6). Let  $\tau$  be the temporal grid width,  $t^k = k\tau$  and  $t^R = T$ . Then Backward Euler is

$$M \cdot \frac{\bar{U}^{k+1} - \bar{U}^k}{\tau} + L \cdot \bar{U}^{k+1} = F.$$

Note that  $F$  is constant in time because the source terms  $f_a, f_v$  are.

Now rearrange terms in order to get an expression for  $\bar{U}^{k+1}$ :

$$\begin{aligned} M \cdot \bar{U}^{k+1} - M \cdot \bar{U}^k + \tau L \cdot \bar{U}^{k+1} &= \tau F \\ \Leftrightarrow (M + \tau L) \cdot \bar{U}^{k+1} &= M \cdot \bar{U}^k + \tau F \\ \Leftrightarrow \bar{U}^{k+1} &= (M + \tau L)^{-1} \cdot (M \cdot \bar{U}^k + \tau F). \end{aligned} \quad (3.8)$$

### 3.2.3 RHS Source Integrals

For the entries of the vector  $F$ , i. e. the source integrals in (3.6), we need to evaluate

$$F_k = \int_{T_a} f_a(\xi) \cdot \varphi_k(\psi^{-1}(\xi)) d\xi + \int_{T_v} f_v(\xi) \cdot \varphi_k(\psi^{-1}(\xi)) d\xi$$

for all basis functions  $\varphi_k$ . Those integrals are computed as (in case of the arterial tree, similarly for the venous tree)

$$\sum_g \sum_{\text{grid cell}} \sum_{s \in T_a} \int_{g \cap s} f_a(\xi) \cdot \varphi_k(\psi^{-1}(\xi)) d\xi.$$

In case of piecewise bilinear base functions that have the value one on exactly one grid point and zero on all other grid points, we only need to consider four base functions whose support contains the straight line segment  $g \cap s$ .

Our basis functions  $\varphi$  are piecewise bilinear functions in 2D, so along a straight line segment within one grid cell they can be considered as polynomials of order 2. We had to compute the points where the segment intersects the boundary of the grid cell earlier<sup>1</sup>, the central point half way between those two is easily computed as well. So if we use three-point quadrature according to Proposition 6.1.1, this is exact for  $f_a$  being a first order polynomial. Here,  $f_a$  is constant for each integration, so the quadrature is exact. Later on in the coupled problem,  $f_a$  is piecewise linear, then we will have to subdivide the line of integration to obtain exact quadrature.

$F$  is not assembled entry-(grid point)-wise but we loop over all grid cells, then over all segments intersecting that grid cell, and add up partial results in the appropriate entries of  $F$ .

Fix one grid cell  $g$  indexed by  $(i, j)$  and one segment intersecting that cell at the points  $(x_i^\ell, y_i^\ell), (x_t^\ell, y_t^\ell)$  (here,  $\ell$  does not refer to length of the segment but denotes local coordinates with respect to the grid cell). There are four base functions for which

$$\int_{g \cap s} f_a \cdot \varphi d\gamma$$

does not vanish, index those with the grid point where they have value one<sup>2</sup>:  $\varphi_{i,j}, \varphi_{i+1,j}, \varphi_{i,j+1}, \varphi_{i+1,j+1}$

For  $x_c^\ell := \frac{1}{2}(x_i^\ell + x_t^\ell), y_c^\ell := \frac{1}{2}(y_i^\ell + y_t^\ell)$ , the three-point Lobatto quadrature (see Proposition 6.1.1) looks as follows:

$$\begin{aligned} \int_{g \cap s} f_a \varphi_{i,j} &= \frac{A_\emptyset h}{6} \cdot \left( \begin{array}{l} f_a(x_i^\ell, y_i^\ell) \cdot \varphi_{i,j}(x_i^\ell, y_i^\ell) + f_a(x_t^\ell, y_t^\ell) \cdot \varphi_{i,j}(x_t^\ell, y_t^\ell) \\ + 4 \cdot f_a(x_c^\ell, y_c^\ell) \cdot \varphi_{i,j}(x_c^\ell, y_c^\ell) \end{array} \right) \\ &= \frac{A_\emptyset h}{6} \cdot \left( \begin{array}{l} f_a(x_i^\ell, y_i^\ell) \cdot (x_i^\ell \cdot y_i^\ell) + f_a(x_t^\ell, y_t^\ell) \cdot (x_t^\ell \cdot y_t^\ell) \\ + 4 \cdot f_a(x_c^\ell, y_c^\ell) \cdot \left(\frac{1}{2}(x_i^\ell + x_t^\ell) \cdot \frac{1}{2}(y_i^\ell + y_t^\ell)\right) \end{array} \right) \\ \int_{g \cap s} f_a \varphi_{i+1,j} &= \frac{A_\emptyset h}{6} \cdot \left( \begin{array}{l} f_a(x_i^\ell, y_i^\ell) \cdot ((1 - x_i^\ell) \cdot y_i^\ell) + f_a(x_t^\ell, y_t^\ell) \cdot ((1 - x_t^\ell) \cdot y_t^\ell) \\ + 4 \cdot f_a(x_c^\ell, y_c^\ell) \cdot \left(\frac{1}{2}((1 - x_i^\ell) + (1 - x_t^\ell)) \cdot \frac{1}{2}(y_i^\ell + y_t^\ell)\right) \end{array} \right) \\ \int_{g \cap s} f_a \varphi_{i,j+1} &= \frac{A_\emptyset h}{6} \cdot \left( \begin{array}{l} f_a(x_i^\ell, y_i^\ell) \cdot (x_i^\ell \cdot (1 - y_i^\ell)) + f_a(x_t^\ell, y_t^\ell) \cdot (x_t^\ell \cdot (1 - y_t^\ell)) \\ + 4 \cdot f_a(x_c^\ell, y_c^\ell) \cdot \left(\frac{1}{2}(x_i^\ell + x_t^\ell) \cdot \frac{1}{2}((1 - y_i^\ell) + (1 - y_t^\ell))\right) \end{array} \right) \\ \int_{g \cap s} f_a \varphi_{i+1,j+1} &= \frac{A_\emptyset h}{6} \cdot \left( \begin{array}{l} f_a(x_i^\ell, y_i^\ell) \cdot ((1 - x_i^\ell) \cdot (1 - y_i^\ell)) + f_a(x_t^\ell, y_t^\ell) \cdot ((1 - x_t^\ell) \cdot (1 - y_t^\ell)) \\ + 4 \cdot f_a(x_c^\ell, y_c^\ell) \cdot \left(\frac{1}{2}((1 - x_i^\ell) + (1 - x_t^\ell)) \cdot \frac{1}{2}((1 - y_i^\ell) + (1 - y_t^\ell))\right) \end{array} \right). \end{aligned}$$

Due to our model assumption of constant temperature on the tree,  $f_a(x, y) = C_a \cdot A_{\emptyset, s}$  with some positive constant  $C_a$  for the arterial tree.

<sup>1</sup>when we determined which segments lie within which grid cells, see Section 2.4

<sup>2</sup>Do not confuse this notation with the summation indices used before: here the two indices refer to the location of the support of  $\varphi$ .

Those four terms need to be computed and added up in the right hand side vector at the corresponding position for each grid cell for each segment intersecting that cell.

For the venous tree, the same formulas are used, the main difference is a negative  $C_v$  instead of  $C_a$ .

### 3.3 Steady State

If heating and cooling are constant in time and are in equilibrium and there is no flow of thermal energy into or out of the domain through the boundary, we expect the analytic solution to converge to a *steady state*. This is the case if

$$\begin{aligned} \int_{T_a} f_a + \int_{T_v} f_v &= 0 \\ \iff \int_{T_v} f_v &= - \int_{T_a} f_a. \end{aligned} \quad (3.9)$$

The steady state is characterized by  $\partial_t u = 0$ , the corresponding problem is to find  $u_\infty(x)$  satisfying

$$\begin{aligned} -\Delta_x u_\infty(x) &\stackrel{*}{=} f(x) \quad \text{in } \Omega \\ \partial_\nu u_\infty(x) &= 0 \quad \text{on } \partial\Omega \\ \int_\Omega u_\infty(x) &= 0. \end{aligned} \quad (3.10)$$

in a distributional sense.

The weak form is obtained by multiplying with test functions  $v \in V$ , integrating and using partial integration in space: Find  $u_\infty \in V$  such that

$$\int_\Omega \nabla u_\infty(x) \cdot \nabla v(x) \, dx = \int_\Omega f(x) \cdot v(x) \, dx \quad \forall v \in V. \quad (3.11)$$

**Proposition 3.3.1.** *If (3.9) holds, there is a solution  $u_\infty(x)$  to the weak steady-state problem (3.11).*

*Proof.* The compatibility relation ([5])  $\int_\Omega (RHS) = \int_{T_a \cup T_v} f = \int_{\partial\Omega} \partial_\nu u_\infty = 0$  holds. Let

$$\begin{aligned} a(u, v) &= \int_\Omega \nabla u \cdot \nabla v \\ l(v) &= \int_{T_a \cup T_v} f \cdot v \end{aligned}$$

where  $a : V \times V \rightarrow \mathbb{R}$  is obviously bilinear and  $l : V \rightarrow \mathbb{R}$  is linear. From Lemmas 3.1.1 and 3.1.2, we know that  $a$  is continuous and coercive.

So, by the Lax-Milgram theorem (Proposition 6.2.11), there is a solution to (3.11).  $\square$

The discrete version of (3.11) is

$$\begin{aligned} L\bar{U} &= F \\ \sum_i U_i &= (1, \dots, 1)\bar{U} = 0. \end{aligned}$$

Viewing this as an optimization problem

$$U = \operatorname{argmin}_{X \in \mathbb{R}^N} \frac{1}{2} LX \cdot X - F \cdot X$$

subject to  $(1, \dots, 1)X = 0$

we can introduce one *Lagrange multiplier*  $\mu$ , and combine the equations to

$$\left[ \begin{array}{c|c} L & \begin{matrix} 1 \\ \vdots \\ 1 \end{matrix} \\ \hline 1 & \dots & 1 & 0 \end{array} \right] \begin{bmatrix} \bar{U} \\ \mu \end{bmatrix} = \begin{bmatrix} F \\ 0 \end{bmatrix}. \quad (3.12)$$

The method of Lagrange multipliers is treated in [4], Chapter 3.

**Proposition 3.3.2.** *If (3.9) holds and  $f(t, x) = f(x)$  is constant in time, the solution  $U(t, x)$  to (3.6) converges to  $U_\infty \in V$  as  $t \rightarrow \infty$ .*

*Proof.* Consider the difference function  $W := U - U_\infty$ , then  $W$  satisfies

$$\partial_t W - \Delta_h W = F - F = 0 \quad (3.13)$$

where  $\Delta_h$  is a discretization of the Laplacian for which the eigenvectors<sup>3</sup> correspond to those eigenfunctions of the continuous Laplacian that can be represented on the grid [19]:

$$V_{p,q} = (\sin(p\pi jh) \cdot \sin(q\pi kh))_{j,k} \quad p, q \in \{0, \dots, N-1\}$$

where  $N$  is the number of unknowns in the grid in one dimension. This is a full set of linearly independent eigenvectors. The corresponding eigenvalues are  $\lambda_{p,q} = -\pi^2(p^2 + q^2)$ .

The solution to the system of ODEs (3.13) is given by

$$W(t) = e^{t\Delta_h} W_0,$$

so convergence depends on the sign of the eigenvalues of  $\Delta_h$ .

$\lambda_{0,0} = 0$ , and the corresponding eigenspace is  $\operatorname{span}(1, \dots, 1)^T$ , the one of constant vectors. Since  $U_0 = 0$ ,  $W_0 = U_0 - U_\infty$  and  $\int_\Omega u_\infty = 0$ , we have  $W(t) = 0 \forall t$ .

All other eigenvalues  $\lambda_{p,q}, (p, q) \neq 0, 0$  are strictly negative, so in either case  $W(t) \rightarrow 0$  as  $t \rightarrow \infty$ .  $\square$

*Remark 3.3.3.* Formally, we can argue similarly on the continuous problem. The solution to the initial value problem

$$\begin{aligned} \partial_t W &= \Delta W \\ W(0) &= W_0 \end{aligned}$$

is given by  $W(t) = e^{t\Delta} W_0$ .  $\Delta$  has a family of eigenvalues  $\lambda_{\alpha,\beta} = -\alpha^2 - \beta^2$  with corresponding eigenfunctions  $u_{\alpha,\beta}(x, y) = \sin(\alpha x) \cdot \sin(\beta y)$  for  $\alpha, \beta \in \mathbb{R}$ .

Again, all eigenvalues are negative except for one corresponding to constant functions, but they are arbitrarily close to zero, so convergence is arbitrarily slow.

<sup>3</sup>Despite the double indices these are vectors. Ordering depends on the ordering of the unknowns on the grid.

Finally, rewrite (3.9) for our source terms: By assumption,  $f_a, f_v$  correspond to constant temperatures on the trees, so (3.9) is equivalent to

$$\begin{aligned} \int_{T_v} f_v &= - \int_{T_a} f_a \\ \iff C_v \sum_{s \in T_v} A_{\mathcal{O},s} \cdot \ell_s &= -C_a \sum_{s \in T_a} A_{\mathcal{O},s} \cdot \ell_s. \end{aligned} \quad (3.14)$$

## 3.4 Implementation and Results

### 3.4.1 Heat Conduction

#### Implementation

We implemented this method in c++ using tools of the quocmesh library. For solving the system (3.8), we use a diagonally preconditioned conjugate gradient solver ([4]).

For the system (3.12), we use a block operator and multivectors, for solving the system, a conjugate gradient solver is used ([14, 4]).

#### Results

We used the first tree (16 terminal nodes) from Section 2.5.4, a  $257 \times 257$  grid and  $\tau = \frac{1}{512}$ . The values for the source term were set to  $C_a = 0.977436, C_v = -1.0$ , satisfying (3.14).

The output is linearly color-coded in the profile used before in Figure 2.10. Red corresponds to maximal temperature, green to zero temperature and blue to minimal temperature.

We can see the location of the segments in the position of heating and cooling in our domain, moreover the intensity is proportional to the cross section area of the segments. Computing those 50 time steps took 726 seconds on a desktop PC with a 1 GHz Athlon CPU.

### 3.4.2 Convergence to Steady State Solution

In order to check convergence to the steady state solution, we first compute the steady state solution for the same tree as above, this time the domain is discretized by a  $129 \times 129$  grid and we take  $\tau = \frac{1}{256}$ . The source values are the same as above. Computing the steady state solution and 300 time steps took 620 seconds.

We use the same color scale as before. A series of time steps is shown in Figure 3.2. At first, the influence of the source terms is hardly visible in the graphic, but at later time steps, we can see that the images look more and more similar to the steady state image.

In fact, computing the norm of the difference between the current time step and the steady state solution confirms this. Figure 3.3 shows a plot of the squared error in each time step relative to the squared norm of the steady state solution for the convergence experiment described. For this, we took  $17^2, 33^2, 65^2$  and  $129^2$  grids with timesteps  $\tau = \frac{1}{32}, \frac{1}{64}, \frac{1}{128}, \frac{1}{256}$ .

We can also see that the final relative error (where the convergence flattens out) is proportional to  $h$ . It is determined by the discretization error in  $M$  and  $L$ . This error can also be observed in the time stepping procedure: the  $\bar{U}^k$  do not satisfy  $(1, \dots, 1)\bar{U}^k = 0$  exactly even

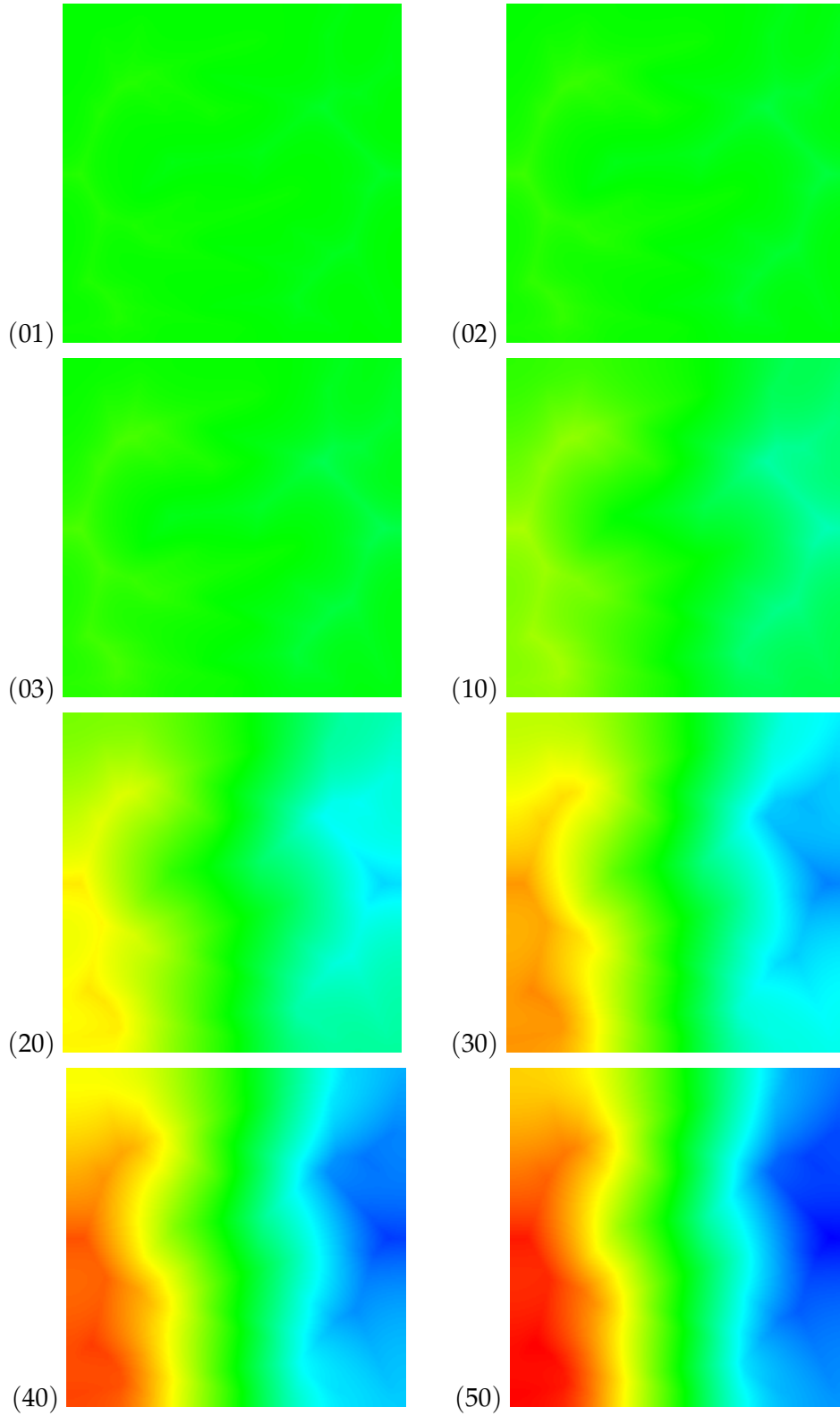


Figure 3.1: Time steps 1, 2, 3, 10, 20, 30, 40, 50 of the heat diffusion computation.

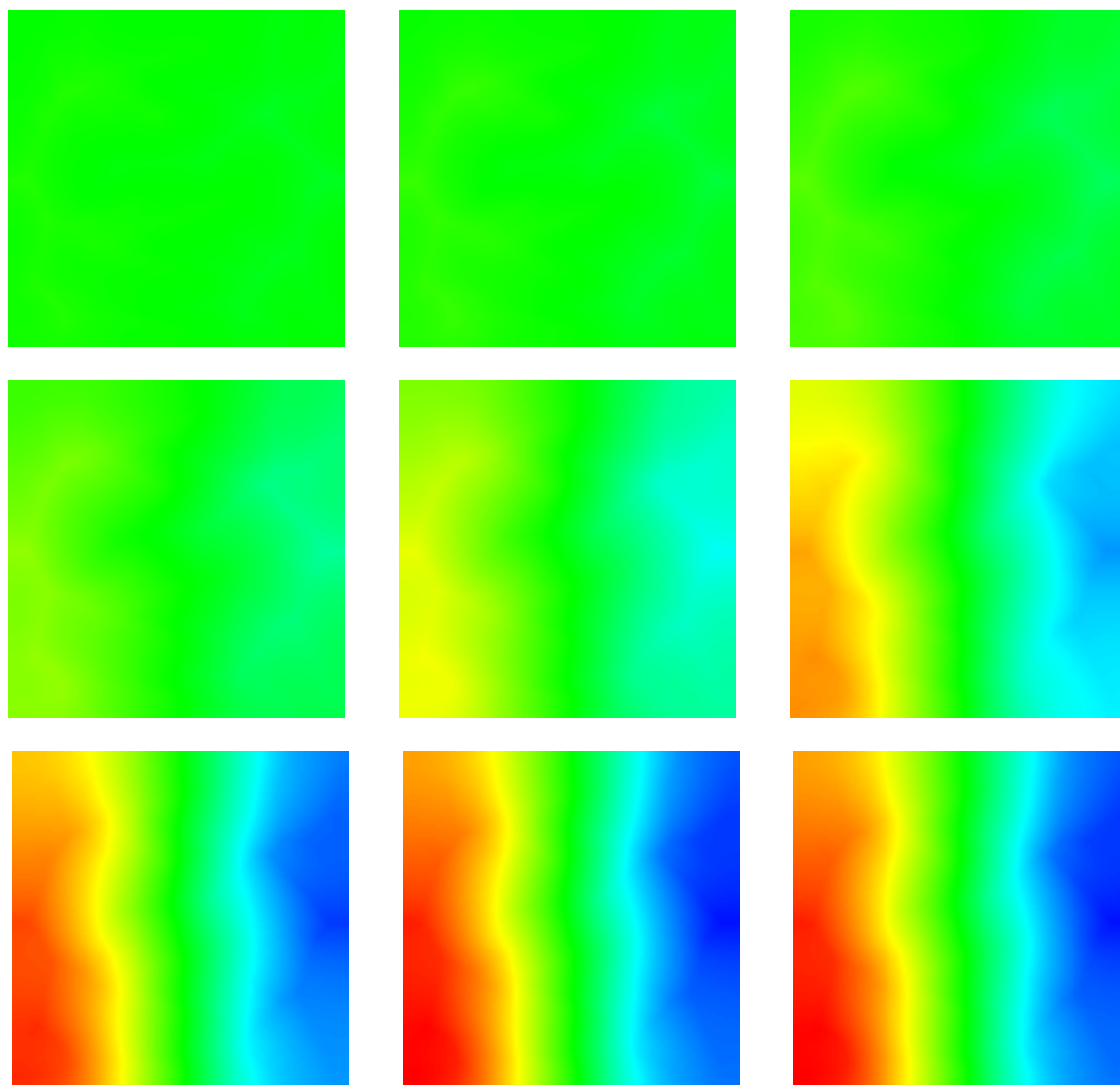


Figure 3.2: Convergence of time stepping solutions to the steady state solution:  
Time steps 1, 2, 4, 8, 16, 32, 64, 256, and the steady state solution.

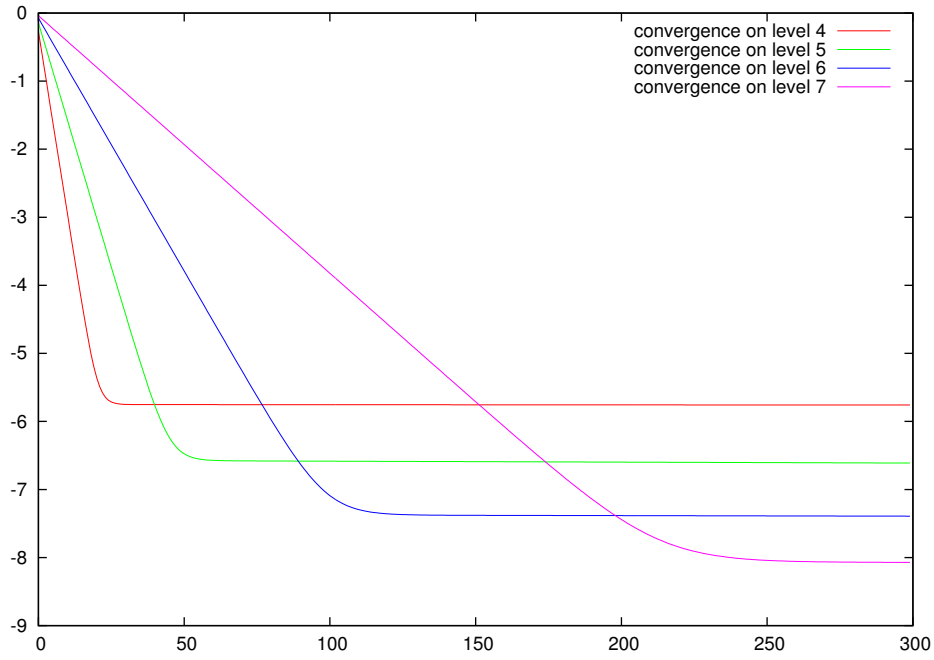


Figure 3.3: Convergence of time stepping solutions to the steady state solution: logarithmic plot of the squared norm of the difference relative to squared norm of the steady state solution (initial error) vs. time step on grid levels 4, 5, 6, 7.

though  $\bar{U}^0 = 0$ , but for sufficiently large  $k$ ,  $(1, \dots, 1)\bar{U}^k \approx (1, \dots, 1)\bar{U}^{k+1}$ . Computing these products on different grids, they also turn out to be  $O(h)$ .



## 4 Advection in Vessel Trees

This chapter deals with advection processes on the branching one-dimensional structure of the two types of vessel trees. The goal is to develop an *ELLAM* (Eulerian-Lagrangian locally adjoint method) to numerically solve the advection problem on these domains and to study the properties of this method. ELLAM was introduced by Celia, Russel and Herrera in [8].

On the vessel trees, we consider a function  $u = u_{\text{ves}}$  being an *energy content* in the sense of energy per length. On non-terminal segments, temperature is then given by  $\frac{1}{C\rho} \frac{u_{\text{ves}}}{A_{\emptyset}}$  where  $C$  is the specific heat capacity and  $\rho$  the density, whereas on terminal segments, energy content decreases to zero at the terminal nodes. We will see later in (4.48) and (4.52) how this is related to temperature.

In the plots in this chapter, we show temperature content defined as energy content at a point multiplied with the cross section area of the segment. On non-terminal segments, temperature content is proportional to temperature, on terminal segments, temperature content decreases to zero at terminal nodes.

The segments of the trees are considered to have constant radius and velocity, the velocities have to be such that mass is conserved at bifurcations ( $p \prec d, e$ ), ( $d, e \succ p$ ) splitting and combining flow:

$$A_{\emptyset,p} \cdot v_p = A_{\emptyset,d} \cdot v_d + A_{\emptyset,e} \cdot v_e.$$

So define the *flow splitting ratios*

$$\theta_d = \frac{A_{\emptyset,d} \cdot v_d}{A_{\emptyset,p} \cdot v_p}$$

$$\theta_e = \frac{A_{\emptyset,e} \cdot v_e}{A_{\emptyset,p} \cdot v_p}$$

where *mass conservation* above implies

$$\theta_d + \theta_e = \frac{A_{\emptyset,d} \cdot v_d + A_{\emptyset,e} \cdot v_e}{A_{\emptyset,p} \cdot v_p} = 1.$$

In the arterial tree, we specify an initial energy content profile, inflow into the root segment, moreover we assume continuous splitting of the temperature at bifurcations and outflow of energy along terminal segments such that the energy content drops down to zero at leaf nodes.

In the venous tree, we also specify an initial energy content profile and zero energy content at leaf nodes. We assume inflow of energy along terminal segments and weighted averaging of temperatures at bifurcations according to the flow splitting ratios.

We first state the continuous problems and the corresponding ELLAM forms for our advection problem on the two vessel trees, afterwards we show how this is built up step by step:

1. We start with a single nonterminal segment for which inflow is given.
2. As a next step we consider simple bifurcations, both  $\prec$  and  $\succ$ , to study how splitting and combination can be incorporated in our ELLAM framework. Again, inflow into parent ( $\prec$  case) or daughter ( $\succ$  case) segments is given.
3. Then we make one of the daughter segments in the bifurcation a terminal segment to present the appropriate source term for a terminal outflow / inflow segment.
4. Finally, we extend this to a pair of complete vessel trees.

Throughout this chapter, we consider two separate advection problems, one on the arterial tree and one on the venous tree. In order to keep notation reasonably simple, we use  $v, f$  and 1D interval representation for both trees. From the context, it will be clear which tree a given equation refers to.

All velocities  $v$  are assumed to be nonnegative.

## 4.1 Continuous and ELLAM Formulation

### 4.1.1 Continuous Advection Problems

We order the unknowns in the segments such that velocity is always positive and formulate the problems separately for the arterial and venous tree because the two processes have a different nature. In the arterial tree, we impose one inflow and compute many outflows (one for each leaf node), moreover, temperature splits continuously at bifurcations. In contrast, we have many inflows into the venous tree (one for each leaf node) and only one outflow condition, at each bifurcation we instantaneously obtain a weighted average of the two inflow temperatures (and energy contents), thus temperature (and energy content) is inherently discontinuous at bifurcations.

We map boundary data at inflow boundaries to initial data as explained below in equation (4.5). As the segments of our trees are represented by intervals in  $\mathbb{R}$ , we need to make sure that these intervals do not intersect when extending the support of initial data to the left. So let  $K \in \mathbb{N}$  from Section 2.1.3 be sufficiently large so that  $(j-1)K + \ell_{j-1} < jK - v_j T$  for all segments  $j$  when considering the time interval  $[0, T]$ .

#### Arterial Tree

The advection problem on the arterial tree with a source term and constant velocities on the segments during the time interval  $[0, T]$  is modeled by the initial-boundary value problem

$$\begin{aligned}
 \partial_t u(t, x) + v(x) \cdot \partial_x u(t, x) &= f(t, x) && \text{on } [0, T] \times T_a = [0, T] \times \bigcup_j [jK, jK + \ell_j] \\
 u(0, x) &= u_0(x) \\
 u(t, 0) &= u_{\text{root}}(t) \\
 u(t, pK + \ell_p) &= \frac{A_{\emptyset, p}}{A_{\emptyset, d}} \cdot u(t, dK) && \forall (p, d) \text{ parent and daughter}
 \end{aligned} \tag{4.1}$$

where  $f(t, x)$  is a source term,  $u_0(x)$  is an initial energy content distribution,  $v(x) = v(i)$  is constant on each of the segments above, inflow is given at the root and temperature is split continuously at bifurcations. This implies for any  $p$  parent of  $d$  and temperatures  $\vartheta$ :

$$\begin{aligned} \vartheta(t, pK + \ell_p) &= \vartheta(t, dK) \\ \Rightarrow \frac{1}{C\rho} \cdot \frac{u(t, pK + \ell_p)}{A_{\varnothing, p}} &= \frac{1}{C\rho} \cdot \frac{u(t, dK)}{A_{\varnothing, d}} \\ \Rightarrow u(t, pK + \ell_p) &= \frac{A_{\varnothing, p}}{A_{\varnothing, d}} \cdot u(t, dK). \end{aligned} \quad (4.2)$$

$f(t, x)$  consists of two parts,  $f(t, x) = f_w(t, x) + f_f(t, x)$ , where  $f_w$  describes source terms describing energy transfer between non-terminal vessel segments and surrounding tissue ("across the vessel walls"),  $f_f$  describes the energy transfer by outflow out of terminal segments along the whole segment. In our model,  $f_w$  is zero on terminal segments whereas  $f_f$  vanishes on non-terminal segments.

$f_f(t, x)$  is given by (see Section 4.4.1):

$$f_f(t, x) = v_j \cdot \frac{u(t, x)}{jK + \ell_j - x}.$$

### Venous Tree

On the venous tree, advection with a source term and constant velocities on the segments is modeled by the initial-boundary value problem

$$\begin{aligned} \partial_t u(t, x) + v(x) \cdot \partial_x u(t, x) &= f(t, x) \quad \text{on } [0, T] \times T_v = [0, T] \times \bigcup_j [jK, jK + \ell_j] \\ u(0, x) &= u_0(x) \\ u(t, jK) &= 0 \quad \forall j \text{ terminal segments} \\ u(t, pK) &= \frac{v_d}{v_p} \cdot u(t, dK + \ell_d) + \frac{v_e}{v_p} \cdot u(t, eK + \ell_e) \quad \forall (d, e) \succ p \text{ bifurcation} \end{aligned} \quad (4.3)$$

where  $f = f_w + f_f$  is a source term with  $f_w = 0$  on terminal segments and  $f_f = 0$  on non-terminal segments,  $u_0(x)$  is an initial energy content distribution,  $v$  is constant on each of the intervals above and temperature satisfies energy conservation when flow is combined at a bifurcation.

Energy conservation implies ( $C$  specific heat capacity in  $\frac{\text{J}}{\text{K} \cdot \text{kg}}$ ,  $\rho$  density<sup>1</sup> in  $\frac{\text{kg}}{\text{Vol}}$ ,  $\vartheta$  temperature in  $\text{K}$ ) for the limits of the function values at the bifurcation point in (4.3):

$$\begin{aligned} A_{\varnothing, p} v_p C\rho \cdot \vartheta(t, pK) &= A_{\varnothing, d} v_d C\rho \cdot \vartheta(t, dK + \ell_d) + A_{\varnothing, e} v_e C\rho \cdot \vartheta(t, eK + \ell_e) \\ \Rightarrow A_{\varnothing, p} v_p C\rho \cdot \frac{u(t, pK)}{A_{\varnothing, p}} &= A_{\varnothing, d} v_d C\rho \cdot \frac{u(t, dK + \ell_d)}{A_{\varnothing, d}} + A_{\varnothing, e} v_e C\rho \cdot \frac{u(t, eK + \ell_e)}{A_{\varnothing, e}} \\ \Rightarrow u(t, pK) &= \frac{v_d}{v_p} \cdot u(t, dK + \ell_d) + \frac{v_e}{v_p} u(t, eK + \ell_e). \end{aligned} \quad (4.4)$$

<sup>1</sup>Vol is two-dimensional volume here in our two-dimensional setting.

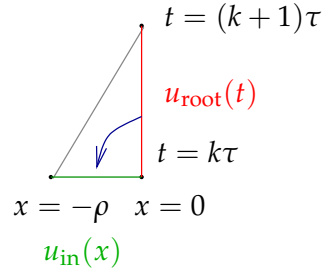


Figure 4.1: Sketch for mapping boundary data to initial data.

Note that energy content at leaf nodes is set to zero, so inflow into venous terminal segments is not given by boundary conditions at leaf nodes. Instead, we impose a source term  $f_f(x)$  on those segments, see Section 4.4.2:

$$f_f(t, x) = \frac{A_{\emptyset} v}{\ell} u_{\text{surr}}(t, x)$$

where  $u_{\text{surr}}$  is the energy density of the surrounding tissue ( $\frac{J}{\text{Vol}}$ ).

#### 4.1.2 Existence of Solutions

In Proposition 4.2.1, we show that there exists a unique solution for the advection problem on a single segment with sufficiently smooth initial and inflow boundary data.

This covers all types of segments of both trees except for terminal segments in the arterial tree that have a different RHS term in the corresponding PDE. For those segments, existence of a unique solution is shown in Section 4.4.1.

#### Arterial Tree

For our numerical method, we map boundary (root) conditions  $u_{\text{root}}(t \geq 0)$  of the arterial tree to initial data  $u_{\text{in}}$  on an inflow domain, see Figure 4.1:

$$u_{\text{in}}(x) := u_{\text{root}}\left(\frac{-1}{v} \cdot x\right) \quad \forall x \in [vT, 0). \quad (4.5)$$

Define extended initial data and source terms for the arterial tree:

$$\tilde{u}_0(x) := \begin{cases} u_{\text{in}}(x) & \text{for } x \in [-vT, 0) \\ u_0(x) & \text{for } x \in T_a = \bigcup_j [jK, jK + \ell_j] \\ 0 & \text{else} \end{cases} \quad (4.6)$$

$$\tilde{f}(x) := \begin{cases} 0 & \text{for } x \in [-vT, 0) \\ f(x) & \text{for } x \in T_a = \bigcup_j [jK, jK + \ell_j] \\ 0 & \text{else.} \end{cases} \quad (4.7)$$

There is no inflow represented at leaf nodes of the arterial tree.

The advection problem on the arterial tree consists of coupled advection problems: outflow out of upflow segments determines inflow to subsequent segments in downflow direction.

From this, we can conclude that there exists a solution for the transport problem on the arterial vessel tree if the extended initial data  $\tilde{u}_0$  and source  $\tilde{f}$  are sufficiently smooth:

**Proposition 4.1.1** (Existence of Solution for the Arterial Tree). *If*

$$\tilde{f}|_{T_a} \in C^0(T_a), \quad \tilde{u}_0|_{T_a \cup [-vT, 0]} \in C^1(T_a \cup [-vT, 0])$$

and  $\tilde{f}, \tilde{u}_0, \tilde{u}'_0$  satisfy the bifurcation limits in problem (4.1), there is a unique solution to the continuous advection problem on the arterial tree.

*Proof.* The solution is obtained by tracing back along the characteristics as in Section 4.2.1 through the branching structure considering the source terms. For a more detailed discussion of advection equations, we refer to [32].  $\square$

This is satisfied if  $f \in C^0(T_a)$ ,  $u_0 \in C^1(T_a)$ ,  $u_{\text{root}} \in C^1([0, T])$ , the transition between  $u_0$  and  $u_{\text{root}}$  at the origin, namely  $\tilde{u}_0|_{\mathbb{B}_\epsilon(0)}$ , is  $C^1$ , and  $f, u_0, u'_0$  satisfy the bifurcation limits.

### Venous Tree

For the venous tree, we have zero boundary conditions at the leaf nodes, so  $u_0(x)$  is extended by 0 outside of  $T_v$ . Here,

$$\tilde{u}_0(x) := \begin{cases} 0 & \text{for } x \in [iK - vT, iK) \text{ for all terminal segments } i \\ u_0(x) & \text{for } x \in T_v = \bigcup_j [jK, jK + \ell_j] \\ 0 & \text{else} \end{cases} \quad (4.8)$$

$$\tilde{f}(x) := \begin{cases} 0 & \text{for } x \in [iK - vT, iK) \text{ for all terminal segments } i \\ f(x) & \text{for } x \in T_v = \bigcup_j [jK, jK + \ell_j] \\ 0 & \text{else.} \end{cases} \quad (4.9)$$

$$(4.10)$$

Again, our transport model consists of coupled advection problems and we get a unique solution if  $\tilde{u}_0$  and  $\tilde{f}$  are sufficiently smooth and satisfy bifurcation and boundary conditions:

**Proposition 4.1.2** (Existence of Solution for the Venous Tree). *If*

$$\tilde{f}|_{T_v} \in C^0(T_v), \quad \tilde{u}_0|_{T_v} \in C^1(T_v),$$

$\tilde{u}_0(jK) = 0$  for all terminal segments  $j$  and  $\tilde{f}, \tilde{u}_0, \tilde{u}'_0$  satisfy the bifurcation limits in problem (4.3), there is a unique solution to the continuous advection problem on the venous tree.

*Proof.*  $\tilde{u}_0(jK) = 0$  for all terminal segments  $j$  implies that

$$\tilde{u}_0|_{T_v \cup \bigcup_{i \text{ terminal segment}} [iK - vT, iK)} \in C^1\left(T_v \cup \bigcup_{i \text{ terminal segment}} [iK - vT, iK)\right). \quad (4.11)$$

The solution is obtained by tracing back along the characteristics as in Section 4.2.1 through the branching structure.  $\square$

### 4.1.3 ELLAM Formulation

Our aim is to discretize the advection PDE using an *ELLAM* (Eulerian-Lagrangian locally adjoint method) as described by Celia et. al in [8]. ELLAM involves obtaining a weak formulation of the advection problem using test functions that are constant along characteristic curves of the PDE, i. e. test functions  $w$  satisfying

$$-\partial_t w(t, x) - v_j \cdot \partial_x w(t, x) = 0 \quad (4.12)$$

on each segment  $j$  during one time step of the calculation. For this purpose, the interval  $[0, T]$  is split into a finite number time steps  $t^0, \dots, t^R, t^k = k \cdot \tau, t^R = T$ .

### Function Spaces

At an arterial bifurcation,  $p_{\text{term}}$  is the downflow node of  $p$ , it coincides with  $d_{\text{init}}$  and  $e_{\text{init}}$ , the upflow nodes of  $d, e$ . At a venous bifurcation,  $d_{\text{init}}$  and  $e_{\text{init}}$  are the downflow nodes of  $d, e$  and coincide with  $p_{\text{term}}$ , the upflow node of  $p$ .

To use a more intuitive notation that respects the direction of flow, we write  $p_{\text{downf}}, d_{\text{upf}}$  and  $e_{\text{upf}}$  in the arterial case and  $d_{\text{downf}}, e_{\text{downf}}$  and  $p_{\text{upf}}$  in the venous case.

Define the following function spaces for  $u(t, \cdot)$  for fixed time  $t$ : for the arterial vesseltree  $T_a = \bigcup_i S_{a,i}$ , (4.2) says how to choose the function space:

$$\begin{aligned} H_a &:= H^1(T_a) := \left\{ u \mid u|_{S_{a,i}} \in H^1(S_{a,i}) \forall i \right\} \\ \|u\|_{H_a} &= \sum_i \|u\|_{H^1(S_{a,i})} \\ V_a &= \left\{ u \in H_a \mid u(p_{\text{downf}}) = \frac{A_{\emptyset,p}}{A_{\emptyset,d}} u(d_{\text{upf}}) = \frac{A_{\emptyset,p}}{A_{\emptyset,e}} u(e_{\text{upf}}) \forall (p \prec d, e) \text{ bifurcation} \right\} \end{aligned}$$

and the venous vesseltree  $T_v = \bigcup_i S_{v,i}$ , (4.4) says how to choose the function space:

$$\begin{aligned} H_v &:= H^1(T_v) := \left\{ u \mid u|_{S_{v,i}} \in H^1(S_{v,i}) \forall i \right\} \\ \|u\|_{H_v} &= \sum_i \|u\|_{H^1(S_{v,i})} \\ V_v &= \left\{ u \in H_v \mid u(p_{\text{upf}}) = \frac{v_d}{v_p} u(d_{\text{downf}}) + \frac{v_e}{v_p} u(e_{\text{downf}}) \forall (d, e \succ p) \text{ bif.}, u(l_{\text{upf}}) = 0 \forall l \text{ leaf} \right\}. \end{aligned}$$

Note that by Proposition 6.2.9,  $H^1$  functions on open intervals are continuous on the closure of these intervals, so the function spaces above are well-defined.

$V_a, V_v$  are the spaces of  $H^1$  functions describing feasible  $u$  profiles on the arterial and the venous tree respectively. In particular, these function spaces incorporate the coupling conditions for bifurcations.

$V_a \subset H_a$  and  $V_v \subset H_v$  are closed and convex subsets, see Lemmas 4.1.3 and 4.1.4 at the end of this section.

For a fixed time step  $k$ , define the following function spaces for the test functions  $w^{k+1}$ :

$$\begin{aligned} \tilde{W}_a &= \{w \in H_a \mid w(p_{\text{downf}}) = \theta_d \cdot w(d_{\text{upf}}) + \theta_e \cdot w(e_{\text{upf}}) \ \forall (p \prec d, e) \text{ bifurcation} \} \\ W_a^{k+1} &:= \left\{ w : [k\tau, (k+1)\tau] \times T_a \rightarrow \mathbb{R} \left| \begin{array}{l} w(t, \cdot) \in \tilde{W}_a \ \forall t \\ \wedge w(\cdot, x) \in C^{0,1}([k\tau, (k+1)\tau]) \ \forall x \\ \wedge -\partial_t w(t, x) - v(x)\partial_x w(t, x) = 0 \ \forall t, x \end{array} \right. \right\} \\ \tilde{W}_v &= \{w \in H_v \mid w(p_{\text{upf}}) = w(d_{\text{downf}}) = w(e_{\text{downf}}) \ \forall (d, e \succ p) \text{ bifurcation} \} \\ W_v^{k+1} &:= \left\{ w : [k\tau, (k+1)\tau] \times T_v \rightarrow \mathbb{R} \left| \begin{array}{l} w(t, \cdot) \in \tilde{W}_v \ \forall t \\ \wedge w(\cdot, x) \in C^{0,1}([k\tau, (k+1)\tau]) \ \forall x \\ \wedge -\partial_t w(t, x) - v(x)\partial_x w(t, x) = 0 \ \forall t, x \end{array} \right. \right\}. \end{aligned}$$

$W_a^{k+1}, W_v^{k+1}$  are the spaces of test functions describing advection with mass conservation. In case of the arterial tree, mass is split  $\theta_d : \theta_e$  between the two daughters at a bifurcation, so only a fraction of the mass flowing out of an upstream segment flows into one given downstream segment. In the venous tree, this is different: all the mass flowing out of an upstream (daughter) segment flows into the downstream (parent) segment. Hence the coupling conditions in the  $\tilde{W}$  spaces are different.

Note that there is duality to some extent:  $V_a$  and  $\tilde{W}_v$  have a similar structure, so do  $V_v$  and  $\tilde{W}_a$ . The structures are not the same, however, because coupling conditions in  $V_{a,v}$  involve an additional factor  $\frac{A_{\mathcal{Q},p}}{A_{\mathcal{Q},d}}$  compared to the conditions in  $W_{v;a}^{k+1}$ .

This is due to the different nature of the two bifurcations: if flow is split, temperature is continuous, if flow is combined, temperatures (and energy contents) are averaged discontinuously.

Also note that there is no continuity requirement for test functions from one time step to the next, i. e.

$$w^{k+1}(t, x) \cdot \chi_{(k\tau, (k+1)\tau)} + w^{k+2}(t, x) \cdot \chi_{((k+1)\tau, (k+2)\tau)}, \quad w^{k+1} \in W_{a,v}^{k+1}, w^{k+2} \in W_{a,v}^{k+2} \quad (4.13)$$

does not have a continuous extension to  $t = (k+1)\tau$  for fixed  $x$ .

Now we can state the weak formulation of the advection problems for the  $k$ th time step obtained by integration in both space and time:

### Arterial Tree

Given  $f \in L^2((0, T), V_a)$  (this space is defined in (3.2)),  $u_0 \in V_a$  and  $u_{\text{root}} \in L^2([0, T])$ , find

$$u \in L^2((0, T); V_a) \cap C^0([0, T]; L^2(T_a))$$

such that

$$\begin{aligned} \int_{T_a} \int_{k\tau}^{(k+1)\tau} (\partial_t u(t, x) + v(x)\partial_x u(t, x)) \cdot w(t, x) \, dt \, dx &= \int_{T_a} \int_{k\tau}^{(k+1)\tau} f(x)w(t, x) \, dt \, dx \quad \forall w \in W_a^{k+1} \\ u(0, x) &= u_0(x) \\ u(t, 0) &= u_{\text{root}}(t) \end{aligned} \quad (4.14)$$

holds for each  $k \in \{1, \dots, R\}$ .

### Venous Tree

Given  $f \in L^2((0, T), V_v)$  and  $u_0 \in V_v$ , find

$$u \in L^2((0, T); V_v) \cap C^0([0, T]; L^2(T_v)) \quad (4.15)$$

such that

$$\begin{aligned} \int_{T_v} \int_{k\tau}^{(k+1)\tau} (\partial_t u(t, x) + v(x) \partial_x u(t, x)) \cdot w(t, x) \, dt \, dx &= \int_{T_v} \int_{k\tau}^{(k+1)\tau} f(x) w(t, x) \, dt \, dx \quad \forall w \in W_v^{k+1} \\ u(0, x) &= u_0(x) \\ u(t, jK) &= 0 \quad \forall j \text{ terminal segment} \end{aligned} \quad (4.16)$$

holds for each  $k \in \{1, \dots, R\}$ .

**Lemma 4.1.3.**  $V_a \subset H_a$  is convex and closed.

*Proof.* Convexity: We have for  $\lambda \in [0, 1]$  and  $v_1, v_2 \in V_a$ :

$$\begin{aligned} &(v_1(p_{\text{downf}}) + \lambda(v_2(p_{\text{downf}}) - v_1(p_{\text{downf}}))) \\ &= \frac{A_{\emptyset, p}}{A_{\emptyset, d}} v_1(d_{\text{upf}}) + \lambda \left( \frac{A_{\emptyset, p}}{A_{\emptyset, d}} v_2(d_{\text{upf}}) - \frac{A_{\emptyset, p}}{A_{\emptyset, d}} v_1(d_{\text{upf}}) \right) \\ &= \frac{A_{\emptyset, p}}{A_{\emptyset, d}} (v_1(d_{\text{upf}}) + \lambda(v_2(d_{\text{upf}}) - v_1(d_{\text{upf}}))). \end{aligned}$$

Closedness: Show that  $\forall w \in H_a \setminus V_a \exists \epsilon > 0$ :

$$\mathbb{B}_\epsilon(w) := \{\tilde{w} \in H_a \mid \|w - \tilde{w}\|_{H_a} < \epsilon\} \subset H_a \setminus V_a,$$

this is equivalent to  $V_a$  being closed subset of  $H_a$ .

For  $w \in H_a \setminus V_a$ , there exists at least one bifurcation at which the limit condition is not satisfied. Let  $p, d$  be the lexicographically first pair of parent, daughter segment at such bifurcations. Let  $C_b := \frac{A_{\emptyset, p}}{A_{\emptyset, d}}$ . Then

$$w(p_{\text{downf}}) - \frac{A_{\emptyset, p}}{A_{\emptyset, d}} w(d_{\text{upf}}) =: \delta(w) = \delta \neq 0.$$

For any fixed  $v \in V_a$ ,  $f := v - w$ ,  $\delta(f) = \delta(w)$ .

Let  $\eta = \min\left(|\delta|, \frac{|\delta|}{C_b}\right)$ , then by Lemma 6.2.15,

$$|f(p_{\text{downf}})| \geq \frac{\eta}{2} \vee |f(d_{\text{upf}})| \geq \frac{\eta}{2}.$$

By Lemma 6.2.14, we obtain

$$\begin{aligned} \|w - v\|_{H_a} &\geq \min\left(\frac{1}{8} \sqrt{\ell_p} \eta, \frac{1}{4\sqrt{\ell_p}} \eta\right) \\ \vee \quad \|w - v\|_{H_a} &\geq \min\left(\frac{1}{8} \sqrt{\ell_d} \eta, \frac{1}{4\sqrt{\ell_d}} \eta\right). \end{aligned}$$

Thus

$$\|w - v\|_{H_a} \geq \min \left( \frac{1}{8} \sqrt{\ell_p} \eta, \frac{1}{4\sqrt{\ell_p}} \eta, \frac{1}{8} \sqrt{\ell_d} \eta, \frac{1}{4\sqrt{\ell_d}} \eta \right) =: \epsilon$$

and  $\epsilon$  is strictly greater than zero and depends on  $w$  and the tree but not on  $v$ , so we have shown that  $H_a \setminus V_a$  is open in  $H_a$ .  $\square$

**Lemma 4.1.4.**  $V_v \subset H_v$  is convex and closed.

*Proof.* Convexity: Again, this is the easier part. Let  $j$  be a terminal segment in the venous tree,  $(d, e \succ p)$  be a bifurcation,  $\lambda \in [0, 1]$  and  $v_1, v_2 \in V_v$ :

$$\begin{aligned} & v_1(j_{\text{upf}}) + \lambda(v_2(j_{\text{upf}}) - v_1(j_{\text{upf}})) \\ &= 0 + \lambda(0 - 0) = 0 \end{aligned}$$

and

$$\begin{aligned} & v_1(p_{\text{upf}}) + \lambda(v_2(p_{\text{upf}}) - v_1(p_{\text{upf}})) \\ &= \frac{v_d}{v_p} v_1(d_{\text{downf}}) + \frac{v_e}{v_p} v_1(e_{\text{downf}}) + \lambda \left( \frac{v_d}{v_p} v_2(d_{\text{downf}}) + \frac{v_e}{v_p} v_2(e_{\text{downf}}) - \frac{v_d}{v_p} v_1(d_{\text{downf}}) - \frac{v_e}{v_p} v_1(e_{\text{downf}}) \right) \\ &= \frac{v_d}{v_p} (v_1(d_{\text{downf}}) + \lambda(v_2(d_{\text{downf}}) - v_1(d_{\text{downf}}))) + \frac{v_e}{v_p} (v_1(e_{\text{downf}}) + \lambda(v_2(e_{\text{downf}}) - v_1(e_{\text{downf}}))). \end{aligned}$$

Closedness: As before, we show that  $\forall w \in H_v \setminus V_v \exists \epsilon > 0$ :

$$\mathbb{B}_\epsilon(w) := \{\tilde{w} \in H_v \mid \|w - \tilde{w}\|_{H_v} < \epsilon\} \subset H_v \setminus V_v,$$

this is equivalent to  $V_v$  being closed subset of  $H_v$ .

For  $w \in H_v \setminus V_v$ , there exists at least one terminal segment  $j$  where the boundary condition is not satisfied or at least one bifurcation  $(d, e; p)$  at which the limit condition is not satisfied.

In the first case, let  $j$  be the troublesome terminal segment with smallest index, let  $\delta(w) = w(j, \text{downf}) = \delta(w - v) = \delta(f) =: \delta$  for all  $v \in V_v, f := w - v$ . Then, by Lemma 6.2.14, we get

$$\|w - v\|_{H_v} \geq \min \left( \frac{1}{4} \sqrt{\ell_j} \delta, \frac{1}{2\sqrt{\ell_j}} \delta \right) =: \epsilon.$$

In the second case, let  $(d, e \succ p)$  be the first troublesome bifurcation with indices in lexicographical ordering and define

$$v(p_{\text{upf}}) - \frac{v_p}{v_d} v(d_{\text{downf}}) - \frac{v_p}{v_e} v(e_{\text{downf}}) =: \delta(w) = \delta \neq 0.$$

For  $v \in V_v, f := v - w$ , we have  $\delta(f) = \delta(w)$ .

Let  $\eta = \min \left( |\delta|, \frac{v_d}{v_p} |\delta|, \frac{v_e}{v_p} |\delta| \right)$ , then by Lemma 6.2.15, we get

$$|f(p_{\text{upf}})| \geq \frac{\eta}{3} \vee |f(d_{\text{downf}})| \geq \frac{\eta}{3} \vee |f(e_{\text{downf}})| \geq \frac{\eta}{3}.$$

Again, Lemma 6.2.14 implies

$$\begin{aligned}\|w - v\|_{H_v} &\geq \min\left(\frac{1}{12}\sqrt{\ell_p}\eta, \frac{1}{6\sqrt{\ell_p}}\eta\right) \\ \forall \|w - v\|_{H_v} &\geq \min\left(\frac{1}{12}\sqrt{\ell_d}\eta, \frac{1}{6\sqrt{\ell_d}}\eta\right) \\ \forall \|w - v\|_{H_v} &\geq \min\left(\frac{1}{12}\sqrt{\ell_e}\eta, \frac{1}{6\sqrt{\ell_e}}\eta\right).\end{aligned}$$

Thus

$$\|w - v\|_{H_v} \geq \min\left(\frac{1}{12}\sqrt{\ell_{\{p,d,e\}}}\eta, \frac{1}{6\sqrt{\ell_{\{p,d,e\}}}}\eta\right) =: \epsilon.$$

In any case,  $\epsilon > 0$  independent of  $v$ , so we have shown that  $H_v \setminus V_v$  is open in  $H_v$ .  $\square$

## 4.2 ELLAM on a Single Segment

### 4.2.1 Continuous Problem

Advection on a single segment of length  $\ell$  and for constant velocity  $v > 0$ , during the time interval  $[0, T]$  with a source term  $f$  and initial conditions  $u_0$  is described by the initial-boundary value problem

$$\begin{aligned}\partial_t u(t, x) + v \cdot \partial_x u(t, x) &= f(t, x) && \text{in } [0, T] \times [0, \ell] \\ u(t, 0) &= u_{\text{root}}(t) && \text{in } [0, \ell] \\ u(0, x) &= u_0(x) && \text{in } [0, T]\end{aligned}\tag{4.17}$$

with  $u_{\text{root}}(t = 0) = u_0(x = 0)$ .

Here, mapping boundary conditions to an inflow domain and extending initial data and source looks as follows:

$$\begin{aligned}\tilde{u}_0(x) &:= \begin{cases} u_{\text{in}}(x) & \text{for } x \in [-vT, 0) \\ u_0(x) & \text{for } x \in [0, \ell] \\ 0 & \text{else} \end{cases} \\ \tilde{f}(x) &:= \begin{cases} 0 & \text{for } x \in [-vT, 0) \\ f(x) & \text{for } x \in [0, \ell] \\ 0 & \text{else.} \end{cases}\end{aligned}$$

First we show the existence and uniqueness of a solution to this problem for sufficiently smooth data and  $f$  constant in time:

**Proposition 4.2.1.** *Let  $f \in C^0(\mathbb{R})$ ,  $u_0 \in C^1(\mathbb{R})$ ,  $v > 0$ . Then the problem*

$$\begin{aligned}\partial_t u(t, x) + v \cdot \partial_x u(t, x) &= f(x) && (t, x) \in [0, \infty) \times \mathbb{R} \\ u(0, x) &= u_0(x) && \text{on } \{0\} \times \mathbb{R}\end{aligned}$$

has a unique solution given by

$$u(t, x) = u_0(x - vt) + \int_{x-vt}^x \frac{1}{v} \cdot f(\xi) \, d\xi. \quad (4.18)$$

*Proof.* The solution is obtained by tracing back along the characteristics. We show that it is in fact a solution: Let  $F(x) := \int_{x_0}^x \frac{1}{v} f(\xi) \, d\xi$  for some  $x_0 \in \mathbb{R}$ , then

$$\begin{aligned} \int_{x-vt}^x \frac{1}{v} \cdot f(\xi) \, d\xi &= F(x) - F(x - vt) \\ u(t, x) &= u_0(x - vt) + F(x) - F(x - vt) \\ \partial_t u(t, x) &= u'_0(x - vt) \cdot (-v) - F'(x - vt) \cdot (-v) \\ \partial_x u(t, x) &= u'_0(x - vt) + F'(x) - F'(x - vt) \cdot 1 \\ \Rightarrow \partial_t u(t, x) + v \cdot \partial_x u(t, x) &= u'_0(x - vt) \cdot (-v) - F'(x - vt) \cdot (-v) \\ &\quad + v (u'_0(x - vt) + F'(x) - F'(x - vt)) \\ &= v \cdot F'(x) = v \cdot \frac{1}{v} \cdot f(x) = f(x). \end{aligned}$$

To show uniqueness, let  $s(t, x)$  be any solution of the initial value problem, then the difference function  $d(t, x) = s(t, x) - u(t, x)$  must satisfy

$$\begin{aligned} \partial_t d(t, x) + v \partial_x d(t, x) &= 0 \quad (t, x) \in [0, \infty) \times \mathbb{R} \\ d(0, x) &= 0 \quad \text{on } \{0\} \times \mathbb{R}, \end{aligned}$$

hence  $d(t, x) = 0 \, \forall (t, x) \in [0, \infty) \times \mathbb{R}$ , so  $s = u$ .  $\square$

*Remark 4.2.2.* Values of the extended functions  $\tilde{f}$  and  $\tilde{u}_0$  outside of the interval  $[-vT, \ell]$  are irrelevant for our solution.

*Remark 4.2.3.* For (4.18) to make sense,  $f$  need not be continuous on all  $\mathbb{R}$ .

Suppose  $f \in C^0([0, \ell])$ , but  $f(0) \neq 0$ . Then for any  $\epsilon > 0$ ,  $f|_{[\epsilon, \ell]}$  can be extended to a  $C^0(\mathbb{R})$  function satisfying

$$\hat{f}(x) = \begin{cases} 0 & x \leq 0 \\ \epsilon \cdot f(\epsilon) & 0 < x < \epsilon \\ f(x) & \epsilon \leq x \leq \ell \\ f(\ell) & x > \ell \end{cases}$$

and  $u, \hat{u}$ , the solutions for  $f, \hat{f}$  as in (4.18), satisfy:

$$\begin{aligned} \hat{u}(t, x) &= u_0(x - vt) + \frac{1}{v} \int_{x-vt}^x \hat{f}(\xi) \, d\xi \\ &= u_0(x - vt) + \frac{1}{v} \int_0^\epsilon \hat{f}(\xi) \, d\xi + \frac{1}{v} \int_\epsilon^x \hat{f}(\xi) \, d\xi \\ &= u_0(x - vt) + \frac{1}{v} \int_\epsilon^x f(\xi) \, d\xi + O(\epsilon) \\ &= u_0(x - vt) + \frac{1}{v} \int_0^x f(\xi) \, d\xi - O(\epsilon) + O(\epsilon) \\ &= u(t, x) + O(\epsilon) \end{aligned}$$

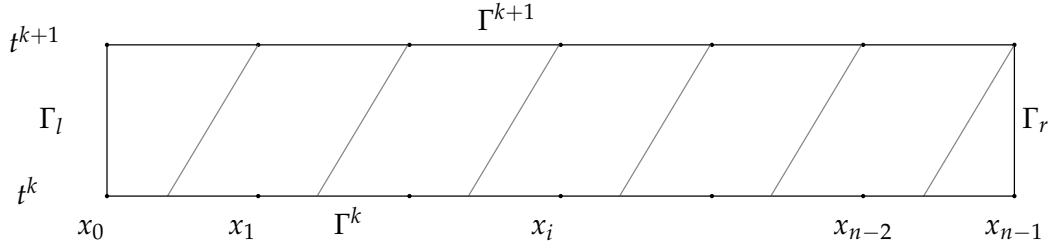


Figure 4.2: Boundary sets for a single ELLAM time step in case of Dirichlet boundary conditions

because  $f \in C^0([0, \ell])$  implies that  $f$  is bounded.

So we get a unique solution for any  $f \in C^0([0, \ell])$ .

*Remark 4.2.4.* Proposition 4.2.1 also holds if  $f$  is not constant in time, but sufficiently smooth. In this case, we also need to integrate the source term  $f(t, x)$  along the characteristic as we trace back to the initial condition.

So for our purposes, we state the following existence result:

**Proposition 4.2.5.** *If  $f \in C^0([0, T] \times [0, \ell])$  and  $u_0$  and  $u_{\text{root}}$  are such that  $\tilde{u}_0 \in C^1([-vT, \ell])$ , problem (4.17) has a unique solution given by*

$$u(t, x) = \tilde{u}_0(x - vt) + \int_{x-vt}^x \frac{1}{v} \cdot \tilde{f}(\xi) d\xi. \quad (4.19)$$

#### 4.2.2 Temporal Discretization using ELLAM

For the spatial discretization we use a one-dimensional grid with equidistant grid points  $x_0 = 0, x_i = i \cdot h, x_n = \ell$  with grid width  $h = \frac{\ell}{n}$ , the temporal discretization is  $t^0 = 0, t^k = k \cdot \tau, \dots, t^m = T$  with temporal grid width  $\tau = \frac{T}{m}$ .

Let  $h$  and  $\tau$  be sufficiently small that the grid has least four nodes and

$$\rho := \frac{v \cdot \tau}{h} \leq 1. \quad (4.20)$$

$\rho$  is a scaling factor for the velocity so that  $\rho \cdot v$  is the velocity in grid cells per time step.

The first condition guarantees that in our discretization and time stepping, we do not have to consider inflow and outflow within the same ELLAM equation. As for the second condition, we will explain the generalization to bigger  $\rho > 1$  after treating the case  $\rho \leq 1$ .

As mentioned before, we write a weak form of the advection problem using test functions that satisfy (4.12).

For a single time step, we define the sets  $\Gamma$  shown in Figure 4.2 and derive the weak formulation by first testing with functions  $w \in W_1^{k+1}$

$$\int_0^\ell \int_{t^k}^{t^{k+1}} (\partial_t + v \cdot \partial_x) u \cdot w = \int_0^\ell \int_{t^k}^{t^{k+1}} f \cdot w \quad (4.21)$$

and then integrating by parts

$$\begin{aligned}
&\Rightarrow \int_{\Gamma^{k+1}} u(t^{k+1}, x) \cdot w(t^{k+1}, x) \, dx - \int_{\Gamma^k} u(t^k, x) \cdot w(t^k, x) \, dx \\
&\quad + \int_0^\ell \int_{t^k}^{t^{k+1}} u(t, x) (-\partial_t - v \cdot \partial_x) w(t, x) \, dt \, dx \\
&\quad + v \cdot \int_{\Gamma_r} u(t, \ell) w(t, \ell) \, dt - v \cdot \int_{\Gamma_l} u(t, 0) w(t, 0) \, dt = \int_0^\ell \int_{t^k}^{t^{k+1}} f(t, x) \cdot w(t, x) \, dx \, dt
\end{aligned} \tag{4.22}$$

where

$$\begin{aligned}
H_1 &:= H^1((0, \ell)) \\
V_1 &:= H_1 \\
W_1^{k+1} &:= \left\{ w : [t^k, t^{k+1}] \times [0, \ell] \rightarrow \mathbb{R} \mid \begin{array}{l} w(t, \cdot) \in H_1 \, \forall t \wedge w(\cdot, x) \in C^{0,1}([t^k, t^{k+1}]) \, \forall x \\ \wedge -\partial_t w(t, x) - v(x) \partial_x w(t, x) = 0 \, \forall t, x \end{array} \right\}.
\end{aligned}$$

Because of equation (4.12), the third integral on the left hand side of (4.22) drops out and we obtain the weak ELLAM formulation of the advection problem for a single segment:

Given  $f \in L^2((0, T), V_1)$ ,  $u_0 \in V_1$  and  $u_{\text{in}} \in L^2([0, T])$ , find

$$u \in L^2((0, T); V_1) \cap C^0([0, T]; L^2(T_a))$$

such that

$$\begin{aligned}
&\int_{\Gamma^{k+1}} u(t^{k+1}, x) \cdot w(t^{k+1}, x) \, dx - \int_{\Gamma^k} u(t^k, x) \cdot w(t^k, x) \, dx \\
&\quad + v \cdot \int_{\Gamma_r} u(t, \ell) w(t, \ell) \, dt - v \cdot \int_{\Gamma_l} u(t, 0) w(t, 0) \, dt = \int_0^\ell \int_{t^k}^{t^{k+1}} f(t, x) \cdot w(t, x) \, dx \, dt \quad \forall w \in W_1^{k+1} \\
&u(t, 0) = u_{\text{in}}(t) \\
&u(0, x) = u_0(x)
\end{aligned} \tag{4.23}$$

is satisfied for each  $k \in \{1, \dots, R\}$ .

### 4.2.3 Spatial Discretization

For the discretization of  $u$  and  $f$ , we use standard finite elements in 1D with piecewise linear nodal basis  $\varphi_j$  satisfying

$$\varphi_j(x_k) = A_\emptyset \cdot \delta_{j,k}$$

so that the discretization of  $u$ ,  $u \approx \sum_j U_j \varphi_j$ , has coefficients  $U_j$  as energy per volume, thus proportional to temperature. For a single segment, this has no big advantage, but it will be useful later. Call this finite element space  $\hat{V}_1$ .

It will turn out that, at time  $t^k$ , we do not yet know  $f(t^{k+1}, \cdot)$ , so we assume  $f$  to be constant in time during  $[t^k, t^{k+1}]$ .

For the discretization  $\hat{W}_1$  of  $W_1$  it is now natural to use functions that have the same shape as the  $\varphi$  on  $\Gamma^{k+1}$ , but height 1. As they are required to be constant along the characteristics (4.12), we choose the roof-shaped functions of [8].

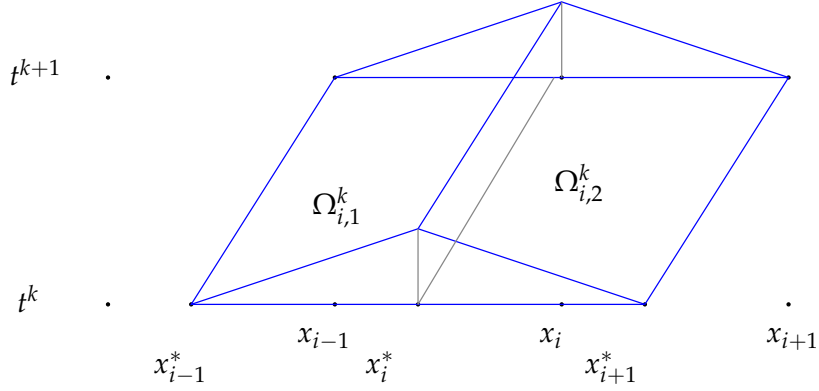


Figure 4.3: The ELLAM test function  $w_i^{k+1}$ , height 1.

Let  $x_i^* := x_i - v\tau$  and define the domains  $\Omega_{i,\{1,2\}}^k$  (parallelograms in space-time, convex hull of their vertices):

$$\begin{aligned}\Omega_{i,1}^k &:= \text{conv} \left( (k\tau, x_{i-1}^*); (k\tau, x_i^*); ((k+1)\tau, x_{i-1}); ((k+1)\tau, x_i) \right), \\ \Omega_{i,2}^k &:= \text{conv} \left( (k\tau, x_i^*); (k\tau, x_{i+1}^*); ((k+1)\tau, x_i); ((k+1)\tau, x_{i+1}) \right).\end{aligned}$$

Then

$$w_i^{k+1}(t, x) = \begin{cases} \frac{x-x_{i-1}}{h} + v \cdot \frac{t^{k+1}-t}{\tau} & (t, x) \in \Omega_{i,1}^k \\ \frac{x_{i+1}-x}{h} + v \cdot \frac{t^{k+1}-t}{\tau} & (t, x) \in \Omega_{i,2}^k \\ 0 & \text{else} \end{cases}$$

are the ELLAM test functions of [8].

The domains and the functions are shown in Figure 4.3.

In this definition, the superscript  $k+1$  indicates that we want to compute the  $(k+1)$ st time step. From now on, we consider a fixed time step only and drop this index to simplify notation.

An approximation of the RHS integral is

$$\int_0^\ell \int_{t^k}^{t^{k+1}} f(t, x) \cdot w(t, x) \approx \tau \cdot \frac{1}{2} \left( \int_0^\ell f(t^k, x) \cdot w(t^k, x) \, dx + \int_0^\ell f(t^{k+1}, x) \cdot w(t^{k+1}, x) \, dx \right). \quad (4.24)$$

We can now state the equations that form the discrete version of (4.23).

### Inflow Boundary

As in the continuous case, see equation (4.5), we do not specify Dirichlet boundary conditions but flow boundary conditions. The boundary sets used here are shown in Figure 4.4. This requires mapping the inflow to  $\Gamma_{\text{in}}$  and a different treatment of the integrals near the boundary.

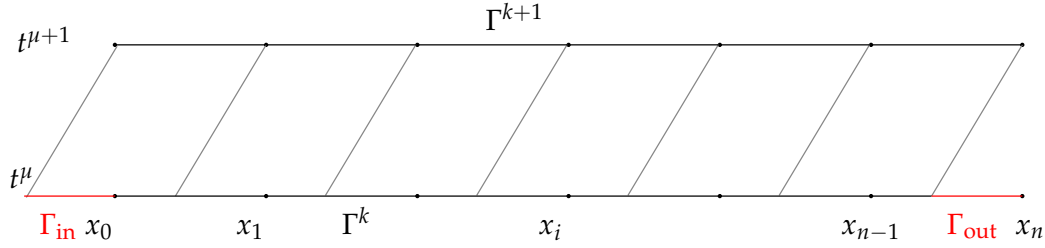


Figure 4.4: Boundary sets for a single ELLAM time step used here

The discretization of (4.23) can be written as

$$\begin{aligned}
 x_0 : \quad & U_0^{k+1} \int_{\Gamma^{k+1}} w_0 \varphi_0 + U_1^{k+1} \int_{\Gamma^{k+1}} w_0 \varphi_1 \\
 & = U_0^k \int_{\Gamma^k} w_0 \varphi_0 + U_1^k \int_{\Gamma^k} w_0 \varphi_1 + \int_{\Gamma_{\text{in}}} w_0 U_{\text{in}} \\
 & \quad + \frac{\tau}{2} \left( F_0^k \int_{\Gamma^{k+1}} w_0 \varphi_0 + F_1^k \int_{\Gamma^{k+1}} w_1 \varphi_1 \right) + \frac{\tau}{2} \left( F_0^k \int_{\Gamma^k} w_0 \varphi_0 + F_1^k \int_{\Gamma^k} w_0 \varphi_1 \right), \tag{4.25}
 \end{aligned}$$

$$\begin{aligned}
 x_1 : \quad & U_0^{k+1} \int_{\Gamma^{k+1}} w_1 \varphi_0 + U_1^{k+1} \int_{\Gamma^{k+1}} w_1 \varphi_1 + U_2^{k+1} \int_{\Gamma^{k+1}} w_1 \varphi_2 \\
 & = U_0^k \int_{\Gamma^k} w_1 \varphi_0 + U_1^k \int_{\Gamma^k} w_1 \varphi_1 + U_2^k \int_{\Gamma^k} w_1 \varphi_2 + \int_{\Gamma_{\text{in}}} w_1 U_{\text{in}}(x) \\
 & \quad + \frac{\tau}{2} \left( F_0^k \int_{\Gamma^{k+1}} w_1 \varphi_0 + F_1^k \int_{\Gamma^{k+1}} w_1 \varphi_1 + F_2^k \int_{\Gamma^{k+1}} w_1 \varphi_2 \right) \\
 & \quad + \frac{\tau}{2} \left( F_0^k \int_{\Gamma^k} w_1 \varphi_0 + F_1^k \int_{\Gamma^k} w_1 \varphi_1 + F_2^k \int_{\Gamma^k} w_1 \varphi_2 \right). \tag{4.26}
 \end{aligned}$$

### Interior Grid Points

At grid points sufficiently far from the boundary, boundary conditions do not have influence on our scheme.

For the test functions  $w_i, 2 \leq i \leq n-1$ , we do not get contributions of either  $\Gamma_l$  or  $\Gamma_r$ . Moreover, only the supports of certain  $w_i$  and  $\varphi_j$  overlap, this is shown in Figure 4.5.

So equation (4.23) in fully discrete form becomes

$$\begin{aligned}
 x_i : \quad & U_{i-1}^{k+1} \int_{\Gamma^{k+1}} w_i \varphi_{i-1} + U_i^{k+1} \int_{\Gamma^{k+1}} w_i \varphi_i + U_{i+1}^{k+1} \int_{\Gamma^{k+1}} w_i \varphi_{i+1} \\
 & = U_{i-2}^k \int_{\Gamma^k} w_i \varphi_{i-2} + U_{i-1}^k \int_{\Gamma^k} w_i \varphi_{i-1} + U_i^k \int_{\Gamma^k} w_i \varphi_i + U_{i+1}^k \int_{\Gamma^k} w_i \varphi_{i+1} \\
 & \quad + \frac{\tau}{2} \left( F_{i-1}^k \int_{\Gamma^{k+1}} w_i \varphi_{i-1} + F_i^k \int_{\Gamma^{k+1}} w_i \varphi_i + F_{i+1}^k \int_{\Gamma^{k+1}} w_i \varphi_{i+1} \right) \\
 & \quad + \frac{\tau}{2} \left( F_{i-2}^k \int_{\Gamma^k} w_i \varphi_{i-2} + F_{i-1}^k \int_{\Gamma^k} w_i \varphi_{i-1} + F_i^k \int_{\Gamma^k} w_i \varphi_i + F_{i+1}^k \int_{\Gamma^k} w_i \varphi_{i+1} \right). \tag{4.27}
 \end{aligned}$$

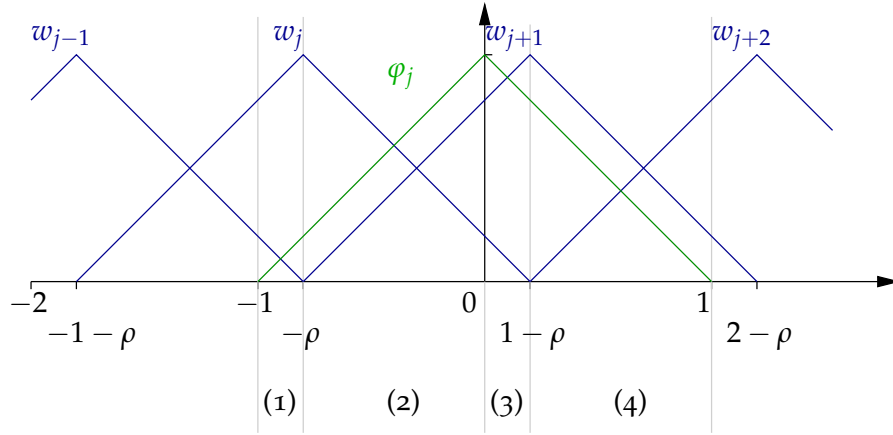


Figure 4.5: Sketch for the computation of  $\int w_i \varphi_j$  away from the boundary. Note that  $w_i$  (blue) always has height 1 whereas  $\varphi_j$  (green) has height  $A_\emptyset$  not necessarily equal to 1.

### Outflow Boundary

At the outflow boundary, only the last equation is affected:

$$\begin{aligned}
 x_n : \quad & U_{n-1}^{k+1} \int_{\Gamma^{k+1}} w_n \varphi_{n-1} + U_n^{k+1} \int_{\Gamma^{k+1}} w_n \varphi_n \\
 = \quad & U_{n-2}^k \int_{\Gamma^k} w_n \varphi_{n-2} + U_{n-1}^k \int_{\Gamma^k} w_n \varphi_{n-1} + U_n^k \int_{\Gamma^k} w_n \varphi_n \\
 & + \frac{\tau}{2} \left( F_{n-1}^k \int_{\Gamma^{k+1}} w_n \varphi_{n-1} + F_n^k \int_{\Gamma^{k+1}} w_n \varphi_n \right) \\
 & + \frac{\tau}{2} \left( F_{n-2}^k \int_{\Gamma^k} w_n \varphi_{n-2} + F_{n-1}^k \int_{\Gamma^k} w_n \varphi_{n-1} + F_n^k \int_{\Gamma^k} w_n \varphi_n \right).
 \end{aligned} \tag{4.28}$$

Note that  $\Gamma_{\text{out}} \not\subset \Gamma^k$ , so that no additional terms appear. We could explicitly compute the outflow by integration over  $\Gamma_{\text{out}}$ . For bifurcations, we will see that the flow from one segment to the next is treated implicitly, for terminal segments of the arterial tree, our model does not allow any outflow out of the leaf node. Only on the root segment of the venous tree, energy outflow out of our system might be interesting.

The outflow can be computed as

$$\begin{aligned}
 h \int_{-\rho}^0 U^k &= U_{n-2}^k h \int_{-\rho}^0 \varphi_{n-2} + U_{n-1}^k h \int_{-\rho}^0 \varphi_{n-1} \\
 &= U_{n-2}^k \cdot A_\emptyset h \cdot \left( \rho - \frac{1}{2} \rho^2 \right) + U_{n-1}^k \cdot A_\emptyset h \cdot \frac{1}{2} \rho^2.
 \end{aligned} \tag{4.29}$$

### 4.2.4 System of equations

From the structure of those equations, we can see that we get a system of equations of the form

$$M \cdot \bar{U}^{k+1} = M^e \cdot \bar{U}^k + \bar{B}^k \tag{4.30}$$

where the integrals over  $\Gamma^k$  and  $\Gamma^{k+1}$  lead to the entries of the two matrices  $M, M^e$  whereas the contributions of the boundary and the source terms can be put into the vector  $\bar{B}^k$ .

**Entries of  $M$** 

Due to the definition of  $w_i^{k+1}$ ,

$$w_i^{k+1}(t^{k+1}, x) = \frac{1}{A_{\emptyset}} \varphi_j(x), \text{ i. e. } w_i^{k+1}|_{\Gamma^{k+1}} = \frac{1}{A_{\emptyset}} \varphi_i|_{\Gamma^{k+1}}.$$

So  $M$  is a standard 1D finite element mass matrix, see Section 6.3, weighted with the cross section area  $A_{\emptyset}$ .

**Entries of  $M^e$** 

These values are slightly more complicated to evaluate.

As shown in Figure 4.5, the support of  $\varphi_j(x)$  has nontrivial intersection with the support of  $w_i^{k+1}(x, t^{k+1})$  if and only if  $i \in \{j-1, j, j+1, j+2\}$  and we need to integrate over piecewise quadratic functions.

The integrals over  $\Gamma^k$  can be evaluated analytically, here  $A$  is short for  $A_{\emptyset}$ :

$$\begin{aligned} I_{44}(A, h, \rho) &:= Ah \cdot \int_{1-\rho}^1 (1-x)(-1+\rho+x) dx &= Ah \cdot \left(\frac{1}{6}\rho^3\right) \\ I_{32}(A, h, \rho) &:= Ah \cdot \int_{-\rho}^0 (1+x)(\rho+x) dx &= Ah \cdot \left(-\frac{1}{6}\rho^3 + \frac{1}{2}\rho^2\right) \\ I_{33}(A, h, \rho) &:= Ah \cdot \int_0^{1-\rho} (1-x)(\rho+x) dx &= Ah \cdot \left(-\frac{1}{6}\rho^3 - \frac{1}{2}\rho^2 + \frac{1}{2}\rho + \frac{1}{6}\right) \\ I_{34}(A, h, \rho) &:= Ah \cdot \int_{1-\rho}^1 (1-x)(2-\rho-x) dx &= Ah \cdot \left(-\frac{1}{6}\rho^3 + \frac{1}{2}\rho^2\right) \\ I_{21}(A, h, \rho) &:= Ah \cdot \int_{-1}^{-\rho} (1+x)(1+\rho+x) dx &= Ah \cdot \left(\frac{1}{6}\rho^3 - \frac{1}{2}\rho + \frac{1}{3}\right) \\ I_{22}(A, h, \rho) &:= Ah \cdot \int_{-\rho}^0 (1+x)(1-\rho-x) dx &= Ah \cdot \left(\frac{1}{6}\rho^3 - \rho^2 + \rho\right) \\ I_{23}(A, h, \rho) &:= Ah \cdot \int_0^{1-\rho} (1-x)(1-\rho-x) dx &= Ah \cdot \left(\frac{1}{6}\rho^3 - \frac{1}{2}\rho + \frac{1}{3}\right) \\ I_{11}(A, h, \rho) &:= Ah \cdot \int_{-1}^{-\rho} (1+x)(-\rho-x) dx &= Ah \cdot \left(-\frac{1}{6}\rho^3 + \frac{1}{2}\rho^2 - \frac{1}{2}\rho + \frac{1}{6}\right). \end{aligned}$$

Now we can compute:

$$\int_{\Gamma^k} w_i \varphi_{i-2} = I_{44}(A, h, \rho) = Ah \cdot \left(\frac{\rho^3}{6}\right) \quad (4.31a)$$

$$\int_{\Gamma^k} w_i \varphi_{i-1} = I_{32}(A, h, \rho) + I_{33}(A, h, \rho) + I_{34}(A, h, \rho) = Ah \cdot \left(-\frac{\rho^3}{2} + \frac{\rho^2}{2} + \frac{\rho}{2} + \frac{1}{6}\right) \quad (4.31b)$$

$$\int_{\Gamma^k} w_i \varphi_i = I_{21}(A, h, \rho) + I_{22}(A, h, \rho) + I_{23}(A, h, \rho) = Ah \cdot \left(\frac{\rho^3}{2} - \rho^2 + \frac{2}{3}\right) \quad (4.31c)$$

$$\int_{\Gamma^k} w_i \varphi_{i+1} = I_{11}(A, h, \rho) = Ah \cdot \left(-\frac{\rho^3}{6} + \frac{\rho^2}{2} - \frac{\rho}{2} + \frac{1}{6}\right), \quad (4.31d)$$

special cases are:

$$\int_{\Gamma^k} w_0 \varphi_0 = I_{23}(A, h, \rho) = Ah \cdot \left( \frac{\rho^3}{6} - \frac{\rho}{2} + \frac{1}{3} \right) \quad (4.31e)$$

$$\int_{\Gamma^k} w_1 \varphi_0 = I_{33}(A, h, \rho) + I_{34}(A, h, \rho) = Ah \cdot \left( -\frac{\rho^3}{3} + \frac{\rho}{2} + \frac{1}{6} \right) \quad (4.31f)$$

$$\int_{\Gamma^k} w_n \varphi_{n-1} = I_{32}(A, h, \rho) + I_{33}(A, h, \rho) = Ah \cdot \left( -\frac{\rho^3}{3} + \frac{\rho}{2} + \frac{1}{3} \right) \quad (4.31g)$$

$$\int_{\Gamma^k} w_n \varphi_n = I_{21}(A, h, \rho) = Ah \cdot \left( \frac{\rho^3}{6} - \frac{\rho}{2} + \frac{1}{3} \right). \quad (4.31h)$$

Note that the matrix  $M^e$  is not symmetric, not even its sparsity structure is symmetric. Since we do not need to invert it, this is not going to cause much of a problem.

### Entries of $B^k$

As noted above, the vector  $B^k$  consists of boundary terms and source terms.

First consider the boundary terms: We need the discrete  $U_{\text{in}}(x)$  in equations (4.25) and (4.26).

Mapping continuous boundary data  $u_{\text{root}}(t)$  (energy content) to initial data  $u_{\text{in}}(x)$  is explained in equation (4.5). For the discretization, we need to consider energy densities: Let  $U_{\text{root}}(t)$  be the instantaneous inflow of energy density,  $U_{\text{root}}(k\tau) = R_{\text{in}}^k$ ,  $U_{\text{root}}((k+1)\tau) = R_{\text{in}}^{k+1}$ , then a linear approximation of  $U_{\text{root}}(t)$  on the time interval  $[k\tau, (k+1)\tau]$  can be written as

$$U_{\text{root}}(t) = R_{\text{in}}^k + \frac{t - k\tau}{\tau} (R_{\text{in}}^{k+1} - R_{\text{in}}^k).$$

Via equation (4.5), this can be mapped to initial data  $U_{\text{in}}(x)$  on  $[-\rho, 0]$ :

$$U_{\text{in}}(x) = R_{\text{in}}^{k+1} + \frac{x + \rho}{\rho} (R_{\text{in}}^k - R_{\text{in}}^{k+1}).$$

Note that inflowing energy density is proportional to inflowing temperature which will later be body temperature (temperature of inflowing blood).

Then we can compute

$$\begin{aligned} b_0^k &= \int_{\Gamma_{\text{in}}} U_{\text{in}} w_0 \, dx = Ah \int_{-\rho}^0 \left( R_{\text{in}}^{k+1} + \frac{x + \rho}{\rho} (R_{\text{in}}^k - R_{\text{in}}^{k+1}) \right) \cdot ((1 - \rho) - x) \, dx \\ &= Ah \left( \left( \frac{1}{2}\rho - \frac{1}{3}\rho^2 \right) R_{\text{in}}^k + \left( \frac{1}{2}\rho - \frac{1}{6}\rho^2 \right) R_{\text{in}}^{k+1} \right), \end{aligned} \quad (4.32)$$

$$\begin{aligned} b_1^k &= \int_{\Gamma_{\text{in}}} U_{\text{in}} w_1 \, dx = Ah \int_{-\rho}^0 \left( R_{\text{in}}^{k+1} + \frac{x + \rho}{\rho} (R_{\text{in}}^k - R_{\text{in}}^{k+1}) \right) \cdot (\rho + x) \, dx \\ &= Ah \left( \frac{1}{3}\rho^2 R_{\text{in}}^k + \frac{1}{6}\rho^2 R_{\text{in}}^{k+1} \right). \end{aligned} \quad (4.33)$$

The outflow is already incorporated in the  $M^e$  matrix by integrating only over  $\Gamma^k$  and not over  $\Gamma_{\text{out}}$ .



In the system,

$$\begin{aligned}
M \cdot \bar{U}^{k+1} &= M^e \cdot \bar{U}^k + \bar{b}^k + \frac{\tau}{2} \cdot (M\bar{F}_k + M^e\bar{F}_k) \\
\Rightarrow \bar{U}^{k+1} &= M^{-1} \left[ M^e \bar{U}^k + \bar{b}^k + \frac{\tau}{2} \cdot (M\bar{F}_k + M^e\bar{F}_k) \right] \\
\Rightarrow \bar{U}^{k+1} &= M^{-1} \left[ M^e \left( \bar{U}^k + \frac{\tau}{2} \bar{F}^k \right) + \bar{b}^k \right] + \frac{\tau}{2} \bar{F}^k.
\end{aligned} \tag{4.40}$$

$M$  is a tridiagonal matrix, so inverting it can be done efficiently by Gaußian elimination. However, as we will see in the next section, this only works in case of a single segment.  $M^e$  is the quadridiagonal (one upper, two lower diagonals) ELLAM matrix. Both these matrices correspond to the case that the segment has an unknown associated to both its initial and its terminal point.

### 4.3 ELLAM on Bifurcations

The coupling between the segments and the fact that one geometric point is part of three segments can be modeled in at least three different ways:

- Treat all segments separately and explicitly compute outflow / inflow:
  - For the arterial tree, compute the outflow from the parent segment, split it according to the flow splitting ratio and use this as inflow for the daughter segments.
  - For the venous tree, compute the outflows from the daughter segments, compute a weighted average according to the flow splitting ratios and use this as inflow for the parent segment.

This decouples the three segments, not allowing numerical artefacts to propagate in upflow direction. This sounds good at first, but makes our method inconsistent in the sense that splitting a segment in half by using a monofurcation (inserting intermediate node of multiplicity one such that one segment is split in parent and daughter) changes the properties of the numerical solution.

- Still assign three unknowns to what is geometrically one point and impose the limit conditions in (4.1) or (4.3) as two additional equations.

In this case, splitting one segment in half by using a monofurcation still changes the system of equations and might lead to the numerical solution being different.

- Assign only one unknown to the terminal point of the parent segment and no unknown to the initial node of the daughter segment<sup>2</sup>
  - For the arterial tree, the support of the  $(n_p - 1)$ st basis function of the parent segment lies partially within the daughter segments.
  - For the venous tree, the support of the 0th basis function of the parent segment lies partially within the daughter segments.

*Remark 4.3.1.* In the implementation in c++, vectors are always indexed from 0 to  $n - 1$ , so we need to be careful to use the correct correspondence between nodal values and the geometric location of the nodes depending on the type of segment being considered.

---

<sup>2</sup>Note that initial and terminal segment do not refer to the direction of flow

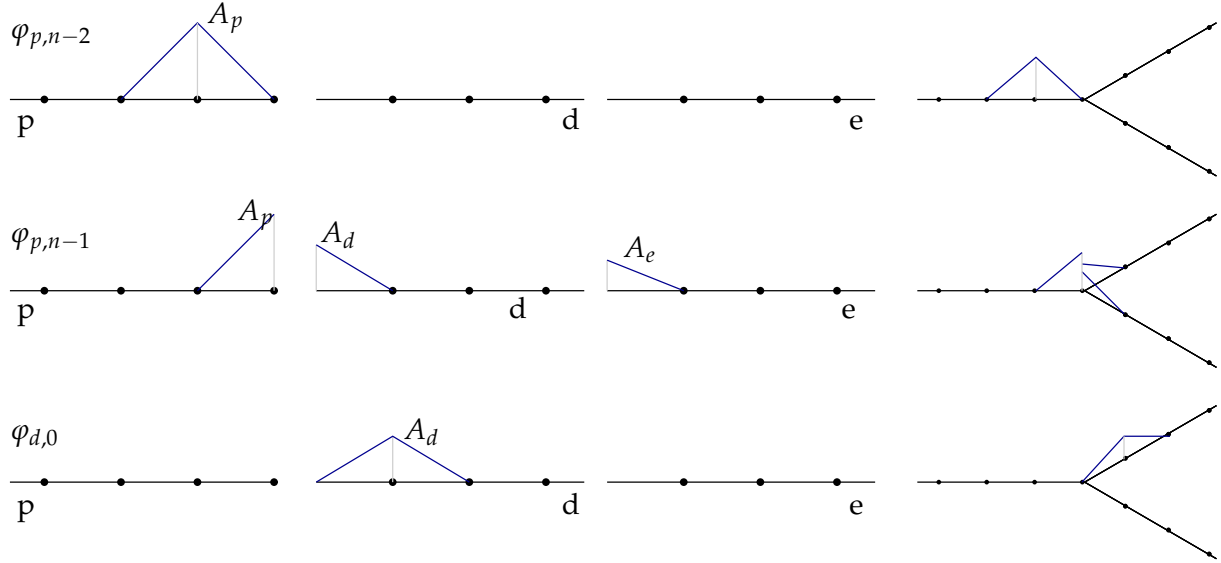


Figure 4.6: Basis functions  $\varphi_j$  of  $\hat{V}_a$ , the function space for discretization of energy content profiles on the arterial tree. This corresponds to a bifurcation ( $p \prec d, e$ ), the parent segment  $p$  is shown on the left, the two daughters  $d, e$  are shown in the center. On the right, we visualize the branching structure of these three segments.

We chose the last method because of the consistency reasons explained above. In this case, we need to modify our  $M$  and  $M^e$  matrices above: let  $M^-$  and  $M^{e,+}$  be the submatrix omitting the last row and column of  $M$  and  $M^e$ , respectively. This corresponds to segments with no unknown associated to their terminal point. Similarly, define  $M^+, M^{e,-}$  by omitting the first row and column for segments with no unknown associated to their initial point.

As for a single segment, we assume that each segment has at least four grid points assigned. This ensures that we do not need to treat left and right boundary within the same ELLAM equation. This assumption will be refined when we treat trees in Section 4.5.

### 4.3.1 An Arterial $\prec$ Bifurcation

We now need to explain what our basis functions for the discretization of  $V_a$  and  $W_a^{k+1}$ ,  $\hat{V}_a, \hat{W}_a^{k+1}$ , look like at a  $\prec$  bifurcation:

When considering a bifurcation, it becomes clear why our basis functions do not have unit height but  $A_\emptyset$ : we want to represent stationary (constant) temperature on all segments by vectors that have all the same entries. So the basis functions  $\varphi$  of  $\hat{V}_a$  are chosen as for a single segment but with the cross section area of the segment considered. This implies that  $\varphi$  are discontinuous at bifurcations, see Figure 4.6.

For the test functions  $w \in \hat{W}_a^{k+1}$ , mass conservation requires us to use a partition of unity. The flow into  $d$  and  $e$  is  $\theta_d$  and  $\theta_e$  times the flow out of  $p$ , so when tracing back along the characteristics across a bifurcation, the two components add up to 1.

The basis functions  $w_j(t^{k+1}, x)$  are shown in Figure 4.7,  $w_j(t^k, x)$  are shown in Figure 4.8.

We now look at the ELLAM equations associated with the points the bifurcation has influence on,  $x_{p,n-1}, x_{d,0}, x_{d,1}, x_{e,0}, x_{e,1}$ :

4 Advection in Vessel Trees

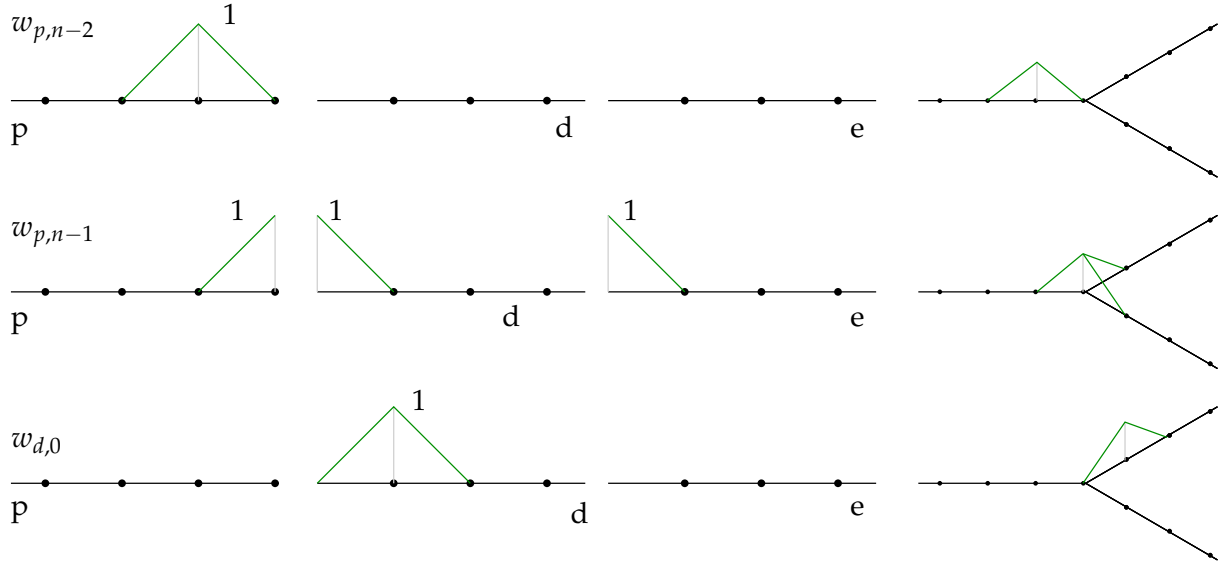


Figure 4.7: Basis functions  $w_j|_{\Gamma^{k+1}}$  of  $\hat{W}_a^{k+1}$ , the space of ELLAM test functions for advection in the arterial tree.

$$\begin{aligned}
 x_{p,n_p} &: U_{p,n-2}^{k+1} \int_{\Gamma^{k+1}} w_{p,n-1} \varphi_{p,n-2} + U_{p,n-1}^{k+1} \int_{\Gamma^{k+1}} \underbrace{w_{p,n-1} \varphi_{p,n-1}}_{*1} + U_{d,0}^{k+1} \int_{\Gamma^{k+1}} \underbrace{w_{p,n-1} \varphi_{d,0}}_{*2} + U_{e,0}^{k+1} \int_{\Gamma^{k+1}} \underbrace{w_{p,n-1} \varphi_{e,0}}_{*2} \\
 &= U_{p,n-3}^k \int_{\Gamma^k} w_{p,n-1} \varphi_{p,n-3} + U_{p,n-2}^k \int_{\Gamma^k} \underbrace{w_{p,n-1} \varphi_{p,n-2}}_{*4} + U_{p,n-1}^k \int_{\Gamma^k} \underbrace{w_{p,n-1} \varphi_{p,n-1}}_{*5} \\
 &\quad + U_{d,0}^k \int_{\Gamma^k} \underbrace{w_{p,n-1} \varphi_{d,0}}_{*6} + U_{e,0}^k \int_{\Gamma^k} \underbrace{w_{p,n-1} \varphi_{e,0}}_{*6} \\
 &\quad + \frac{\tau}{2} \left[ F_{p,n-2}^k \int_{\Gamma^{k+1}} w_{p,n-1} \varphi_{p,n-2} + F_{p,n-1}^k \int_{\Gamma^{k+1}} \underbrace{w_{p,n-1} \varphi_{p,n-1}}_{*1} \right. \\
 &\quad + F_{d,0}^k \int_{\Gamma^{k+1}} \underbrace{w_{p,n-1} \varphi_{d,0}}_{*2} + F_{e,0}^k \int_{\Gamma^{k+1}} \underbrace{w_{p,n-1} \varphi_{e,0}}_{*2} \\
 &\quad + F_{p,n-3}^k \int_{\Gamma^k} w_{p,n-1} \varphi_{p,n-3} + F_{p,n-2}^k \int_{\Gamma^k} \underbrace{w_{p,n-1} \varphi_{p,n-2}}_{*4} + F_{p,n-1}^k \int_{\Gamma^k} \underbrace{w_{p,n-1} \varphi_{p,n-1}}_{*5} \\
 &\quad \left. + F_{d,0}^k \int_{\Gamma^k} \underbrace{w_{p,n-1} \varphi_{d,0}}_{*6} + F_{e,0}^k \int_{\Gamma^k} \underbrace{w_{p,n-1} \varphi_{e,0}}_{*6} \right], \tag{4.41}
 \end{aligned}$$

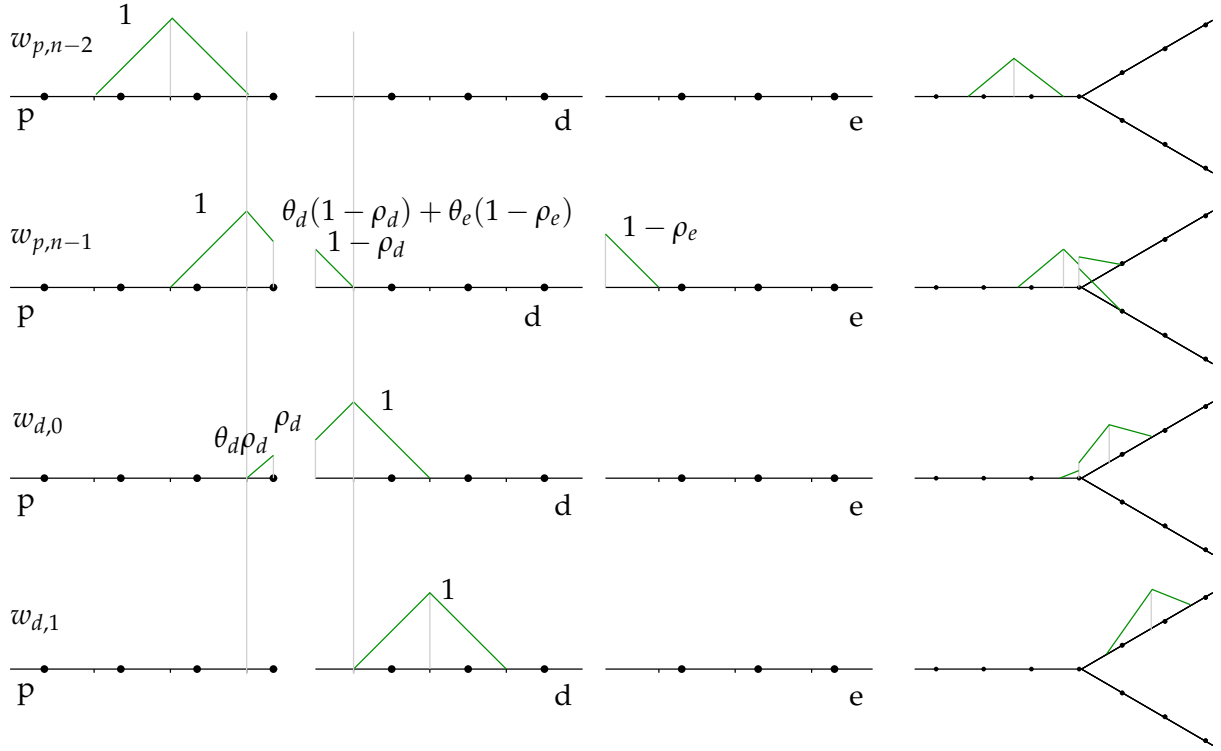


Figure 4.8: Basis functions  $w_j|_{\Gamma^k}$  of  $\hat{W}_a^{k+1}$ , the space of ELLAM test functions for advection in the arterial tree. Here, the flow velocities are such that  $\rho_p = 0.3, \rho_d = 0.5, \rho_e = 0.2$ .

$$\begin{aligned}
x_{d,0} &: U_{p,n-1}^{k+1} \int_{\Gamma^{k+1}} \underbrace{w_{d,0} \varphi_{p,n-1}}_{*3} + U_{d,0}^{k+1} \int_{\Gamma^{k+1}} w_{d,0} \varphi_{d,0} + U_{d,1}^{k+1} \int_{\Gamma^{k+1}} w_{d,0} \varphi_{d,1} \\
&= U_{p,n-2}^k \int_{\Gamma^k} \underbrace{w_{d,0} \varphi_{p,n-2}}_{*7} + U_{p,n-1}^k \int_{\Gamma^k} \underbrace{w_{d,0} \varphi_{p,n-1}}_{*8} + U_{d,0}^k \int_{\Gamma^k} w_{d,0} \varphi_{d,0} + U_{d,1}^k \int_{\Gamma^k} w_{d,0} \varphi_{d,1} \\
&\quad + \frac{\tau}{2} \left[ F_{p,n-1}^k \int_{\Gamma^{k+1}} \underbrace{w_{d,0} \varphi_{p,n-1}}_{*3} + F_{d,0}^k \int_{\Gamma^{k+1}} w_{d,0} \varphi_{d,0} + F_{d,1}^k \int_{\Gamma^{k+1}} w_{d,0} \varphi_{d,1} \right. \\
&\quad + U_{p,n-2}^k \int_{\Gamma^k} \underbrace{w_{d,0} \varphi_{p,n-2}}_{*7} + F_{p,n-1}^k \int_{\Gamma^k} \underbrace{w_{d,0} \varphi_{p,n-1}}_{*8} \\
&\quad \left. + F_{d,0}^k \int_{\Gamma^k} w_{d,0} \varphi_{d,0} + F_{d,1}^k \int_{\Gamma^k} w_{d,0} \varphi_{d,1} \right], \tag{4.42}
\end{aligned}$$

$$\begin{aligned}
x_{d,1} &: U_{d,0}^{k+1} \int_{\Gamma^{k+1}} w_{d,1} \varphi_{d,0} + U_{d,1}^{k+1} \int_{\Gamma^{k+1}} w_{d,1} \varphi_{d,1} + U_{d,2}^{k+1} \int_{\Gamma^{k+1}} w_{d,1} \varphi_{d,2} \\
&= U_{p,n-1}^k \int_{\Gamma^k} \underbrace{w_{d,1} \varphi_{p,n-1}}_{*9} + U_{d,0}^k \int_{\Gamma^k} w_{d,1} \varphi_{d,0} + U_{d,1}^k \int_{\Gamma^k} w_{d,1} \varphi_{d,1} + U_{d,2}^k \int_{\Gamma^k} w_{d,1} \varphi_{d,2} \\
&\quad + \frac{\tau}{2} \left[ F_{d,0}^k \int_{\Gamma^{k+1}} w_{d,1} \varphi_{d,0} + F_{d,1}^k \int_{\Gamma^{k+1}} w_{d,1} \varphi_{d,1} + F_{d,2}^k \int_{\Gamma^{k+1}} w_{d,1} \varphi_{d,2} \right. \\
&\quad \left. + F_{p,n-1}^k \int_{\Gamma^k} \underbrace{w_{d,1} \varphi_{p,n-1}}_{*9} + F_{d,0}^k \int_{\Gamma^k} w_{d,1} \varphi_{d,0} + F_{d,1}^k \int_{\Gamma^k} w_{d,1} \varphi_{d,1} + F_{d,2}^k \int_{\Gamma^k} w_{d,1} \varphi_{d,2} \right]. \tag{4.43}
\end{aligned}$$

All terms that are not computed in the standard way are marked. The equations for  $x_{e,0}, x_{e,1}$  have the same structure as those for  $x_{d,0}, x_{d,1}$

The colored \*s used here include the integration over  $\Gamma^k$  or  $\Gamma^{k+1}$ . They are for easier recognition of the various terms, the colors do not have any meaning.

We define four more terms for specific parts of the integrals above:

$$\begin{aligned}
J_{34}(A_p, h_p, \rho_p, \rho_d) &= A_p h_p \cdot \int_{-\rho_p}^0 -x \left( (1 - \rho_d) - \frac{\rho_d}{\rho_p} x \right) dx \\
&= A_p h_p \cdot \left( \frac{1}{2} \rho_p^2 - \frac{1}{6} \rho_d \rho_p^2 \right) \\
J_{22}(A_p, h_p, \rho_p, \rho_d) &= A_p h_p \cdot \int_{-\rho_p}^0 (1 + x) \left( (1 - \rho_d) - \frac{\rho_d}{\rho_p} x \right) dx \\
&= A_p h_p \cdot \left( \rho_p - \frac{1}{2} \rho_p^2 - \frac{1}{2} \rho_d \rho_p + \frac{1}{6} \rho_d \rho_p^2 \right) \\
J_{44}(A_p, h_p, \rho_p, \rho_d) &= \frac{\rho_d}{\rho_p} \cdot I_{44}(A_p, h_p, \rho_p) \\
J_{32}(A_p, h_p, \rho_p, \rho_d) &= \frac{\rho_d}{\rho_p} \cdot I_{32}(A_p, h_p, \rho_p)
\end{aligned}$$

Note that this is consistent with equivalent speeds relative to the grids:

For  $A_p = A_d, h_p = h_d, \rho_p = \rho_d$ ,

$$\begin{aligned}
J_{34}(A_p, h_p, \rho_p, \rho_d) &= I_{34}(A_p, h_p, \rho_p) = I_{34}(A_d, h_d, \rho_d) \\
J_{22}(A_p, h_p, \rho_p, \rho_d) &= I_{22}(A_p, h_p, \rho_p) = I_{22}(A_d, h_d, \rho_d) \\
J_{44}(A_p, h_p, \rho_p, \rho_d) &= I_{44}(A_p, h_p, \rho_p) = I_{44}(A_d, h_d, \rho_d) \\
J_{32}(A_p, h_p, \rho_p, \rho_d) &= I_{32}(A_p, h_p, \rho_p) = I_{32}(A_d, h_d, \rho_d).
\end{aligned}$$

Now we can compute:

$$\begin{aligned}
*1 \quad & \int_{\Gamma^{k+1}} w_{p,n-1} \varphi_{p,n-1} \\
& = A_p h_p \int_0^1 x \cdot x \, dx + A_d h_d \int_0^1 x \cdot x \, dx + A_e h_e \int_0^1 x \cdot x \, dx = A_p h_p \cdot \frac{1}{3} + A_d h_d \cdot \frac{1}{3} + A_e h_e \cdot \frac{1}{3} \\
*2 \quad & \int_{\Gamma^{k+1}} w_{p,n-1} \varphi_{d,0} \\
& = A_d h_d \int_0^1 (1-x) \cdot x \, dx = A_d h_d \cdot \frac{1}{6} \\
*3 \quad & \int_{\Gamma^{k+1}} w_{d,0} \varphi_{p,n-1} \\
& = A_d h_d \int_0^1 (1-x) \cdot x \, dx = A_d h_d \cdot \frac{1}{6} \\
*4 \quad & \int_{\Gamma^k} w_{p,n-1} \varphi_{p,n-2} \\
& = I_{32}(A_p, h_p, \rho_p) + I_{33}(A_p, h_p, \rho_p) + \theta_d J_{34}(A_p, h_p, \rho_p, \rho_d) + \theta_e J_{34}(A_p, h_p, \rho_p, \rho_e) \\
*5 \quad & \int_{\Gamma^k} w_{p,n-1} \varphi_{p,n-1} \\
& = I_{21}(h_p, \rho_p) + \theta_d J_{22}(A_p, h_p, \rho_p, \rho_d) + \theta_e J_{22}(A_p, h_p, \rho_p, \rho_e) + I_{23}(A_d, h_d, \rho_d) + I_{23}(A_e, h_e, \rho_e) \\
*6 \quad & \int_{\Gamma^k} w_{p,n-1} \varphi_{d,0} \\
& = I_{11}(A_d, h_d, \rho_d) \\
*7 \quad & \int_{\Gamma^k} w_{d,0} \varphi_{p,n-2} \\
& = \theta_d J_{44}(A_p, h_p, \rho_p, \rho_d) \\
*8 \quad & \int_{\Gamma^k} w_{d,0} \varphi_{p,n-1} \\
& = \theta_d J_{32}(A_p, h_p, \rho_p, \rho_d) + I_{33}(A_d, h_d, \rho_d) + I_{34}(A_d, h_d, \rho_d) \\
*9 \quad & \int_{\Gamma^k} w_{d,1} \varphi_{p,n-1} \\
& = I_{44}(A_d, h_d, \rho_d)
\end{aligned}$$

The whole three-segment problem can be put in a single system of equations of the following block structure:

$$M_{\text{BLOCK}}^{\leftarrow} \cdot \bar{U}_{\text{MULTI}}^{k+1} = M_{\text{BLOCK}}^{e,\leftarrow} \cdot \bar{U}_{\text{MULTI}}^k + \bar{B}_{\text{MULTI}}^k$$

where

$$\bar{B}_{\text{MULTI}}^k = \begin{bmatrix} \frac{\bar{B}_p^k}{\bar{B}_d^k} \\ \frac{\bar{B}_d^k}{\bar{B}_e^k} \end{bmatrix} = \begin{bmatrix} \frac{\bar{b}_p^k}{0} \\ 0 \end{bmatrix} + \frac{\tau}{2} \left( M_{\text{BLOCK}}^{\leftarrow} \cdot \bar{F}_{\text{MULTI}}^k + M_{\text{BLOCK}}^{e,\leftarrow} \cdot \bar{F}_{\text{MULTI}}^k \right).$$

Here,

$$\bar{F}_{\text{MULTI}}^k = \begin{bmatrix} \frac{\bar{F}_p^k}{\bar{F}_d^k} \\ \bar{F}_e^k \end{bmatrix}$$

and  $\bar{F}$  are the vectors of coefficients when discretizing  $f(t, x)|_{t \in [k\tau, (k+1)\tau]} = f(x)$  with respect to the appropriate basis functions:

$$\begin{aligned} f|_p &\approx \sum_i (\bar{F}_p^k)_i \cdot \varphi_{p;i} \\ f|_d &\approx \sum_i (\bar{F}_d^k)_i \cdot \varphi_{d;i} \\ f|_e &\approx \sum_i (\bar{F}_e^k)_i \cdot \varphi_{e;i}. \end{aligned}$$

The overall structure is

$$\begin{aligned} &\left[ \begin{array}{c|c|c} M_p + C_{p,d}^< + C_{p,e}^< & C_{p,d}^<,u & C_{p,e}^<,u \\ \hline C_{p,d}^<,l & M_{d1}^- & 0 \\ \hline C_{p,d}^<,l & 0 & M_{d2}^- \end{array} \right] \cdot \left[ \begin{array}{c} \bar{U}_p^{k+1} \\ \bar{U}_{d1}^{k+1} \\ \bar{U}_{d2}^{k+1} \end{array} \right] \\ &= \left[ \begin{array}{c|c|c} M_p^e + C_{p,d}^{e,<} + C_{p,e}^{e,<} & C_{p,d}^{e,<,u} & C_{p,e}^{e,<,u} \\ \hline C_{p,d}^{e,<,l} & M_{d1}^{-,e} & 0 \\ \hline C_{p,d}^{e,<,l} & 0 & M_{d2}^{-,e} \end{array} \right] \cdot \left[ \begin{array}{c} \bar{U}_p^k \\ \bar{U}_{d1}^k \\ \bar{U}_{d2}^k \end{array} \right] + \left[ \begin{array}{c} \bar{B}_p^k \\ \bar{B}_d^k \\ \bar{B}_e^k \end{array} \right] \end{aligned}$$

with

$$\begin{aligned} C_{p,d}^< &= \left[ \begin{array}{c} \ominus \\ A_d h_d \cdot \frac{1}{3} \end{array} \right] \\ C_{p,d}^<,u &= \left[ \begin{array}{c} \ominus \\ A_d h_d \cdot \frac{1}{6} \end{array} \right] \\ C_{p,d}^<,l &= \left[ \begin{array}{c} A_d h_d \cdot \frac{1}{6} \\ \ominus \end{array} \right] \\ C_{p,d}^{e,<} &= \left[ \begin{array}{c} \ominus \\ \sum_{\delta \in \{d,e\}} \theta_\delta J_{34}(A_p, h_p, \rho_p, \rho_\delta) \quad \sum_{\delta \in \{d,e\}} \theta_\delta J_{22}(A_p, h_p, \rho_p, \rho_\delta) + I_{23}(A_\delta, h_\delta, \rho_\delta) \end{array} \right] \\ C_{p,d}^{e,<,u} &= \left[ \begin{array}{c} \ominus \\ I_{11}(A_d, h_d, \rho_d) \end{array} \right] \\ C_{p,d}^{e,<,l} &= \left[ \begin{array}{c} \theta_d J_{44}(A_p, h_p, \rho_p, \rho_d) \quad \theta_d J_{32}(A_p, h_p, \rho_p, \rho_d) + I_{33}(A_d, h_d, \rho_d) + I_{34}(A_d, h_d, \rho_d) \\ \ominus \quad I_{44}(A_d, h_d, \rho_d) \end{array} \right] \end{aligned}$$

where  $\ominus$  denotes that the rest of the matrix has zero entries.





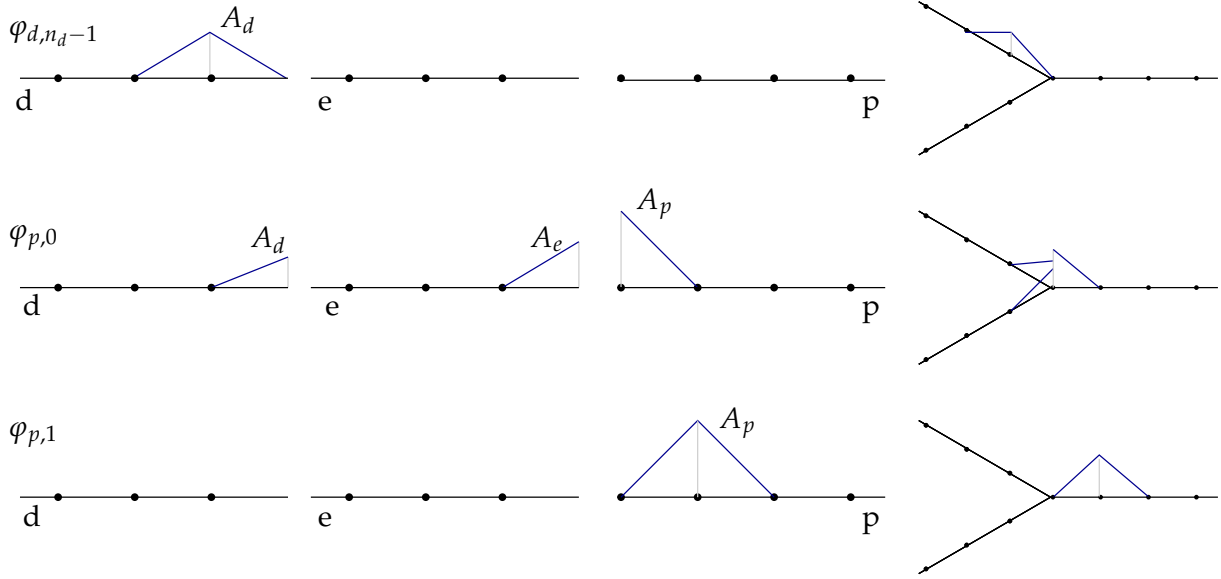


Figure 4.9: Basis functions  $\varphi_j$  of  $\hat{V}_v$ , the function space for discretization of energy content profiles on the venous tree. The two daughter segments  $d, e$  of a bifurcation ( $d, e > p$ ) are shown on the left, the parent segment is shown in the center, the direction of flow is to the right. On the very right, we visualize the branching structure of the segments.

### 4.3.2 A Venous $\succ$ Bifurcation

Here, we need to explain what our basis functions for the discretization of  $V_v$  and  $W_v^{k+1}$ ,  $\hat{V}_v$  and  $\hat{W}_v^{k+1}$  look like at a  $\succ$  bifurcation ( $d, e > p$ ).

Again, the base functions  $\varphi$  are chosen in such a way that the  $\mathbf{1}$ -vector represents the stationary profile (constant temperature on all three segments), so they are discontinuous at a bifurcation, see Figure 4.9.

For the test functions  $w \in \hat{W}_v^{k+1}$ , due to mass conservation we again use a partition of unity. Now tracing back the characteristics across the bifurcation yields two components of  $\mathbf{1}$  each as weighting occurs in the forward direction only.

The test functions  $w_j(t^{k+1}, x)$  are shown in Figure 4.10,  $w_j(t^k, x)$  are shown in Figure 4.11.

Here, the bifurcation has influences on the ELLAM equations for the unknowns  $x_{d,n_d-1}$ ,  $x_{e,n_e-1}$ ,  $x_{p,0}$ , and  $x_{p,1}$ :

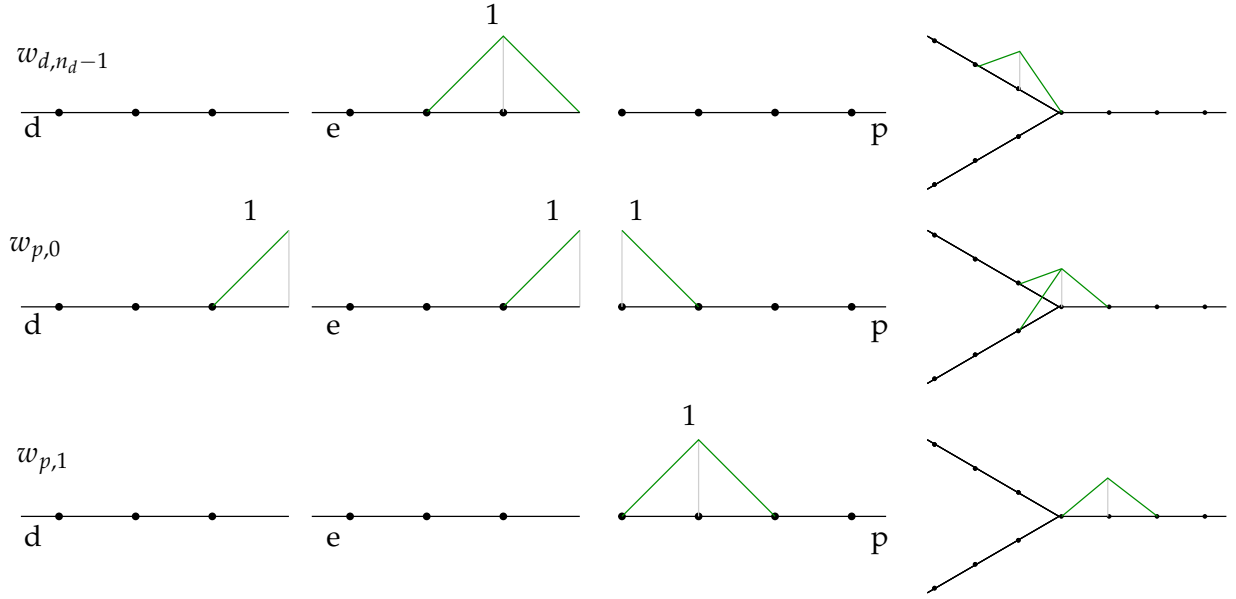


Figure 4.10: Basis functions  $w_j|_{\Gamma^{k+1}}$  of  $\hat{W}_v^{k+1}$ , the space of ELLAM test functions for advection in the venous tree.

$$\begin{aligned}
 x_{d,n_d-1} : & \quad U_{d,n_d-2}^{k+1} \int_{\Gamma^{k+1}} w_{d,n_d-1} \varphi_{d,n_d-2} + U_{d,n_d-1}^{k+1} \int_{\Gamma^{k+1}} w_{d,n_d-1} \varphi_{d,n_d-1} + U_{p,0}^{k+1} \int_{\Gamma^{k+1}} \underbrace{w_{d,n_d-1} \varphi_{p,0}}_{*3} \\
 = & \quad U_{d,n_d-3}^k \int_{\Gamma^k} w_{d,n_d-1} \varphi_{d,n_d-3} + U_{d,n_d-2}^k \int_{\Gamma^k} w_{d,n_d-1} \varphi_{d,n_d-2} \\
 & + U_{d,n_d-1}^k \int_{\Gamma^k} w_{d,n_d-1} \varphi_{d,n_d-1} + U_{p,0}^k \int_{\Gamma^k} \underbrace{w_{d,n_d-1} \varphi_{p,0}}_{*9} \tag{4.44} \\
 & + \frac{\tau}{2} \left[ F_{d,n_d-2}^k \int_{\Gamma^{k+1}} w_{d,n_d-1} \varphi_{d,n_d-2} + F_{d,n_d-1}^k \int_{\Gamma^{k+1}} \underbrace{w_{d,n_d-1} \varphi_{p,0}}_{*3} + F_{p,0}^k \int_{\Gamma^{k+1}} w_{d,n_d-1} \varphi_{p,0} \right. \\
 & + F_{d,n_d-3}^k \int_{\Gamma^k} w_{d,n_d-1} \varphi_{d,n_d-3} + F_{d,n_d-2}^k \int_{\Gamma^k} w_{d,n_d-1} \varphi_{d,n_d-2} \\
 & \left. + F_{d,n_d-1}^k \int_{\Gamma^k} w_{d,n_d-1} \varphi_{d,n_d-1} + F_{p,0}^k \int_{\Gamma^k} \underbrace{w_{d,n_d-1} \varphi_{p,0}}_{*9} \right],
 \end{aligned}$$

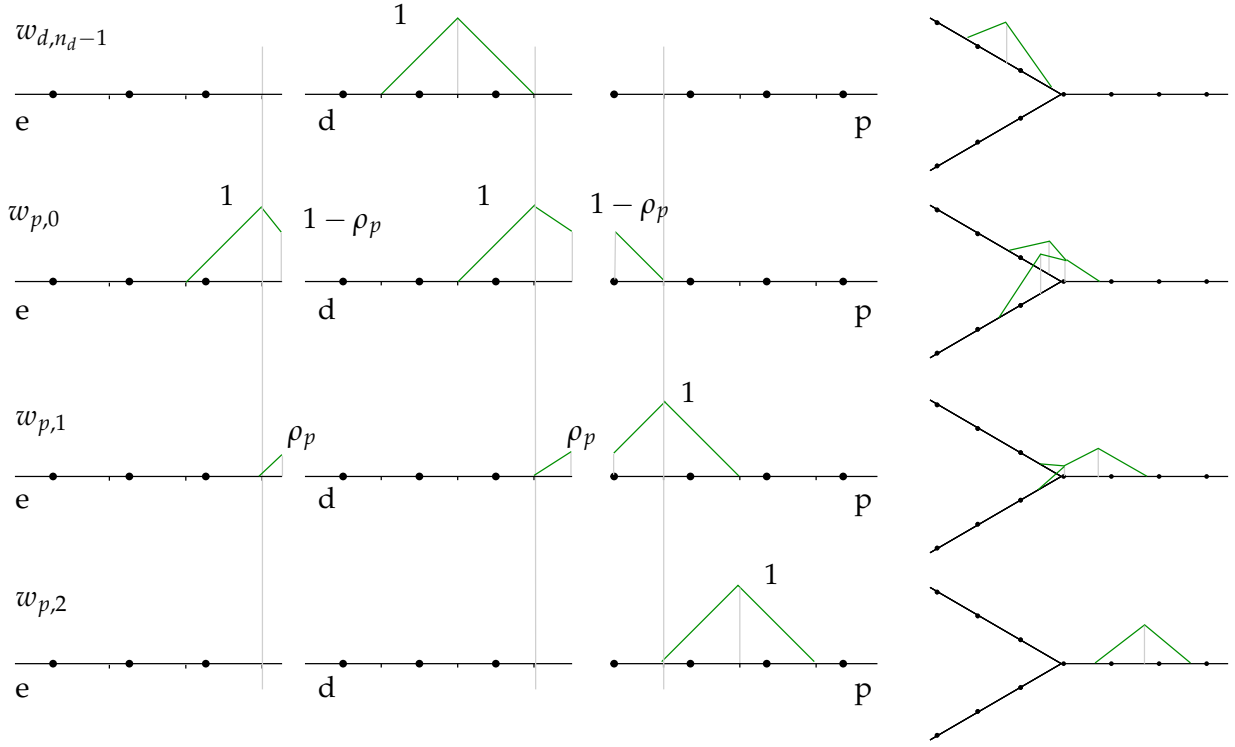


Figure 4.11: Basis functions  $w_j|_{\Gamma^k}$  of  $\hat{W}_v^{k+1}$ , the space of ELLAM test functions for advection in the venous tree. Here, the flow velocities are such that  $\rho_d = 0.2, \rho_e = 0.5, \rho_p = 0.3$ .

$$\begin{aligned}
x_{p,0} : & \quad U_{d,n_d-1}^{k+1} \int_{\Gamma^{k+1}} \underbrace{w_{p,0} \varphi_{d,n_d-1}}_{*2} + U_{e,n_e-1}^{k+1} \int_{\Gamma^{k+1}} \underbrace{w_{p,0} \varphi_{e,n_e-1}}_{*2} + U_{p,0}^{k+1} \int_{\Gamma^{k+1}} \underbrace{w_{p,0} \varphi_{p,0}}_{*1} + U_{p,1}^{k+1} \int_{\Gamma^{k+1}} w_{p,0} \varphi_{p,1} \\
= & \quad U_{d,n_d-2}^k \int_{\Gamma^k} \underbrace{w_{p,0} \varphi_{d,n_d-2}}_{*6} + U_{e,n_e-2}^k \int_{\Gamma^k} \underbrace{w_{p,0} \varphi_{e,n_e-2}}_{*6} + U_{d,n_d-1}^k \int_{\Gamma^k} \underbrace{w_{p,0} \varphi_{d,n_d-1}}_{*4} + U_{e,n_e-1}^k \int_{\Gamma^k} \underbrace{w_{p,0} \varphi_{e,n_e-1}}_{*4} \\
& + U_{p,0}^k \int_{\Gamma^k} \underbrace{w_{p,0} \varphi_{p,0}}_{*5} + U_{p,1}^k \int_{\Gamma^k} w_{p,0} \varphi_{p,1} \tag{4.45} \\
& + \frac{\tau}{2} \left[ F_{d,n_d-1}^k \int_{\Gamma^{k+1}} \underbrace{w_{p,0} \varphi_{d,n_d-1}}_{*2} + F_{e,n_e-1}^k \int_{\Gamma^{k+1}} \underbrace{w_{p,0} \varphi_{e,n_e-1}}_{*2} + F_{p,0}^k \int_{\Gamma^{k+1}} \underbrace{w_{p,0} \varphi_{p,0}}_{*1} + F_{p,1}^k \int_{\Gamma^{k+1}} w_{p,0} \varphi_{p,1} \right. \\
& + F_{d,n_d-2}^k \int_{\Gamma^k} \underbrace{w_{p,0} \varphi_{d,n_d-2}}_{*6} + F_{e,n_e-2}^k \int_{\Gamma^k} \underbrace{w_{p,0} \varphi_{e,n_e-2}}_{*6} + F_{d,n_d-1}^k \int_{\Gamma^k} \underbrace{w_{p,0} \varphi_{d,n_d-1}}_{*4} + F_{e,n_e-1}^k \int_{\Gamma^k} \underbrace{w_{p,0} \varphi_{e,n_e-1}}_{*4} \\
& \left. + F_{p,0}^k \int_{\Gamma^k} \underbrace{w_{p,0} \varphi_{p,0}}_{*5} + F_{p,1}^k \int_{\Gamma^k} w_{p,0} \varphi_{p,1} \right],
\end{aligned}$$

$$\begin{aligned}
x_{p,1} : & \quad U_{p,0}^{k+1} \int_{\Gamma^{k+1}} w_{p,1} \varphi_{p,0} + U_{p,1}^{k+1} \int_{\Gamma^{k+1}} w_{p,1} \varphi_{p,1} + U_{p,2}^{k+1} \int_{\Gamma^{k+1}} w_{p,1} \varphi_{p,2} \\
& = U_{d,n_d-1}^k \int_{\Gamma^k} \underbrace{w_{p,1} \varphi_{d,n_d-1}}_{*7} + U_{e,n_e-1}^k \int_{\Gamma^k} \underbrace{w_{p,1} \varphi_{e,n_e-1}}_{*7} + U_{p,0}^k \int_{\Gamma^k} \underbrace{w_{p,1} \varphi_{p,0}}_{*8} \\
& \quad + U_{p,1}^k \int_{\Gamma^k} w_{p,1} \varphi_{p,1} + U_{p,2}^k \int_{\Gamma^k} w_{p,1} \varphi_{p,2} \\
& \quad + \frac{\tau}{2} \left[ F_{p,0}^k \int_{\Gamma^k} w_{p,1} \varphi_{p,0} + F_{p,1}^k \int_{\Gamma^k} w_{p,1} \varphi_{p,1} + F_{p,2}^k \int_{\Gamma^k} w_{p,1} \varphi_{p,2} \right. \\
& \quad + F_{d,n_d-1}^k \int_{\Gamma^k} \underbrace{w_{p,1} \varphi_{d,n_d-1}}_{*7} + F_{e,n_e-1}^k \int_{\Gamma^k} \underbrace{w_{p,1} \varphi_{e,n_e-1}}_{*7} + F_{p,0}^k \int_{\Gamma^k} \underbrace{w_{p,1} \varphi_{p,0}}_{*8} \\
& \quad \left. + F_{p,1}^k \int_{\Gamma^k} w_{p,1} \varphi_{p,1} + F_{p,2}^k \int_{\Gamma^k} w_{p,1} \varphi_{p,2} \right].
\end{aligned} \tag{4.46}$$

The equation for  $x_{e,n_e-1}$  has the same structure as the one for  $x_{d,n_d-1}$ . The nonstandard integrals are marked and can be computed as follows:

$$\begin{aligned}
*1 & \quad \int_{\Gamma^{k+1}} w_{p,0} \varphi_{p,0} \\
& = A_p h_p \int_0^1 x \cdot x \, dx + A_d h_d \int_0^1 x \cdot x \, dx + A_e h_e \int_0^1 x \cdot x \, dx = A_p h_p \cdot \frac{1}{3} + A_d h_d \cdot \frac{1}{3} + A_e h_e \cdot \frac{1}{3} \\
*2 & \quad \int_{\Gamma^{k+1}} w_{p,0} \varphi_{d,n_d-1} \\
& = A_d h_d \int_0^1 x \cdot (1-x) \, dx = A_d h_d \cdot \frac{1}{6} \\
*3 & \quad \int_{\Gamma^{k+1}} w_{d,n_d-1} \varphi_{p,0} \\
& = A_d h_d \int_0^1 (1-x) \cdot x \, dx = A_d h_d \cdot \frac{1}{6} \\
*9 & \quad \int_{\Gamma^k} w_{d,n_d-1} \varphi_{p,0} \\
& = I_{11}(A_d, h_d, \rho_d) \\
*6 & \quad \int_{\Gamma^k} w_{p,0} \varphi_{d,n_d-2} \\
& = I_{44}(A_d, h_d, \rho_d) \\
*4 & \quad \int_{\Gamma^k} w_{p,0} \varphi_{d,n_d-1} \\
& = I_{32}(A_d, h_d, \rho_d) + I_{33}(A_d, h_d, \rho_d) + J_{34}(A_d, h_d, \rho_d, \rho_p) \\
*5 & \quad \int_{\Gamma^k} w_{p,0} \varphi_{p,0} \\
& = I_{21}(A_d, h_d, \rho_d) + I_{21}(A_e, h_e, \rho_e) + J_{22}(A_d, h_d, \rho_d, \rho_p) + J_{22}(A_e, h_e, \rho_e, \rho_p) + I_{23}(A_p, h_p, \rho_p)
\end{aligned}$$

$$\begin{aligned}
 *7 \quad & \int_{\Gamma^k} w_{p,1} \varphi_{d,n_d-1} \\
 & = J_{44}(A_d, h_d, \rho_d, \rho_p) \\
 *8 \quad & \int_{\Gamma^k} w_{p,1} \varphi_{p,0} \\
 & = J_{32}(A_d, h_d, \rho_d, \rho_p) + J_{32}(A_e, h_e, \rho_e, \rho_p) + I_{33}(A_p, h_p, \rho_p) + I_{34}(A_p, h_p, \rho_p)
 \end{aligned}$$

Again, we can put the three-segment problem into one block system:

$$M_{\text{BLOCK}}^{\succ} \cdot \bar{U}_{\text{MULTI}}^{k+1} = M_{\text{BLOCK}}^{e,\succ} \cdot \bar{U}_{\text{MULTI}}^k + B_{\text{MULTI}}^k$$

where

$$\bar{B}_{\text{MULTI}}^k = \begin{bmatrix} \frac{\bar{B}_p^k}{\bar{B}_d^k} \\ \frac{\bar{B}_d^k}{\bar{B}_e^k} \end{bmatrix} = \begin{bmatrix} 0 \\ \frac{\bar{b}_d^k}{\bar{b}_e^k} \end{bmatrix} + \frac{\tau}{2} \left( M_{\text{BLOCK}}^{\succ} \cdot \bar{F}_{\text{MULTI}}^k + M_{\text{BLOCK}}^{e,\succ} \cdot \bar{F}_{\text{MULTI}}^k \right)$$

and  $\bar{F}_{\text{MULTI}}^k$  is given in the same way as for  $\prec$  bifurcations.

The overall structure is

$$\begin{bmatrix} M_p + C_p^{\succ} & C_{p,d}^{\succ,u} & C_{p,e}^{\succ,u} \\ C_{p,d}^{\succ,l} & M_d^+ & 0 \\ C_{p,e}^{\succ,l} & 0 & M_e^+ \end{bmatrix} \cdot \begin{bmatrix} \bar{U}_p^{k+1} \\ \bar{U}_d^{k+1} \\ \bar{U}_e^{k+1} \end{bmatrix} = \begin{bmatrix} M_p^e + C_p^{e,\succ} & C_{p,d}^{e,\succ,u} & C_{p,e}^{e,\succ,u} \\ C_{p,d}^{e,\succ,l} & M_d^{+,e} & 0 \\ C_{p,e}^{e,\succ,l} & 0 & M_e^{+,e} \end{bmatrix} \cdot \begin{bmatrix} \bar{U}_p^k \\ \bar{U}_d^k \\ \bar{U}_e^k \end{bmatrix} + \begin{bmatrix} \frac{B_p^k}{\bar{B}_d^k} \\ \frac{B_d^k}{\bar{B}_e^k} \end{bmatrix}$$

with

$$\begin{aligned}
 C_p^{\succ} &= \begin{bmatrix} A_d h_d \cdot \frac{1}{3} + A_e h_e \cdot \frac{1}{3} \\ \ominus \end{bmatrix} \\
 C_{d,p}^{\succ,u} &= \begin{bmatrix} A_d h_d \cdot \frac{1}{6} \\ \ominus \end{bmatrix} \\
 C_{d,p}^{\succ,l} &= \begin{bmatrix} \ominus \\ A_d h_d \cdot \frac{1}{6} \end{bmatrix} \\
 C_p^{e,\succ} &= \begin{bmatrix} \sum_{\delta \in \{d,e\}} I_{21}(A_\delta, h_\delta, \rho_\delta) + J_{22}(A_\delta, h_\delta, \rho_\delta, \rho_p) \\ \sum_{\delta \in \{d,e\}} J_{32}(A_\delta, h_\delta, \rho_\delta, \rho_p) \\ \ominus \end{bmatrix} \\
 C_{d,p}^{e,\succ,u} &= \begin{bmatrix} I_{44}(A_d, h_d, \rho_d) & I_{32}(A_d, h_d, \rho_d) + I_{33}(A_d, h_d, \rho_d) + J_{34}(A_d, h_d, \rho_d, \rho_p) \\ \ominus & J_{44}(A_d, h_d, \rho_d, \rho_p) \end{bmatrix} \\
 C_{d,p}^{\succ,l} &= \begin{bmatrix} \ominus \\ I_{11}(A_d, h_d, \rho_d) \end{bmatrix}.
 \end{aligned}$$

The following block structure shows where the coupling terms are added:

$$\begin{array}{l}
 M_{\text{BLOCK}}^{\wedge} = \left[ \begin{array}{c|c|c}
 *1 & & *2 \\
 & M_p & \\
 \hline
 & & M_d^{\dagger} \\
 *3 & & \\
 \hline
 & & M_e^{\dagger} \\
 *3 & & \\
 \hline
 \end{array} \right] \\
 M_{\text{BLOCK}}^{e,\succ} = \left[ \begin{array}{c|c|c}
 *5 & & *6 \quad *4 \\
 *8 & M_p^e & *7 \\
 \hline
 & & M_d^{\dagger,e} \\
 *9 & & \\
 \hline
 & & M_e^{\dagger,e} \\
 *9 & & \\
 \hline
 \end{array} \right]
 \end{array}$$

Again,  $M_{\text{BLOCK}}^{\wedge}$  is a generalized mass matrix, so we expect it to be symmetric and positive definite.

**Lemma 4.3.4.**  $M_{\text{BLOCK}}^{\wedge}$  is symmetric and positive definite.

*Proof.* The proof is very similar to the proof of Lemma 4.3.2.

\*2 = \*3, so symmetry is obvious from the definition of the matrix, positive definiteness can easily be verified using the definition: As before, let

$$x = [x_0, x_1, \dots, x_{a-1}, x_a | x_{a+1}, x_{a+2}, \dots, x_{b-1}, x_b | x_{b+1}, x_{b+2}, \dots, x_{c-1}, x_c]^T$$

and  $p, d, e$  as in the proof of Lemma 4.3.2. Then  $x \cdot M_{\text{BLOCK}}^{\widehat{}} x$  can be written as

$$\begin{aligned}
& \begin{bmatrix} x_0 \\ x_1 \\ \vdots \\ x_{a-1} \\ x_a \\ \hline x_{a+1} \\ x_{a+2} \\ \vdots \\ x_{b-1} \\ x_b \\ \hline x_{b+1} \\ x_{b+2} \\ \vdots \\ x_{c-1} \\ x_c \end{bmatrix} \cdot \begin{bmatrix} 2p+2d+2e & p & & & & & d & & & e \\ & p & 4p & p & & & & & & \\ & & \ddots & & & & & & & \\ & & & p & 4p & p & & & & \\ & & & & p & 2p & & & & \\ \hline & & & & & & 2d & d & & \\ & & & & & & d & 4d & d & \\ & & & & & & & \ddots & & \\ & & & & & & & d & 4d & d \\ & & & d & & & & & d & 4d \\ \hline & & & & & & & & & 2e & e \\ & & & & & & & & & e & 4e & e \\ & & & & & & & & & & \ddots & \\ & & & & & & & & & e & 4e & e \\ & & & e & & & & & & & e & 4e \end{bmatrix} \begin{bmatrix} x_0 \\ x_1 \\ \vdots \\ x_{a-1} \\ x_a \\ \hline x_{a+1} \\ x_{a+2} \\ \vdots \\ x_{b-1} \\ x_b \\ \hline x_{b+1} \\ x_{b+2} \\ \vdots \\ x_{c-1} \\ x_c \end{bmatrix} \\
&= (2p+2d+2e)x_0^2 + px_0x_1 + dx_0x_b + ex_0x_c + px_1x_0 + 4px_1^2 + px_1x_2 + px_2x_1 + 4px_2^2 + px_2x_3 + \dots \\
&\quad + px_{a-1}x_{a-2} + 4px_{a-1}^2 + px_ax_{a-1} + 2px_a^2 \\
&\quad + 2dx_{a+1}^2 + dx_{a+1}x_{a+2} + dx_{a+2}x_{a+1} + 4dx_{a+2}^2 + dx_{a+2}x_{a+3} + 4dx_{a+3}^2 + \dots \\
&\quad + dx_{b-1}x_{b-2} + 4dx_{b-1}^2 + dx_{b-1}x_b + dx_bx_0 + dx_bx_{b-1} + 4dx_b^2 \\
&\quad + 2ex_{b+1}^2 + ex_{b+1}x_{b+2} + ex_{b+2}x_{b+1} + 4ex_{b+2}^2 + ex_{b+2}x_{b+3} + 4ex_{b+3}^2 + \dots \\
&\quad + ex_{c-1}x_{c-2} + 4ex_{c-1}^2 + ex_{c-1}x_c + ex_cx_0 + ex_cx_{c-1} + 4ex_c^2 \\
&= px_0^2 + p(x_0+x_1)^2 + 2px_1^2 + p(x_1+x_2)^2 + 2px_2^2 + \dots + 2px_{a-1}^2 + p(x_{a-1}+x_a)^2 + px_a^2 \\
&\quad + dx_{a+1}^2 + d(x_{a+1}+x_{a+2})^2 + 2dx_{a+2}^2 + \dots + 2dx_{b-1}^2 + d(x_{b-1}+x_b)^2 + 2dx_b^2 + d(x_b+x_0)^2 + dx_0^2 \\
&\quad + ex_{b+1}^2 + e(x_{b+1}+x_{b+2})^2 + 2ex_{b+2}^2 + \dots + 2ex_{c-1}^2 + e(x_{c-1}+x_c)^2 + 2ex_c^2 + e(x_c+x_0)^2 + ex_0^2 \\
&\geq (p+d+e)x_0^2 + 2px_1^2 + 2px_2^2 + \dots + 2px_{a-1}^2 + px_a^2 + dx_{a+1}^2 + 2dx_{a+2}^2 + \dots + 2dx_{b-1}^2 + 2dx_b^2 \\
&\quad + ex_{b+1}^2 + 2ex_{b+2}^2 + \dots + 2ex_{c-1}^2 + 2ex_c^2 \geq 0
\end{aligned}$$

and equality holds if and only if  $x = 0$ .  $\square$

*Remark 4.3.5.*  $M_{\text{BLOCK}}^{e,\widehat{}}$  is not spd, its structure is not even symmetric.

### 4.3.3 Implementation and Convergence Experiments

#### Implementation

The methods presented here were implemented using the quocmesh library. We wrote special band matrix classes for the  $M^b$  and  $M^t$  blocks that are optimized for fast matrix-vector multiplication.

BlockOperators were used for the matrix block structures, MultiVectors to store the vectors of unknowns.

In contrast to the case of one segment, the system matrices are no longer tridiagonal, so Gaussian elimination or banded solvers are no longer efficient. Renumbering the segments in

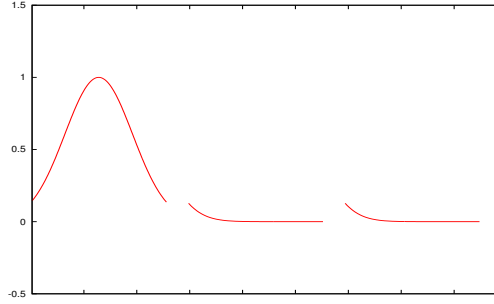


Figure 4.12: Initial temperature content profile used to verify order of convergence. The parent segment is shown on the left, the first daughter in the center and the second daughter on the right. The flow will be directed to the right.

order to decrease overall bandwidth could be applied (e. g. by the Cuthill-McKee algorithm, see [21, 10]), but still a lot of fill-in would be produced.

From Lemmas 4.3.2 and 4.3.4, we know that the system matrices are symmetric and positive definite, so we can apply a CG solver.

### Convergence Experiments

[29] refers to [37] for the following error estimate for ELLAM advection in 1D and zero source term.

Our advection problem on the trees consists of individual such problems coupled by flows through bifurcations, so we expect the same convergence order for our methods.

**Proposition 4.3.6.** *Let  $u(x, t)$  be the exact solution and  $U(x, t)$  be the ELLAM approximation. Then the following error estimate holds*

$$\max_k \|U(\cdot, t^k) - u(\cdot, t^k)\|_{L^2(\Omega)} + \|U(L, \cdot) - u(L, \cdot)\|_{L^2([0, T])} \leq C (h^2 + \tau). \quad (4.47)$$

We performed a few numerical experiments to check whether this convergence estimate holds for our method on trees.

We considered a simple  $\prec$  bifurcation ( $p \prec d, e$ ) for convergence experiments and plotted temperature content as described at the very beginning of this chapter. The plots show the profile on  $p$ ,  $d$  and  $e$  from left to right.

Our initial profile was a *Gaussian bell curve* shown in Figure 4.12 with appropriate inflow data. Our source term was assumed to be zero.

In cases 1a and 1b, the flow is split 50 : 50 in the two daughter segments, 1a advects the bell until it lies in the two daughter segments, 1b advects them further out. In case 2 we used a 75 : 25 split, in case 3 we used different lengths and cross section areas for the three segments. The parameters are shown in Table 4.1.

The final profiles are shown in Figure 4.13

We chose  $n_p = 17, 33, 65, 129, 257, 513, 1025, n_d = n_e = n_p - 1$ .

To obtain second-order convergence in  $h$ , we need to use  $\tau = h^2$  due to (4.47). However, using a larger time step  $\tau = h$ , we do not lose accuracy.

Case	1a	1b	2	3
$l_p$	1.0	1.0	1.0	1.15
$l_d$	1.0	1.0	1.0	1.34
$l_e$	1.0	1.0	1.0	0.85
$A_{\emptyset,p}$	1.0	1.0	1.0	1.23
$A_{\emptyset,d}$	0.5	0.5	1.0	1.47
$A_{\emptyset,e}$	0.5	0.5	1.0	0.82
$v_p$	0.8	0.5	0.8	0.8
$v_d$	0.4	0.4	0.6	0.421714
$v_e$	0.4	0.4	0.2	0.4444
$\theta_d$	0.5	0.5	0.75	0.63
$\theta_e$	0.5	0.5	0.25	0.37
$T$	1.25	2.50	1.25	1.0

Table 4.1: Parameters for convergence experiments

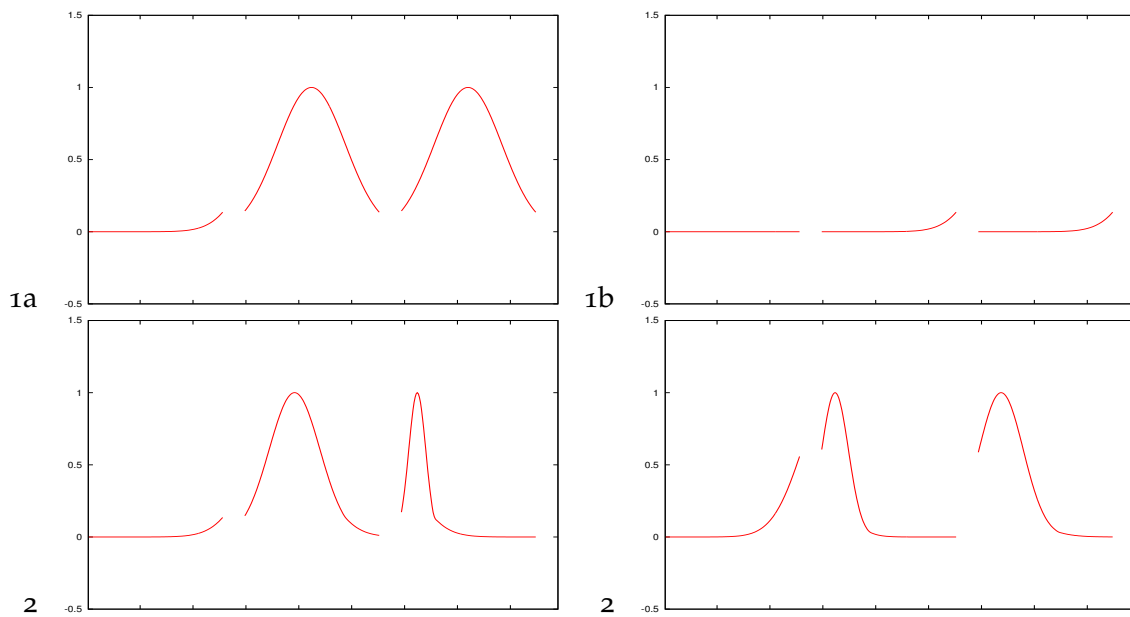


Figure 4.13: Final temperature content profiles in the convergence experiment, top: cases 1a, 1b, bottom: cases 2, 3 for  $n_p = 129$ . The initial profile, see Figure 4.12 has advected from the parent segment (left) into the two daughter segments (center and right), direction of flow was to the right.

This is also the stability limit due to the *CFL condition* (in [9]): Our method cannot handle  $\rho > 1$ , so the CFL condition is  $\frac{v\tau}{h} < 1$ , and our velocities satisfy  $v \leq 1$ .

Results of our convergence experiment are shown in Table 4.2 and plotted in Figure 4.14. The computation was performed on a desktop PC with an 1 GHz Athlon CPU.

### Limitations of our Method

Other experiments show some limitations: our ELLAM cannot handle discontinuities very well. An example for this is shown in Figure 4.15.

We start with a rectangular and a triangular pulse on the parent segment of a  $<$  bifurcation, as an inflow over time we use a cosine.

Oscillations of high frequency and significant magnitude appear in the downflow direction of the discontinuity as it is advected. These oscillations are smoothed out slightly when transferred to the daughter segment.

The amplitude of the triangular pulse slowly decreases as the pulse is advected. This is an effect of *numerical diffusion* or *dissipation*.

At the outflow boundary of the two daughter segments, the profile is advected out smoothly without any visible oscillations in upflow direction.

In Figure 4.16, we used the same initial profile on the two daughter segments and equal speed. In this case, temperature and temperature content (but not energy content) are continuous across the bifurcation.

In case of a  $>$  bifurcation combining the two incoming flows, a related effect can be observed. Unlike in the splitting case where the values are continuous at the bifurcation, the inflow to the parent segment in case of combination becomes a weighted average of the outflows of the two daughter segments. So, in general, it is not continuous.

In Figure 4.17, we have combined two cosine profiles of different frequency arriving at the bifurcation out of phase. In the parent segment, we see a correctly weighted average. However, in the daughter segments we see oscillations in the upflow direction of the bifurcation.

Numerically, this leads to oscillations in the upflow direction of the discontinuity at the bifurcation.

### 4.3.4 Further Extensions: $\rho > 1$ and Multifurcations

The method presented above can be generalized to velocity greater than one grid cell per time step, allowing bigger time steps for fixed grid on the segments.

Assuming that the velocities are still small enough so that no ELLAM equation is affected by two bifurcations at the same time, the following changes:

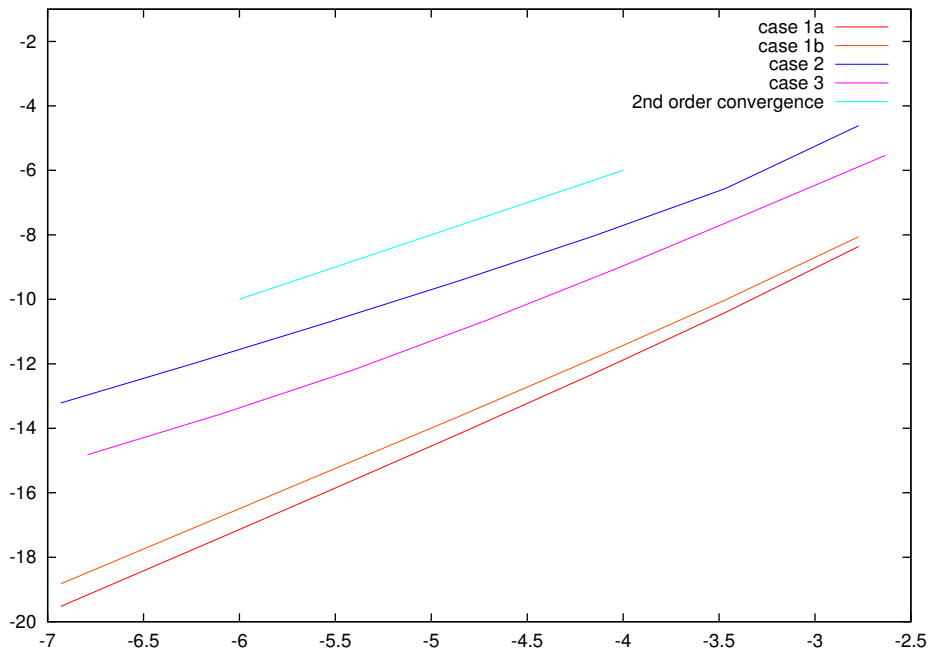
- The first  $\lfloor \rho \rfloor + 2$  equations are affected by the inflow boundary rather than only the first two, see (4.25) and (4.26). Here,  $\lfloor \rho \rfloor := \max \{n \in \mathbb{N} \mid n \leq \rho\}$ .
- Thus  $\bar{b}_p^k$  has  $\lfloor \rho \rfloor + 2$  nonzero entries at the beginning, see (4.32) and (4.33). They still depend on  $R_{\text{in}}^k$  and  $R_{\text{in}}^{k+1}$ .
- The last  $\lfloor \rho \rfloor + 1$  equations are affected by the outflow rather than only the last one, (4.28).

case 1a:			case 1b:		
$h$	error	cputime(s)	$h$	error	cputime
0.0625	2.33866e-04	0.01	0.0625	3.16118e-04	0.02
0.03125	3.02458e-05	0.04	0.03125	4.46117e-05	0.08
0.015625	4.46823e-06	0.15	0.015625	7.15554e-06	0.29
0.0078125	7.05806e-07	0.53	0.0078125	1.21150e-06	1.06
0.00390625	1.15822e-07	2.10	0.00390625	2.13716e-07	4.14
0.00195312	1.94554e-08	8.52	0.00195312	3.77569e-08	17.03
0.000976562	3.31875e-09	39.75	0.000976562	6.67517e-09	78.17

case 2:			case 3:		
$h$	error	cputime(s)	$h_p$	error	cputime
0.0625	9.94837e-03	0.01	0.071875	3.94829e-03	0.01
0.03125	1.41214e-04	0.03	0.0359375	6.84522e-04	0.04
0.015625	3.19938e-04	0.11	0.0179687	1.22199e-04	0.13
0.0078125	8.12095e-05	0.41	0.00898437	2.36154e-05	0.49
0.00390625	2.19118e-05	1.56	0.00449219	5.08129e-06	1.89
0.00195312	6.20890e-06	6.44	0.00224609	1.28790e-06	7.65
0.000976562	1.82766e-06	31.21	0.001123045	3.66321e-07	38.20

Table 4.2: Results of the convergence experiments

Figure 4.14: loglog plot of error vs  $h$  for the different sets of parameters.

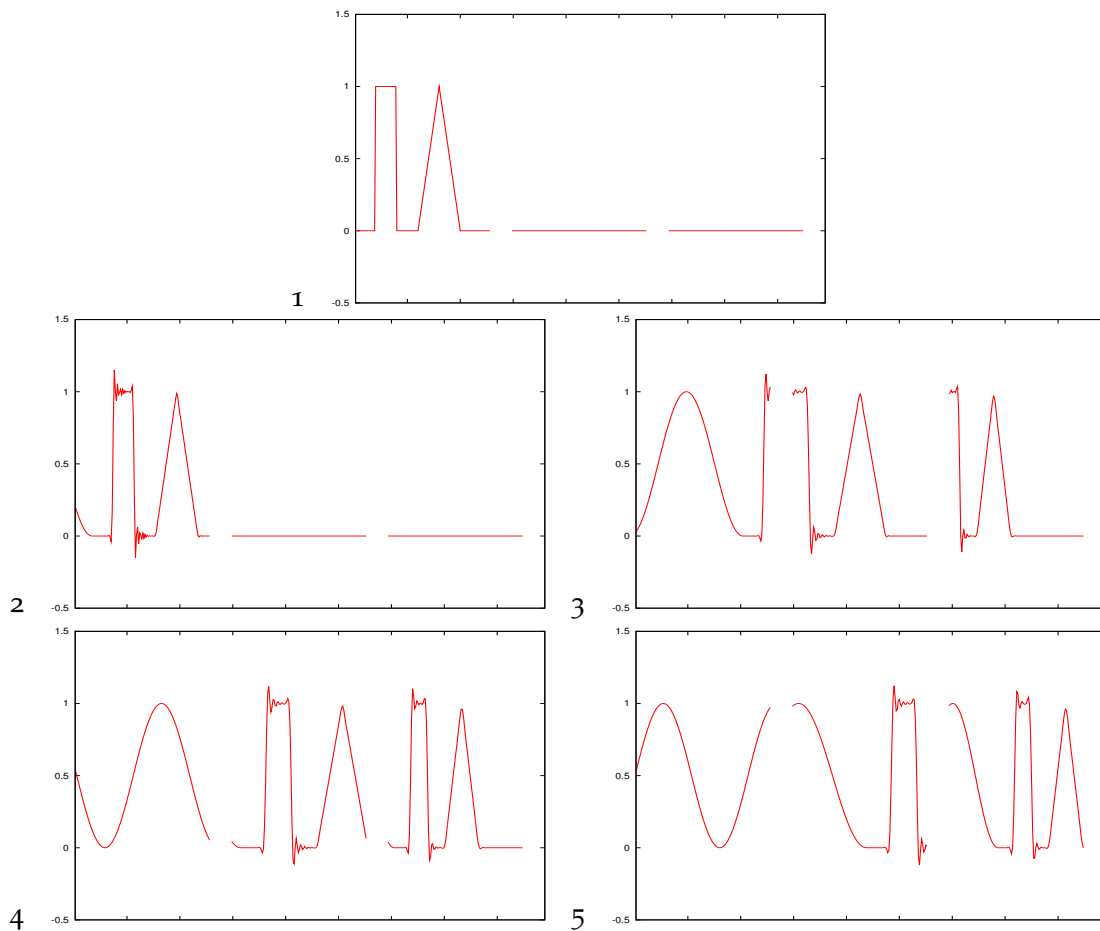


Figure 4.15: Advection of an temperature content profile split at a bifurcation and oscillating inflow. The parent segment is shown on the left, the two daughters in the center and on the right, direction of flow is to the right. The flow velocities of the two daughter segments are different.

1: initial profile

2: initial profile advected within parent segment

3: discontinuity being split at the bifurcation

4: initial rectangular and triangular pulse being advected through the daughter segments

5: continuous oscillation being split at the bifurcation

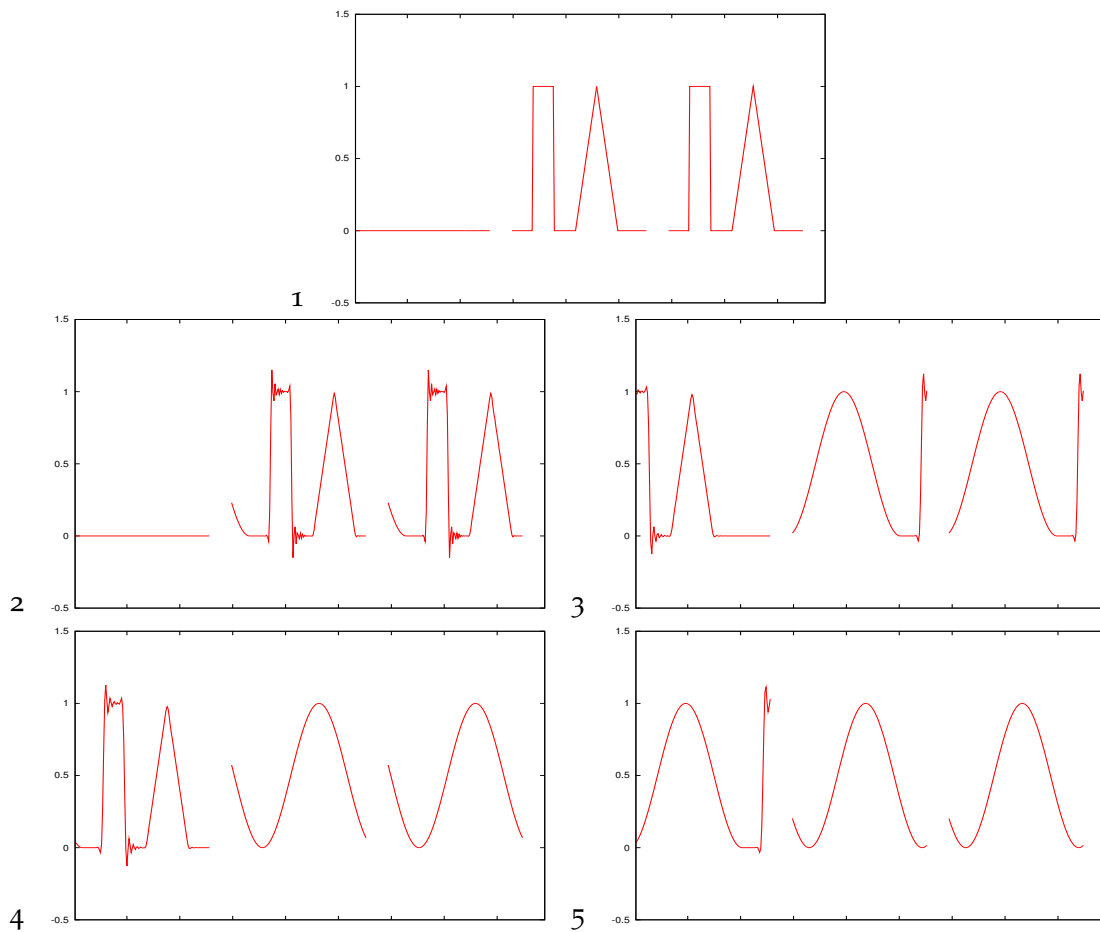


Figure 4.16: Advection of a temperature content profile combined at a bifurcation and oscillating inflow. The direction of flow is to the right, flow out of the daughter segments (center, right) is into the parent segment on the left. The flow velocities of the two daughter segments are equal.

1: initial profile within the daughter segments

2: initial profile advected within the daughter segments

3: discontinuity being combined at the bifurcation

4: initial rectangular and triangular pulses combined being advected through the parent segment

5: continuous oscillations being combined at the bifurcation, discontinuity being advected out of the parent segment

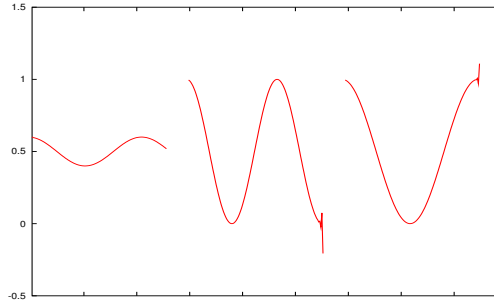


Figure 4.17: Combination of two cosine (different frequency) shaped temperature content profiles: The discontinuity causes upflow oscillations. Again, the direction of flow is to the right, out of daughter segments (center, right) into parent segment (left).

- $M^e$  matrices still have four adjacent bands, but they are shifted to the left by  $\lfloor \rho \rfloor$ , see (4.38). Their entries can still be computed as before by taking only the fractional part of  $\rho$  in (4.31). Other entries in the top left and the bottom right corner have to be treated as special cases.
- The flow transfer between segments couples the last  $\lfloor \rho \rfloor + 2$  nodal values of the upflow segment(s) and the first  $\lfloor \rho \rfloor + 2$  of the downflow segment(s). So the sparsity structure of the  $C^e$  matrices change. The additional entries are shifted further to the left, maybe into a different block, also the integrals change.

Coupling becomes more complicated if velocities are still bigger so that more than one bifurcation needs to be considered during one time step.

Moreover, the method above can be generalized to multifurcations. In this case we get more than two times two nonzero off-diagonal blocks. For an intermediate node (a monofurcation), it is only one times two nonzero off-diagonal blocks.

## 4.4 Treatment of Terminal Segments

### 4.4.1 Terminal Segments in the Arterial Tree

In a terminal segment of the arterial tree, we have outflow of mass, thus energy, along the whole segment  $[sK, sK + \ell_s]$ . Without loss of generality, assume<sup>4</sup>  $s = 0$  and set  $\ell = \ell_s$ . Note that our model assumes that there is no heat conduction between terminal segments and the surrounding tissue.

As  $u$  is the energy per length contained in the segment, we want  $u$  to drop off to zero along terminal segments. In 2D, cross section area is proportional to radius, so we can view this as regular advection of temperature ( $\sim$  energy per volume), integrated over an *apparent cross section area* that drops off linearly to zero. Note that  $A_\emptyset$  is always constant along segments and does not mean the apparent cross section area.

<sup>4</sup>To simplify notation only. In this section we relax the condition that segment 0 is always the root segment

The temperature  $\vartheta$  on a terminal segment of the arterial tree is given by

$$\vartheta(\bar{\xi}) = \frac{1}{C\rho} \cdot \frac{u(\bar{\xi})}{A_{\varnothing} \cdot \left(1 - \frac{\bar{\xi}}{\ell}\right)}. \quad (4.48)$$

We could use an approach based on decreasing cross section area, modify the basis functions and incorporate the outflow in the transport. The approach presented here, however, allows an easier treatment of energy exchange processes with the surrounding tissue.

To motivate the appropriate right hand side, suppose we advect a profile of constant non-zero temperature through the tree. In this case, we want the  $u$  profile to drop off linearly along a terminal segment. So we need a right hand side term satisfying

$$\begin{aligned} u(t, x) &= \frac{-1}{v} \int_x^{\ell} f(y) \, dy \\ \Rightarrow u(t, x) &= \frac{-1}{v} (F(\ell) - F(x)) \end{aligned}$$

where  $F(z) = \int_0^z f(y) \, dy$ , so

$$\begin{aligned} \partial_x u(t, x) &= \frac{1}{v} \cdot \partial_x F(x) \\ &= \frac{1}{v} \cdot f(x). \end{aligned}$$

Using the linear drop off  $\partial_x u(t, x) = \frac{u(t, \ell) - u(t, x)}{\ell - x}$  to zero,  $u(t, \ell) = 0$ , we obtain

$$\begin{aligned} \frac{-u(t, x)}{\ell - x} &= \frac{1}{v} \cdot f(x) \\ \Rightarrow f(x) &= -v \cdot \frac{u(t, x)}{\ell - x}. \end{aligned}$$

Below, we show that this makes sense on the closed interval despite the root of the denominator for  $x \rightarrow \ell$ .

So our advection problem on (outflow) terminal segments is described by

$$\begin{aligned} \partial_t u(t, x) + v \cdot \partial_x u(t, x) &= f_f(t, x) = -v \cdot \frac{u(t, x)}{\ell - x} \quad \text{on } [0, \ell) \\ u(0, x) &= u_0(t) \\ u(t, 0) &= u_{\text{in}}(t). \end{aligned} \quad (4.49)$$

**Proposition 4.4.1** (Existence of a solution). *If the boundary data for  $x = 0$  is mapped to  $C^1$  initial data as in (4.5), there is a unique solution to problem (4.49) given by*

$$u(t, x) = u_0(x - vt) \cdot \frac{\ell - x}{\ell}. \quad (4.50)$$

*Proof.*

$$\begin{aligned} u(t, x) &= u_0(x - vt) \cdot \frac{\ell - x}{\ell} \\ \partial_t u(t, x) &= u'_0(x - vt) \cdot (-v) \cdot \frac{\ell - x}{\ell} \\ \partial_x u(t, x) &= u'_0(x - vt) \cdot \frac{\ell - x}{\ell} + u_0(x - vt) \cdot \frac{-1}{\ell}, \end{aligned}$$

so

$$\begin{aligned} \partial_t u(t, x) + v \cdot \partial_x u(t, x) &= v \cdot u_0(x - vt) \cdot \frac{-1}{\ell} \\ &= \frac{-v}{\ell} \cdot u(t, x) \frac{\ell}{\ell - x} \\ &= -v \cdot \frac{u(t, x)}{\ell - x}. \end{aligned}$$

Uniqueness is proved as for Proposition 4.2.1: let  $s(t, x)$  be any solution of the initial value problem, then the difference function  $d(t, x) = s(t, x) - u(t, x)$  must satisfy

$$\begin{aligned} \partial_t d(t, x) + v \cdot \partial_x d(t, x) &= 0 \quad (t, x) \in [0, \infty) \times \mathbb{R} \\ d(0, x) &= 0 \quad \text{on } \{0\} \times \mathbb{R}, \end{aligned}$$

hence  $d(t, x) = 0 \forall (t, x) \in [0, \infty) \times \mathbb{R}$ , so  $s = u$ .  $\square$

The solution (4.50) can be extended to  $x = \ell$ :  $u(t, \ell) = 0$ .

Approximate the right hand side of the weak form (4.23) as in (4.24) to obtain temporal quadrature:

$$\begin{aligned} \int_0^\ell \int_{t^k}^{t^{k+1}} f_f(t, x) w(t, x) &= \int_0^\ell \int_{t^k}^{t^{k+1}} -v \cdot \frac{u(t, x)}{\ell - x} \cdot w(t, x) \\ &\approx \frac{-v\tau}{2} \left( \int_0^\ell \frac{u(t^k, x) w(t^k, x)}{x - \ell} + \int_0^\ell \frac{u(t^{k+1}, x) w(t^{k+1}, x)}{x - \ell} \right) \end{aligned}$$

As for the spatial quadrature, we need to pay attention to the singularity of  $\frac{1}{x-\ell}$  for  $x \rightarrow \ell$ . This factor  $\frac{1}{x-\ell}$  is assigned to the test functions  $w$ , so the spatial discretization can be computed by using mass matrix  $M^+$  and ELLAM matrix  $M^{+,e}$  with each row scaled accordingly, corresponding to a multiplication with a diagonal matrix on the left:

$$\bar{B}^k = \frac{-v\tau}{2\ell} \left[ \text{diag} \left( \frac{n}{n-i-1} \right)_{i=0, \dots, n-1} \cdot M^+ + \text{diag} \left( \frac{n}{n-i-1+\rho} \right)_{i=0, \dots, n-1} \cdot M^{+,e} \right] \bar{U}^k \quad (4.51)$$

where, in the first diagonal matrix, we set  $\frac{0}{0} := 0$  because this line describes the influence of  $\bar{U}_{n-1}^k$  (analytically 0) on  $\bar{U}^{k+1}$ .

Near the leaf node, i. e. at the end of the terminal segment, this approximation becomes worse because of the singularity of  $\frac{1}{\ell-x}$ . We need to be particularly careful when interpreting these energy content values as temperatures by division by the small apparent cross section areas.

*Remark 4.4.2.* Individually, the error in the spatial quadrature is biased.  $\frac{1}{x-\ell}$ , by which the test functions  $w(t, x)$  are weighted, is a decreasing and strictly concave function on  $(0, \ell)$ . In the quadrature, it is approximated by the value at the center of the support of  $w_i(t, \cdot)$ . Hence, the quadrature tends to underestimate the intensity of our source (loss of energy content).

With a better combined temporal-spatial quadrature or exact integration, we should be able to improve the accuracy here.

#### 4.4.2 Terminal segments in the Venous Tree

In case of the venous tree, inflow accumulating along a terminal segment is determined by the temperature of the surrounding tissue. Again, suppose the terminal segment is  $[0, \ell]$ .

The temperature  $\vartheta$  on a terminal segment of the venous tree is given by

$$\vartheta(\tilde{\zeta}) = \frac{1}{C\rho} \cdot \frac{u(\tilde{\zeta})}{A_{\varnothing} \cdot \frac{\tilde{\zeta}}{\ell}}. \quad (4.52)$$

If a terminal segment lies within an area of tissue of constant temperature (energy density), we want it to have an energy content corresponding to that temperature at the end. For this, we need a right hand side term  $f(t, x) = \frac{A_{\varnothing}v}{\ell} u_{\text{tis}}(t, \psi^{-1}(x))$  where  $u_{\text{tis}}$  is the energy density of the surrounding tissue.

In general, the advection problem on a terminal segment of the venous tree is given by

$$\begin{aligned} \partial_t u(t, x) + v \cdot \partial_x u(t, x) &= f_w(t, x) = \frac{A_{\varnothing}v}{\ell} \cdot u_{\text{tis}}(t, \psi^{-1}(x)) \\ u(0, x) &= u_0(t) \\ u(t, 0) &= 0 \end{aligned} \quad (4.53)$$

where  $\psi^{-1}$  maps the point  $x$  on the segment to its corresponding location in 2D, see (2.1) and the boundary condition  $u(t, 0) = 0$  reflects that the energy advected into the segment is zero and inflow happens only along the segment.

This type of source terms is treated in (4.34).

Again, this approach allows us to easily describe the corresponding sink terms in the diffusion problem.

#### 4.4.3 Implementation and Results

We modified the  $\prec$  bifurcation such that the second daughter segment becomes an outflow segment and we applied a source term to part of the first daughter segment. We started with a continuous initial profile and used cosine inflow condition, the flow is split 60 : 40 between the two daughters. The result for this is shown in Figure 4.18.

The first plot shows the initial profile we started with, then we can see how the source term affects the first daughter segment and how constant temperature inflow to the second daughter segment does not change the profile on this segment. Finally, the cosine waves advect through the bifurcation and are affected by the source term on the first daughter and by the outflow source on the second daughter.

We also modified the  $\succ$  bifurcation such that there is constant inflow to the first daughter and the second daughter segment is a terminal inflow segment. This is a 50 : 50 flow combination. In this case, we applied no further source terms.

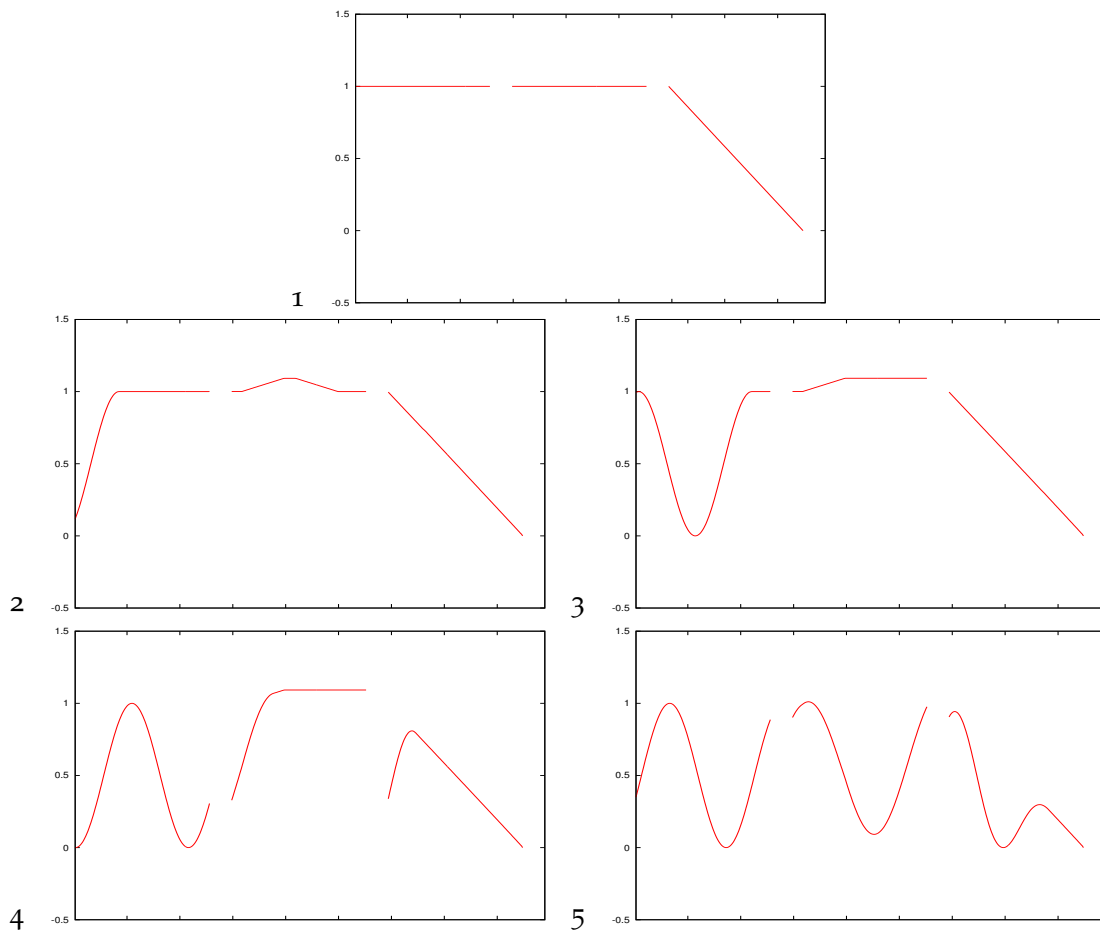


Figure 4.18: Advection of a temperature content profile split at a bifurcation with oscillating inflow, a source term on one daughter (center) and a terminal segment as the other daughter (right): Initial profile and four time steps. The parent segment is shown on the left, the direction of flow is to the right.

1: initial profile

2: oscillating inflow on parent segment, influence of the source term on the first daughter (center), linear drop-off on the second daughter

3: influence of heating on the first daughter has fully developed

4: oscillating pattern reaches both daughters

5: oscillating pattern advected through both daughters and experiences heating in the first daughter (center) and linear drop-off of the amplitude on the second daughter (right)

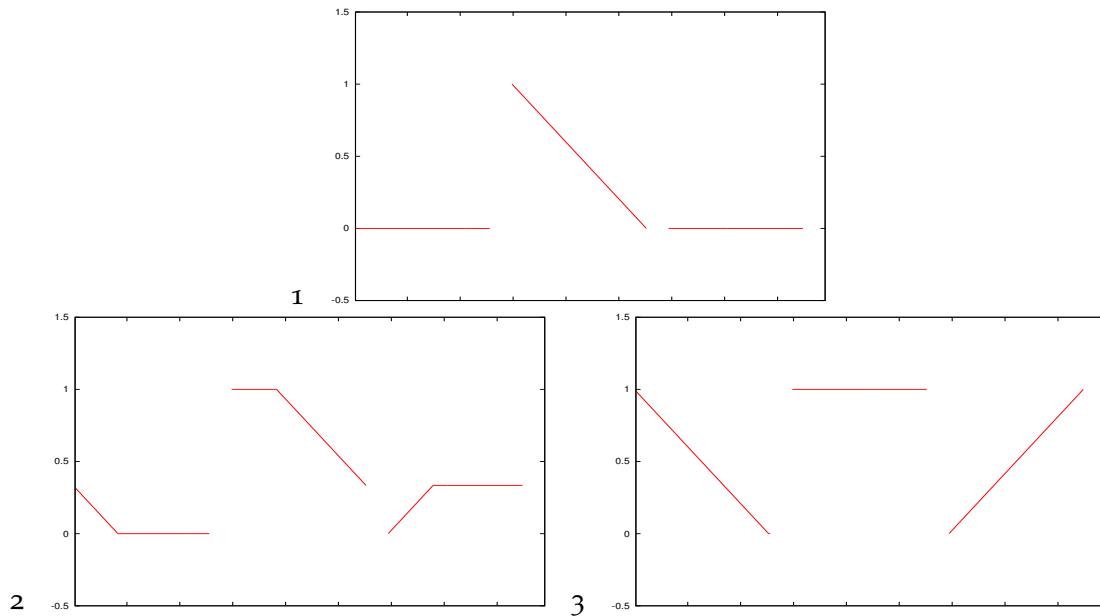


Figure 4.19: Advection of a temperature content profile combined at a bifurcation with one terminal inflow segment (right): Initial profile and two time steps. The parent segment is shown on the left, the other (non-inflow) daughter in the center, direction of flow is to the right.

1: initial profile: zero initial conditions on parent segment and second daughter (right), the profile on the first daughter (center) is chosen such that there will be no discontinuity at the bifurcation

2: boundary condition for the first daughter (center) is constant and leads to a continuous profile, inflow source terms along the second daughter (right) show first effects, flow combination at the bifurcation into the parent segment occurs continuously

3: fully developed influence of the inflow source terms on the second daughter (right) has just reached the parent segment

In Figure 4.19, first the initial profile is shown, on the first daughter (center) it is chosen such that temperature is continuous at the bifurcation and we do not observe numerical artefacts due to discontinuities. The next two plots show how the terminal inflow to the second daughter segment increases its energy content.

## 4.5 ELLAM on Vessel Trees

We now have all necessary tools to set up a simulation of advection on full arterial and venous trees.

Recall how the flow into and out of the different types of segments is treated:

On the arterial tree,

- root segment: inflow at root node is given explicitly, see (4.32), (4.33); outflow is treated implicitly via coupling terms of the daughter segments, see (4.41), (4.42), (4.43)
- intermediate segment: inflow is computed implicitly via coupling, see (4.41), (4.42), (4.43); same for outflow.
- terminal segment: inflow is computed via coupling, see (4.41), (4.42), (4.43), outflow on the whole segment is described by (4.51), there is no outflow at the leaf node.

on the venous tree,

- root segment: inflow is computed via coupling, see (4.44), (4.45), (4.46); outflow at root node can be computed, see (4.29).
- intermediate segment: inflow is computed via coupling, see (4.44), (4.45), (4.46); same for outflow
- terminal segment: inflow at leaf node is zero, inflow over whole segment described by source as in (4.53); outflow is computed via coupling terms of the daughter segments, see (4.44), (4.45), (4.46);

The extension of the block system presented for a single bifurcation can easily be extended to more complex trees. In this case, our block systems become bigger and the coupling matrices have to be put and added in the correct position corresponding to the connectivity structure of the tree.

For arterial trees, the block system for a venous tree is set up as follows: For each bifurcation  $(p \prec d, e)$ ,

- add  $C_{p,d}^{\prec}, C_{p,e}^{\prec}$  to the block  $(p, p)$  of  $M_{\text{BLOCK}}^{\prec}$
- put  $C_{p,d}^{\prec,u}$  to the block  $(p, d)$  of  $M_{\text{BLOCK}}^{\prec}$
- put  $C_{p,d}^{\prec,l}$  to the block  $(d, p)$  of  $M_{\text{BLOCK}}^{\prec}$
- put  $C_{p,e}^{\prec,u}$  to the block  $(p, e)$  of  $M_{\text{BLOCK}}^{\prec}$
- put  $C_{p,e}^{\prec,l}$  to the block  $(e, p)$  of  $M_{\text{BLOCK}}^{\prec}$
- add  $C_{p,d}^{e,\prec}, C_{p,e}^{e,\prec}$  to the block  $(p, p)$  of  $M_{\text{BLOCK}}^{e,\prec}$

- put  $C_{p,d}^{e,\prec,u}$  to the block  $(p, d)$  of  $M_{\text{BLOCK}}^{e,\prec}$
- put  $C_{p,d}^{e,\prec,l}$  to the block  $(d, p)$  of  $M_{\text{BLOCK}}^{e,\prec}$
- put  $C_{p,e}^{e,\prec,u}$  to the block  $(p, e)$  of  $M_{\text{BLOCK}}^{e,\prec}$
- put  $C_{p,e}^{e,\prec,l}$  to the block  $(e, p)$  of  $M_{\text{BLOCK}}^{e,\prec}$

For each bifurcation  $(d, e \succ p)$ ,

- add  $C_p^\succ$  to block  $(p, p)$  of  $M_{\text{BLOCK}}^\succ$
- put  $C_{d,p}^{\succ,u}$  into block  $(p, d)$  of  $M_{\text{BLOCK}}^\succ$
- put  $C_{d,p}^{\succ,l}$  into block  $(d, p)$  of  $M_{\text{BLOCK}}^\succ$
- put  $C_{e,p}^{\succ,u}$  into block  $(p, e)$  of  $M_{\text{BLOCK}}^\succ$
- put  $C_{e,p}^{\succ,l}$  into block  $(e, p)$  of  $M_{\text{BLOCK}}^\succ$
- add  $C_p^{e,\succ}$  to block  $(p, p)$  of  $M_{\text{BLOCK}}^{e,\succ}$
- put  $C_{d,p}^{e,\succ,u}$  into block  $(p, d)$  of  $M_{\text{BLOCK}}^{e,\succ}$
- put  $C_{d,p}^{e,\succ,l}$  into block  $(d, p)$  of  $M_{\text{BLOCK}}^{e,\succ}$
- put  $C_{e,p}^{e,\succ,u}$  into block  $(p, e)$  of  $M_{\text{BLOCK}}^{e,\succ}$
- put  $C_{e,p}^{e,\succ,l}$  into block  $(e, p)$  of  $M_{\text{BLOCK}}^{e,\succ}$

The discretization of the segments of our trees is always such that the (1D) grid on the root segment has at least four grid points and grids on intermediate and terminal segments have at least three grid points. This avoids dealing with two segment boundaries within the same ELLAM equation.

**Definition 4.5.1.** The *grid spacings* on a tree are

$$h_j = \begin{cases} \frac{l_j}{\text{number of grid points on } j-1} & \text{for the root segment } j \\ \frac{l_j}{\text{number of grid points on } j} & \text{for intermediate and terminal segments } j \end{cases}$$

because non-root segments do not have grid points assigned to their initial points.

**Definition 4.5.2.** A grid with at least four grid points on the root segment and at least three on all other segments is said to be of *level*  $d$  if all grid spacings satisfy  $h_j \leq 2^{-d}$ .

tree	level	# timesteps	cputime (s)	cputime / time step (ms)
8-tree	7	800	4.52	5.65
	8	1600	15.62	9.76
	9	3200	50.18	15.68
	10	6400	291.87	45.61
16-tree	9	3200	96.14	30.04

Table 4.3: Number of time steps and computation times for advection on an 8-tree and a 32-tree.

#### 4.5.1 Implementation and Results

As an example, we used a pair of tree with 8 terminal segments each.

We specified an oscillating inflow to the arterial tree with outflow on the terminal segments, for the venous tree we assumed the surrounding tissue to have constant temperature of 1. On both trees the initial temperature was set to 0. This is not realistic because initial temperature distributions should be such that the vessels have the same local temperatures as the surrounding tissue. It is used to demonstrate how our method works on trees.

The output shown in Figure 4.20 is the parallel projection of a three-dimensional plot: in the  $xy$  plane, we show the structure of our tree (red for the arterial tree, blue for the venous tree), in  $z$  direction, the temperature contents at the corresponding position are shown. On non-terminal segments, this corresponds to temperature, on terminal segments, this shows the drop-off from an temperature content corresponding to full temperature to zero at leaf nodes.

In addition to the height, the values are also color-coded on the same color scale as in Figure 2.10, red corresponding to 1 and blue corresponding to 0. These plots were written out as eps files by our program.

On the arterial tree, we can see that

- our inflow profile is advected into the tree
- temperature transitions at bifurcations are  $C^0$  but not  $C^1$  since the velocities change
- values drop down to zero on terminal segments (in this case, the amplitude of the raised cosine waves drops down to zero linearly along the terminal segments)

on the venous tree, we can see that

- terminal segments collect energy according to their length
- the profiles are advected out of the tree
- transitions at bifurcations are discontinuous and lead to upflow oscillations
- at the root, the profile advects out without visible numerical upflow effects

The computation above was performed with a grid of level 8. To show the influence of a coarser and finer discretization, we repeated the computation above with grids of level 7 to 10 and show the result of the advection until the same time in Figure 4.21. Computation time for these calculations are shown in Table 4.3.

Due to the limitation that  $\rho$  must be less than 1 on each segment and as our flow velocities are less than 1, the time step we can use is limited, so the number of time steps increases if a finer discretization is used.

In Figure 4.21, we can see some effects on the coarser tree:

- In the arterial tree in the terminal segment on the left below the root, the high frequency oscillations cannot be resolved on the terminal segment, so they are lumped together.
- In the venous tree in the central inflow segment, the discontinuity at the end of the segment leads to upflow oscillations. These sawtooth-like ripples are less prominent in the trees with finer resolution.
- The venous tree is not in steady state yet (constant temperature profile has not been fully advected until the root), and due to different velocities there are discontinuities at the bifurcations in the lower half of the venous tree. Upflow oscillations appear, their magnitude does not decrease on finer resolution.

We also computed advection with the same initial setting a tree with 32 terminal segments. Due to the more complex structure of this tree, a three-dimensional plot does not intuitively show results, so we present these results in a view from the top using color-coding only. Thickness of the lines here does not correspond to the radii of the segments but is the same for all segments. Some timesteps of this calculation are shown in Figure 4.22.

Again, we can see how the first pulse of temperature is advected through the arterial tree and how energy starts flowing up the venous tree from the terminal segments. In both trees, we can see that velocities decrease on segments of higher generation, in particular that velocities are almost zero on those segments far away from the other tree. On those segments with very small flow velocity, there is almost no inflow of mass, thus their temperature content remains almost unchanged.

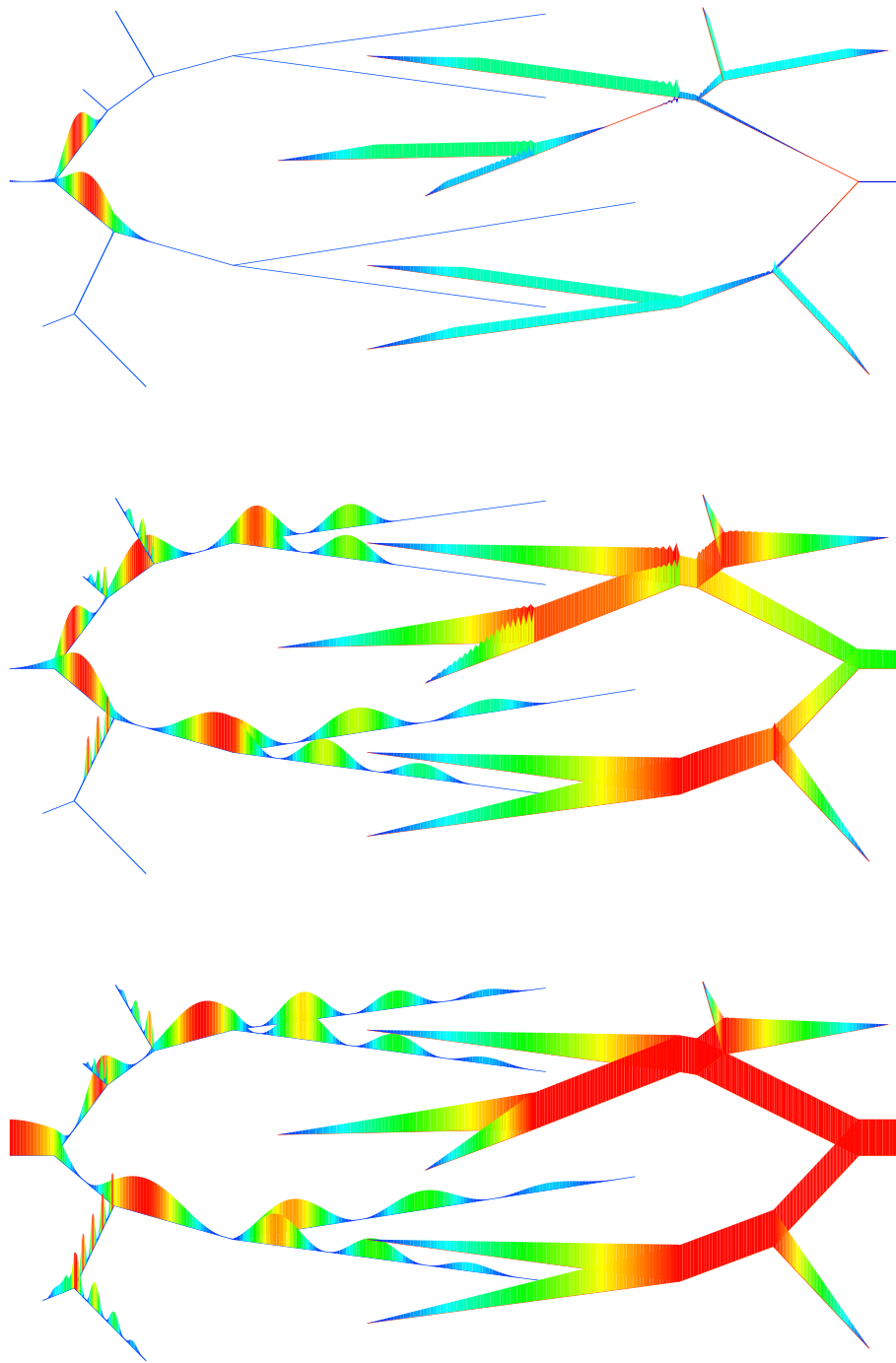


Figure 4.20: Advection on a pair of vessel trees: temperature content profiles after 200, 750 and 1600 time steps. There is no coupling between the two trees (by energy exchange or in another way).

On the arterial tree, the drop-off of temperature content on terminal segments can be observed, similarly on the venous tree, the effect of inflow source terms along terminal segments can be seen. In case of discontinuous flow combination, we obtain upflow oscillations.

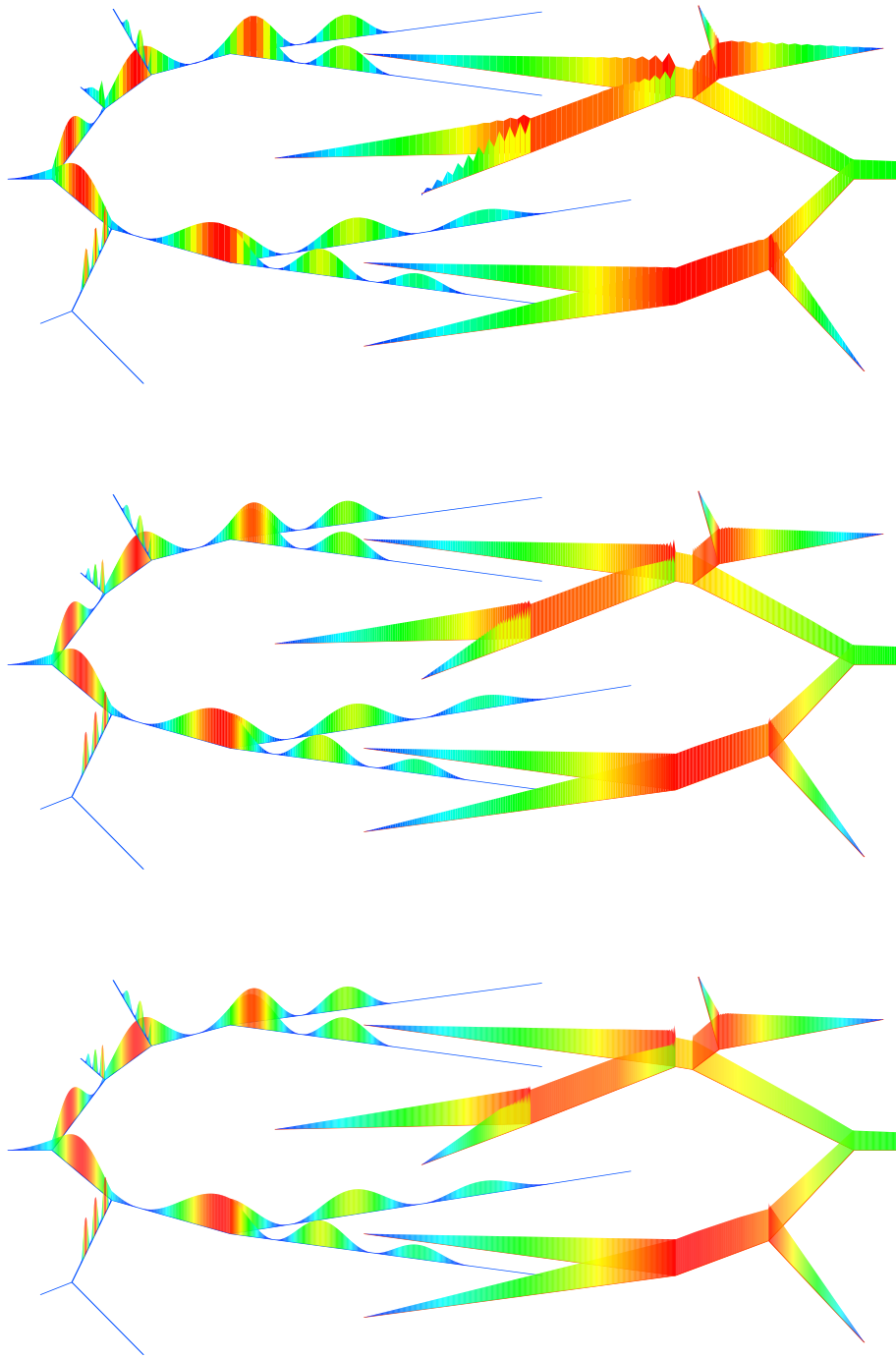


Figure 4.21: Advection on a pair of 8-trees, comparison of different discretizations (grid levels). Compare these profiles to second tree in Figure 4.20. There is no coupling between the two trees.

On the upper arterial tree, discretization is not fine enough to resolve some high frequency oscillations. On the venous trees, we can see that upflow oscillations in case of discontinuous flow combination cannot be reduced in amplitude by finer discretization.

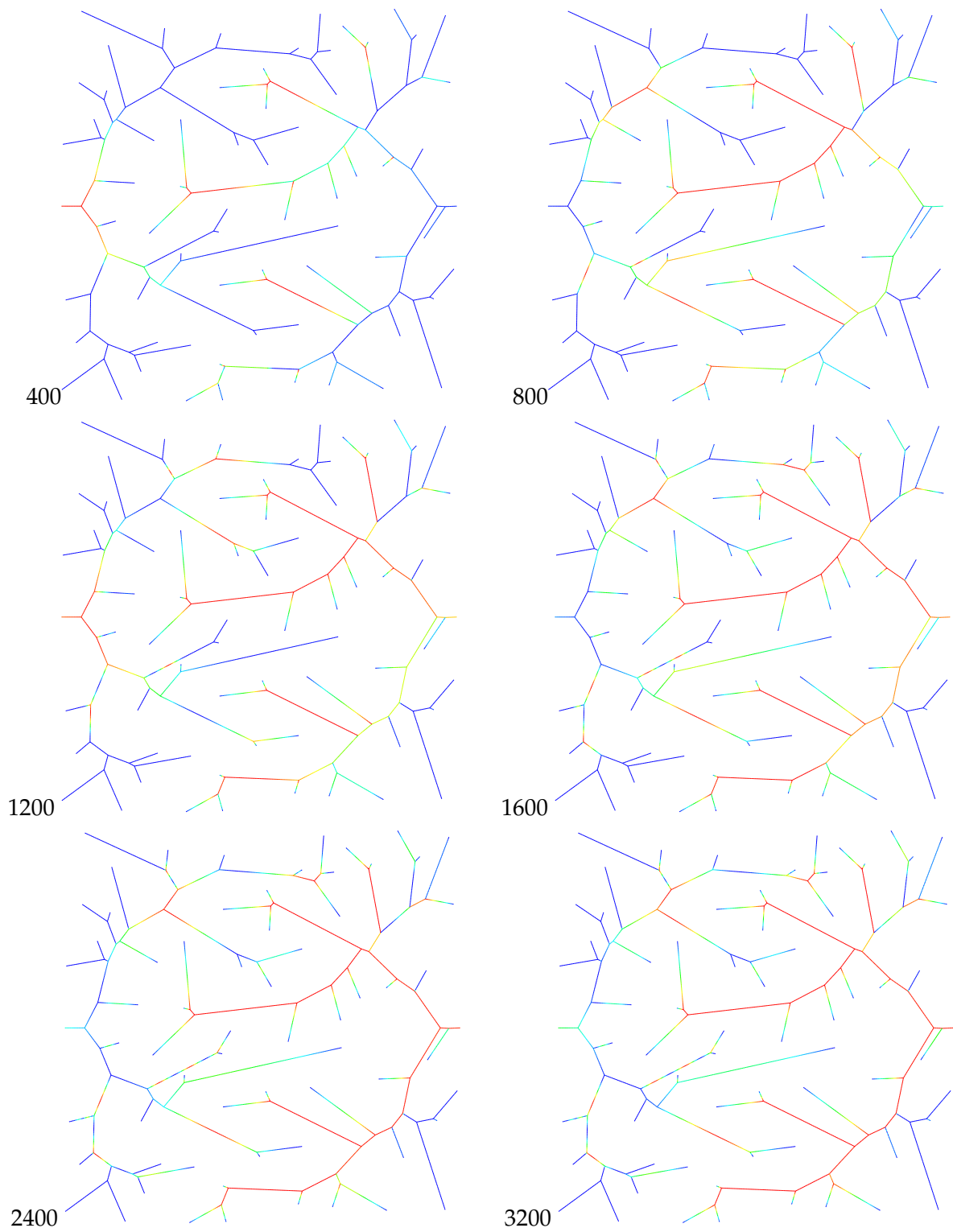


Figure 4.22: Temperature content profiles at time steps 400, 800, 1200, 1600, 2400, 3200 for advection on pairs of 32-trees, color-coded temperature content times cross section area. There is no coupling between the two trees. This shows the same as the two three-dimensional plots before, but now seen from the top so that temperature content information is only encoded in color, not height.

# 5 Coupling Transport and Diffusion

After having treated heat diffusion in the tissue and advection in the two vessel trees as separate problems, we can now couple the two problems by modeling an exchange of heat between tissue and vessels.

Throughout this chapter,  $x$  is used as the variable in 2D tissue whereas  $\xi$  is the variable for 1D representations of trees.

We use  $A_{\emptyset,j}$  for the cross section area of a segment  $j$ , but also  $A_{\emptyset}(\xi) = A_{\emptyset,j} \forall \xi \in [jK, jK + \ell]$ . Indices art and ven are added to distinguish between the two vessel trees whenever necessary.

## 5.1 Problem Formulation

### 5.1.1 Energy Transfer

Let  $C_{\text{ves}}$  be the specific heat capacity of the vessels (equal for arterial and venous vessels), similarly  $\rho_{\text{ves}}$  their density,  $C_{\text{tis}}, \rho_{\text{tis}}$  specific heat capacity and density of the tissue.

For an exchange of energy by heat conduction to occur, there needs to be a temperature gradient. Recall how temperatures are computed from our quantities: In the tissue, we consider an energy density  $u_{\text{tis}}(x)$ , so temperature  $\vartheta_{\text{tis}}$  is

$$\vartheta_{\text{tis}}(x) = u_{\text{tis}}(x) \cdot \frac{1}{C_{\text{tis}}\rho_{\text{tis}}}$$

whereas in the vessels, we consider an energy content  $u_{\text{ves}}(\xi)$  and temperature  $\vartheta_{\text{ves}}$  is (see the beginning of Chapter 4 and equations (4.48) and (4.52)):

$$\vartheta_{\text{ves}}(\xi) = u_{\text{ves}}(\xi) \cdot \frac{1}{C_{\text{ves}}\rho_{\text{ves}}} \cdot \begin{cases} \frac{1}{A_{\emptyset, \{\text{art}, \text{ven}\}, j}} & \text{on non-terminal segment } j \\ \frac{1}{A_{\emptyset, \text{art}, j} \cdot \left(1 - \frac{\xi - jK}{\ell_j}\right)} & \text{on terminal segment } j \text{ of the arterial tree} \\ \frac{1}{A_{\emptyset, \text{ven}, j} \cdot \left(\frac{\xi - jK}{\ell_j}\right)} & \text{on terminal segment } j \text{ of the venous tree} \end{cases}$$

$$= u_{\text{ves}}(\xi) \cdot \frac{1}{C_{\text{ves}}\rho_{\text{ves}}} \cdot \begin{cases} \frac{1}{A_{\emptyset, \{\text{art}, \text{ven}\}, j}} & \text{on non-terminal segment } j \\ \frac{1}{A_{\emptyset, \text{art}, j} \cdot \left(\frac{jK + \ell_j - \xi}{\ell_j}\right)} & \text{on terminal segment } j \text{ of the arterial tree} \\ \frac{1}{A_{\emptyset, \text{ven}, j} \cdot \left(\frac{\xi - jK}{\ell_j}\right)} & \text{on terminal segment } j \text{ of the venous tree.} \end{cases}$$

### Non-Terminal Segments

For the non-terminal segments of the vessel trees, we model a transfer of energy between one-dimensional vessel segments and the two-dimensional tissue. The flow is assumed perpendicular to the vessel segments, but as they are 1D line segments, the notion of heat

conductivity in the usual sense of  $\frac{\text{power}}{\text{temperature difference} \cdot \text{length}}$  needs to be adapted for our purpose.

The energy flow is proportional to the temperature difference between blood vessel and surrounding tissue, it must satisfy energy conservation, and it must be taken into account that we do not get equal temperature instantaneously at one point in a vessel and the tissue at that position. For this purpose, we consider a *heat transmittivity* and consider a heat transmittivity coefficient  $\kappa_{\text{trans}}$  in units  $\frac{\text{W}}{\text{K} \cdot \text{Vol}}$ .  $\kappa_{\text{trans}}$  is the heating of the tissue divided by local temperature difference (between vessels and tissue) per unit volume.

The temperature difference at a point  $\xi$  in a non-terminal segment of one of the trees and the corresponding point in the tissue  $x = \psi(\xi)$  is:

$$\vartheta_{\text{diff}} := \frac{u_{\text{ves}}(\xi)}{A_{\emptyset} \cdot C_{\text{ves}} \rho_{\text{ves}}} - \frac{u_{\text{tis}}(x)}{C_{\text{tis}} \rho_{\text{tis}}}$$

where  $C$  are the specific heat capacities and  $\rho$  are the densities of vessel and tissue respectively.

Then source terms  $f_{\text{ves,w}}(\xi)$  in units of energy content per time (power per length) for the vessels and source terms  $f_{\text{tis,w}}$  in units of energy density per time (power density) are of the form

$$\begin{aligned} f_{\text{ves,w}}(\xi) &= A_{\emptyset}(\xi) \cdot \kappa_{\text{trans}} \cdot (-\vartheta_{\text{diff}}(\xi)) \\ f_{\text{tis,w}}(x) &= \kappa_{\text{trans}} \cdot \vartheta_{\text{diff}}(x). \end{aligned}$$

Writing these in more detail and including time dependence, the mutual source terms for the arterial and venous non-terminal vessel segments are

$$\begin{aligned} f_{\text{art,w}} &: [0, T] \times T_a \rightarrow \mathbb{R} \\ f_{\text{art,w}}(t, \xi) &= A_{\emptyset, \text{art}}(\xi) \cdot \kappa_{\text{trans}} \left[ \frac{u_{\text{tis}}(t, \psi_{\text{art}}^{-1}(\xi))}{C_{\text{tis}} \rho_{\text{tis}}} - \frac{u_{\text{art}}(t, \xi)}{A_{\emptyset, \text{art}}(\xi) \cdot C_{\text{ves}} \rho_{\text{ves}}} \right] \end{aligned} \quad (5.1)$$

$$\begin{aligned} f_{\text{ven,w}} &: [0, T] \times T_v \rightarrow \mathbb{R} \\ f_{\text{ven,w}}(t, \xi) &= A_{\emptyset, \text{ven}}(\xi) \cdot \kappa_{\text{trans}} \left[ \frac{u_{\text{tis}}(t, \psi_{\text{ven}}^{-1}(\xi))}{C_{\text{tis}} \rho_{\text{tis}}} - \frac{u_{\text{ven}}(t, \xi)}{A_{\emptyset, \text{ven}}(\xi) \cdot C_{\text{ves}} \rho_{\text{ves}}} \right], \end{aligned} \quad (5.2)$$

and for the tissue, the source term is

$$\begin{aligned} f_{\text{tis,w}} &: [0, T] \times \Omega \rightarrow \mathbb{R} \\ f_{\text{tis,w}}(t, x) &= \begin{cases} f_{\text{tis,art,w}}(t, x) & \text{if } x \in \text{non-term. segm. of } T_a \\ f_{\text{tis,ven,w}}(t, x) & \text{if } x \in \text{non-term. segm. of } T_v \\ 0 & \text{else} \end{cases} \\ &= \begin{cases} \frac{-1}{A_{\emptyset, \text{art}}(\psi_{\text{art}}(x))} \cdot f_{\text{art,w}}(t, \psi_{\text{art}}(x)) & \text{if } x \in \text{non-term. segm. of } T_a \\ \frac{-1}{A_{\emptyset, \text{ven}}(\psi_{\text{ven}}(x))} \cdot f_{\text{ven,w}}(t, \psi_{\text{ven}}(x)) & \text{if } x \in \text{non-term. segm. of } T_v \\ 0 & \text{else.} \end{cases} \end{aligned} \quad (5.3)$$

## Terminal Segments

For terminal segments, we have outflow and inflow of blood as described in Section 4.4.1. The effect on the energy content of terminal segments by this outflow and inflow was expressed as source terms for the vessels, see equations (4.49) and (4.53):

$$f_{\text{art},f} : [0, T] \times T_a \rightarrow \mathbb{R}$$

$$f_{\text{art},f}(t, \xi) = -v_{\text{art},j} \cdot \frac{u_{\text{art}}(t, \xi)}{jK_{\text{art}} + \ell_{\text{art},j} - \xi} \quad (5.4)$$

$$f_{\text{ven},f} : [0, T] \times T_v \rightarrow \mathbb{R}$$

$$f_{\text{ven},f}(t, \xi) = \frac{A_{\emptyset, \text{ven}, j} v_j}{\ell_{\text{ven}, j}} \cdot u_{\text{tis}}(t, \psi_{\text{ven}}^{-1}(\xi)). \quad (5.5)$$

As we do not model advection in the tissue, we cannot simply take the sink terms for the tissue corresponding to those source terms on the vessels. If we would do this, we would replace a source of mass and energy by a source of energy only. Then the physically stationary state (constant temperature in the whole system, i. e. in tissue and all vessels) would not be a stationary state in our model.

Instead, we microscopically inspect what we model as outflow segments: In the arterial tree, blood flows from arterial vessels into fine capillaries and tissue that already contain blood at a certain temperature. Heating and cooling, i. e. energy sources for the tissue, are only effective if there is a difference between inflowing and existing temperature. In the venous tree, blood flows from fine capillaries and tissue into venous vessels. Due to the opposite flow direction (there is no mass flowing in from the outside), this has no heating or cooling effect for the tissue.

We obtain source terms  $f_{\text{tis}, \text{art}, f}$  and  $f_{\text{tis}, \text{ven}, f}$  in units of energy density per time (power density) for the tissue that are of the form:

$$f_{\text{tis}, \text{art}, f}(x) = C_{\text{tis}} \rho_{\text{tis}} \cdot \frac{v}{\ell} \cdot \vartheta_{\text{diff}}(x)$$

$$f_{\text{tis}, \text{ven}, f}(x) = 0$$

where, for terminal segments, we need to use the apparent cross section area for computing temperature (see Section 4.4.1)

$$\vartheta_{\text{diff}} := \frac{u_{\text{ves}}(\xi)}{A_{\emptyset} \cdot \frac{\ell_j + jK - \psi_{\text{art}}(x)}{\ell_j} \cdot C_{\text{ves}} \rho_{\text{ves}}} - \frac{u_{\text{tis}}(x)}{C_{\text{tis}} \rho_{\text{tis}}}.$$

Writing this in more detail with correct velocity and length, and adding time dependence,

the mutual source terms for the tissue are

$$\begin{aligned}
 f_{\text{tis},f} &: [0, T] \times \Omega \rightarrow \mathbb{R} \\
 f_{\text{tis},f}(t, x) &= \begin{cases} f_{\text{tis,art},f}(t, x) & \text{if } x \in \text{non-term. segm. of } T_a \\ f_{\text{tis,ven},f}(t, x) & \text{if } x \in \text{non-term. segm. of } T_v \\ 0 & \text{else} \end{cases} \quad (5.6) \\
 &= \begin{cases} C_{\text{tis}}\rho_{\text{tis}} \frac{v_{\text{art},j}}{\ell_{\text{art},j}} \cdot \left[ \frac{u_{\text{art}}(t, \psi_{\text{art}}(x))}{A_{\mathcal{O},\text{art},j} \cdot \left( \frac{\ell_j + jK - \psi_{\text{art}}(x)}{\ell_j} \right) \cdot C_{\text{ves}}\rho_{\text{ves}}} - \frac{u_{\text{tis}}(t, x)}{C_{\text{tis}}\rho_{\text{tis}}} \right] & \text{if } x \in \text{term. segm. } j \text{ of } T_a \\ 0 & \text{if } x \in \text{term. segm. of } T_v \\ 0 & \text{else.} \end{cases}
 \end{aligned}$$

In particular, this means that we do not model heat diffusion (transmission) between tissue and venous terminal segments.

### 5.1.2 Coupled Problems

#### Advection in the Arterial Tree

Advection in the arterial tree as a one-dimensional problem with flow velocities  $v_{\text{art}}(\xi) = v_j$  being constant on each segment  $j$ , boundary values  $u_{\text{a,root}}(t)$  at the root and initial profile  $u_{\text{art},0}(\xi)$  is modeled by

$$\begin{aligned}
 \partial_t u_{\text{art}}(t, \xi) + v_{\text{art}}(\xi) \cdot \partial_{\xi} u_{\text{art}}(t, \xi) &= f_{\text{art}}(t, \xi) \quad \text{in } [0, T] \times T_a \\
 u_{\text{art}}(t, 0) &= u_{\text{a,root}}(t) \quad \text{in } [0, T] \\
 u_{\text{art}}(0, \xi) &= u_{\text{art},0}(\xi) \quad \text{in } T_a.
 \end{aligned} \quad (5.7)$$

The source term  $f_{\text{art}}$  has the form

$$\begin{aligned}
 f_{\text{art}}(t, \xi) &= \begin{cases} f_{\text{art,w}}(t, \xi) & \text{on non-terminal segments} \\ f_{\text{art,f}}(t, \xi) & \text{on terminal segments} \end{cases} \quad (5.8) \\
 &= \begin{cases} A_{\mathcal{O},\text{art},j} \cdot \kappa_{\text{trans}} \cdot \left[ \frac{u_{\text{tis}}(t, \psi_{\text{art}}^{-1}(\xi))}{C_{\text{tis}}\rho_{\text{tis}}} - \frac{u_{\text{art}}(t, \xi)}{A_{\mathcal{O},\text{art},j} \cdot C_{\text{ves}}\rho_{\text{ves}}} \right] & \text{on non-terminal segments } j \\ -v_{\text{art},j} \frac{u_{\text{art}}(t, \xi)}{jK_{\text{art}} + \ell_{\text{art},j} - \xi} & \text{on terminal segments } j. \end{cases}
 \end{aligned}$$

#### Advection in the Venous Tree

Advection in the venous tree as a one-dimensional problem with flow velocities  $v_{\text{ven}}(\xi) = v_j$  being constant on each segment  $j$ , zero boundary values at the leaf nodes and initial profile  $u_{\text{ven},0}(\xi)$  is modeled by

$$\begin{aligned}
 \partial_t u_{\text{ven}}(t, \xi) + v(\xi) \cdot \partial_{\xi} u_{\text{ven}}(t, \xi) &= f_{\text{ven}}(t, \xi) \quad \text{in } [0, T] \times T_v \\
 u_{\text{ven}}(t, K \cdot l) &= 0 \quad \text{in } [0, T], \forall l \text{ leaf node} \\
 u_{\text{ven}}(0, \xi) &= u_{\text{ven},0}(\xi) \quad \text{in } T_v.
 \end{aligned} \quad (5.9)$$

The source term  $f_{\text{ven}}$  has the form

$$\begin{aligned}
 f_{\text{ven}}(t, \xi) &= \begin{cases} f_{\text{ven,w}}(t, \xi) & \text{on non-terminal segments} \\ f_{\text{ven,f}}(t, \xi) & \text{on terminal segments} \end{cases} & (5.10) \\
 &= \begin{cases} A_{\emptyset, \text{ven}, j} \cdot \kappa_{\text{trans}} \cdot \left[ \frac{u_{\text{tis}}(t, \psi_{\text{ven}}^{-1}(\xi))}{C_{\text{tis}} \rho_{\text{tis}}} - \frac{u_{\text{ven}}(t, \xi)}{A_{\emptyset, \text{ven}, j} \cdot C_{\text{ves}} \rho_{\text{ves}}} \right] & \text{on non-terminal segments } j \\ \frac{A_{\emptyset, \text{ven}, j} v_j}{\ell_{\text{ven}, j}} \cdot u_{\text{tis}}(t, \psi_{\text{ven}}^{-1}(\xi)) & \text{on terminal segments } j. \end{cases}
 \end{aligned}$$

### Heat Diffusion in Tissue

Isotropic heat conduction with constant heat conduction coefficient  $\kappa$ , zero Neumann boundary values and initial data  $u_{\text{tis},0}$  is modeled by

$$\begin{aligned}
 \partial_t u_{\text{tis}}(t, x) - \kappa \cdot \Delta_x u_{\text{tis}}(t, x) &= f_{\text{tis}}(t, x) + f_{\text{probe}}(t, x) & \text{in } [0, T] \times \Omega \\
 \partial_\nu u_{\text{tis}}(t, x) &= 0 & \text{in } [0, T] \times \partial\Omega \\
 u_{\text{tis}}(0, x) &= u_{\text{tis},0}(x) & \text{in } \Omega
 \end{aligned} \tag{5.11}$$

where  $f_{\text{probe}}$  is an  $L^2(\Omega)$  source describing heating by the probe whereas  $f_{\text{tis}}(t, \cdot) \in H^{-1}(\Omega)$  is meant in a distributional sense as in equation (3.4):

$$\int_{\Omega} (\partial_t u_{\text{tis}}(t, x) - \kappa \cdot \Delta_x u_{\text{tis}}(t, x)) \varphi(x) \, dx = \int_{T_a \cup T_v} f_{\text{tis}}(t, x) \varphi(x) \, d\gamma + \int_{\Omega} f_{\text{probe}}(t, x) \varphi(x) \, dx$$

for test functions  $\varphi$  where, again,  $dx$  is integration in 2D whereas  $d\gamma$  denotes integration along 1D line segments in 2D.

$f_{\text{tis}}$  has the form:

$$\begin{aligned}
 &f_{\text{tis}}(t, x) \\
 &= \begin{cases} f_{\text{tis,art,w}}(t, x) & x \in \text{non-term. segm. } j \text{ of } T_a \\ f_{\text{tis,art,f}}(t, x) & x \in \text{term. segm. } j \text{ of } T_a \\ f_{\text{tis,ven,w}}(t, x) & x \in \text{non-term. segm. } j \text{ of } T_v \\ f_{\text{tis,ven,f}}(t, x) & x \in \text{term. segm. } j \text{ of } T_v \\ 0 & \text{else} \end{cases} \\
 &= \begin{cases} \frac{-1}{A_{\emptyset, \text{art}, j}} \cdot f_{\text{art,w}}(t, \psi_{\text{art}}(x)) & x \in \text{non-term. segm. } j \text{ of } T_a \\ C_{\text{tis}} \rho_{\text{tis}} \cdot \frac{v_{\text{art}, j}}{\ell_{\text{art}, j}} \cdot \left[ \frac{u_{\text{art}}(t, \psi_{\text{art}}(x))}{A_{\emptyset, \text{art}, j} \cdot \left( \frac{\ell_{j+JK} - \psi_{\text{art}}(x)}{\ell_j} \right) \cdot C_{\text{ves}} \rho_{\text{ves}}} - \frac{u_{\text{tis}}(t, x)}{C_{\text{tis}} \rho_{\text{tis}}} \right] & x \in \text{term. segm. } j \text{ of } T_a \\ \frac{-1}{A_{\emptyset, \text{ven}, j}} \cdot f_{\text{ven,w}}(t, \psi_{\text{ven}}(x)) & x \in \text{non-term. segm. } j \text{ of } T_v \\ 0 & x \in \text{term. segm. } j \text{ of } T_v \\ 0 & \text{else} \end{cases}
 \end{aligned}$$

$$= \begin{cases} \kappa_{\text{trans}} \cdot \left[ \frac{u_{\text{art}}(t, \psi_{\text{art}}(x))}{A_{\mathcal{O}, \text{art}, j} \cdot C_{\text{ves}} \rho_{\text{ves}}} - \frac{u_{\text{tis}}(t, x)}{C_{\text{tis}} \rho_{\text{tis}}} \right] & x \in \text{non-term. segm. } j \text{ of } T_a \\ C_{\text{tis}} \rho_{\text{tis}} \cdot \frac{v_{\text{art}, j}}{\ell_{\text{art}, j}} \cdot \left[ \frac{u_{\text{art}}(t, \psi_{\text{art}}(x))}{A_{\mathcal{O}, \text{art}, j} \cdot \left( \frac{\ell_{j+JK} - \psi_{\text{art}}(x)}{\ell_j} \right) \cdot C_{\text{ves}} \rho_{\text{ves}}} - \frac{u_{\text{tis}}(t, x)}{C_{\text{tis}} \rho_{\text{tis}}} \right] & x \in \text{term. segm. } j \text{ of } T_a \\ \kappa_{\text{trans}} \cdot \left[ \frac{u_{\text{ven}}(t, \psi_{\text{art}}(x))}{A_{\mathcal{O}, \text{ven}, j} \cdot C_{\text{ves}} \rho_{\text{ves}}} - \frac{u_{\text{tis}}(t, x)}{C_{\text{tis}} \rho_{\text{tis}}} \right] & x \in \text{non-term. segm. } j \text{ of } T_v \\ 0 & x \in \text{term. segm. } j \text{ of } T_v \\ 0 & \text{else.} \end{cases}$$

*Remark 5.1.1.* Some of the factors here could be canceled, but the form presented here is used for the actual computation.

### Time Step

To avoid numerical artefacts in the advection computation, we may choose the level of the vessel discretization to be greater than the level of the tissue discretization. Since the diffusion in tissue dominates the memory requirement and causes a significant part of the runtime if the discretizations are equally fine, we try to discretize the tissue as coarse as tolerable.

Finally, we get a bound on our time step:  $\tau \leq h_{\text{tis}}$  and  $\tau \cdot v_j \leq h_{\text{ves}, j} \forall j \in T_a \cup T_v$ .

This bound is critical for the advection problem: Advection is treated explicitly, so the time step restriction is necessary for stability. For the diffusion problem that we treat semi-implicitly (explicit sources but implicit computation of diffusion), this time step restriction is necessary for consistency but we would still get stability for a bigger time step. For a more detailed treatment of consistency and stability of time stepping methods, we refer to [19].

This shows that generalizing our ELLAM to  $\rho > 1$  would allow us to refine the discretization of the vessels without being forced to use a smaller time step.

### Mutual Source Terms

For the source terms, we consider three different types of source terms:

- $\bar{F}_{\text{art}}$  and  $\bar{F}_{\text{ven}}$ , the actual sources for the advection problems
- $\tilde{F}_{\text{tis}, \text{art}}$  and  $\tilde{F}_{\text{tis}, \text{ven}}$ , virtual sources on the two vessel trees whose sum corresponds to
- $\bar{F}_{\text{tis}}$ , the actual source terms for the diffusion problem.

In the implementation, we compute

1.  $\bar{F}_{\text{art}, f}$ , discretization of  $f_{\text{art}, f}$  as in equation (4.51), the outflow of energy content out of terminal segments of the arterial tree
2.  $\tilde{F}_{\text{tis}, \text{art}, f}$ , discretization of  $f_{\text{tis}, \text{art}, f}$  as a function on the arterial vessel tree, see equation (5.4), the inflow of energy into tissue (from terminal segments of the arterial tree if there is a temperature difference)
3.  $\bar{F}_{\text{ven}, f}$ , discretization of  $f_{\text{ven}, f}$  as in equation (4.53), the inflow of energy content into terminal segments of the venous tree

4.  $\tilde{F}_{\text{tis,ven},f} = 0$ , discretization of  $f_{\text{tis,art},f} = 0$ , as a function on the venous vessel tree see equation (5.5)
5.  $\bar{F}_{\text{art},w}$ , discretization of  $f_{\text{art},w}$  as in equation (5.1), the diffusive flow of energy content out of non-terminal segments of the arterial tree (into tissue)
6.  $\tilde{F}_{\text{tis,art},w}$ , discretization of  $f_{\text{tis,art},w}$  as a function on the arterial vessel tree, this is simply proportional to  $\bar{F}_{\text{art},w}$ , see equation (5.3)
7.  $\bar{F}_{\text{ven},w}$ , discretization of  $f_{\text{ven},w}$  as in equation (5.2), the diffusive flow of energy content out of non-terminal segments of the venous tree (into tissue)
8.  $\tilde{F}_{\text{tis,ven},w}$ , discretization of  $f_{\text{tis,ven},w}$  as a function on the venous vessel tree, again this is simply proportional to  $\bar{F}_{\text{ven},w}$ , see equation (5.3)

These discrete functions are defined on the whole trees. Then we have:

$$\begin{aligned}\bar{F}_{\text{art}} &= \bar{F}_{\text{art},f} + \bar{F}_{\text{art},w}, \\ \bar{F}_{\text{ven}} &= \bar{F}_{\text{ven},f} + \bar{F}_{\text{ven},w}, \\ \tilde{F}_{\text{tis,art}} &= \tilde{F}_{\text{tis,art},f} + \tilde{F}_{\text{tis,art},w}, \\ \tilde{F}_{\text{tis,ven}} &= \tilde{F}_{\text{tis,ven},f} + \tilde{F}_{\text{tis,ven},w}.\end{aligned}$$

Finally, like in Section 3, the source terms  $\bar{F}_{\text{tis}}$ , a discrete function on the tissue, is computed from  $\tilde{F}_{\text{tis,art}}$  and  $\tilde{F}_{\text{tis,ven}}$ .

The source terms  $\bar{F}_{\text{art},w}$  and  $\bar{F}_{\text{ven},w}$  for the advection problem are set up by looping over all grid cells of all non-terminal segments of both trees and computing the instantaneous energy transfer from the local temperature differences at the beginning of the time step and assuming a constant source during the time step, see Section 4.2.3. Similarly  $\tilde{F}_{\text{tis,art},f}$ , the discretization of  $f_{\text{art},f}$ , is computed from local temperature differences.

The error in this temporal approximation is biased: The temperature difference, thus the energy transfer, decays during the time step, so this numerical approximation considering only the temperature difference at the beginning of the time step tends to overestimate the flow of energy.

## 5.2 Heating by the RF Probe

We use a very simple model for the additional source term for our diffusion problem describing the influence of an RF probe. A more detailed treatment of this heating can be found in [16].

Here,  $f_{\text{probe}}(t, x)$  is set to

$$f_{\text{probe}}(t, x) = \begin{cases} C(\vartheta(t, (x_s, y_s))) \cdot \exp\left(\frac{-1}{1 + \frac{(x-x_s)^2 + (y-y_s)^2}{\sigma^2}}\right) & \text{for } (x - x_s)^2 + (y - y_s)^2 < \sigma^2 \\ 0 & \text{else} \end{cases} \quad (5.12)$$

where  $(x_s, y_s)$  is the position where the source is centered,  $\sigma$  the radius of the domain heated and  $C(\vartheta(t, (x_s, y_s)))$  depends nonlinearly on the average temperature on some neighborhood of  $(x_s, y_s)$ , it is some constant positive value if  $\vartheta(t, (x_s, y_s))$  is smaller than some temperature threshold  $\vartheta_{\text{thres}}$ , otherwise zero.

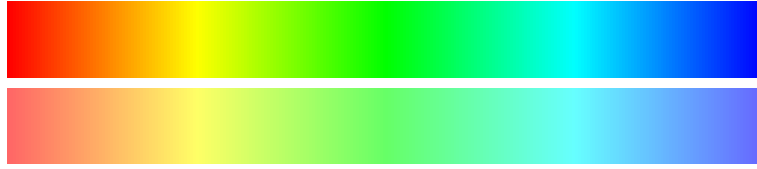


Figure 5.1: The two corresponding color scales used for the plots in this chapter, top: for vessels, bottom: for tissue.

*Remark 5.2.1.*  $f_{\text{probe}}(t, \cdot)$  is a  $C^\infty(\mathbb{R}^2)$  function with compact support.  
 $f_{\text{probe}}|_{[0,1]^2}(t, \cdot)$  is  $C^\infty([0,1]^2)$ .

### 5.3 Implementation and Results

In addition to heat conduction and advection on trees that were implemented before, we now need to find a common time step and deal with the mutual source terms described above.

As our flow velocities may vary throughout the simulation but will always satisfy  $v_j \leq 1$ , our restriction for the time step is:  $\tau \leq h_{\text{ves}}$  and  $\tau \leq h_{\text{ves},j} \forall j \in T_a \cup T_v$ .

A class `tissue_vessel_geometry` was written to store the discrete data on the tissue and on the vessels, it also keeps track of the discretizations and provides functions for computing the mutual source terms.

In each time step of the calculation, we first set up the mutual source terms, then compute one time step of diffusion and one time step of advection. Both methods are *explicit*, no source term of one problem depends on the new time step of the other problem, so the order in which the two time steps are computed does not matter and we could compute them in parallel.

The output shown is a superposition of the tissue temperature and the vessel temperature where the tissue is shown with an opacity of 60 %. The corresponding color scales are shown in Figure 5.1. The combined plots were generated from the tissue temperature plots (ppm bitmap graphics) and vessel temperature plots (eps vector graphics) written out by our program, converting these to ppm images of the same size and finally producing a composite image using `pnmcomp` and an appropriate alpha mask.

Note that we now plot temperature for the vessels, not energy content as in Chapter 4.

#### 5.3.1 Limitations of our Model

Two significant limitations of our model are shown in Figure 5.2:

- If segments lie perpendicular to a temperature gradient (left of the probe), we observe artificial cooling (or heating).

The temperature difference between the vessel and warmer surrounding tissue leads to an energy source for the vessel and a sink for the tissue. This sink acts isotropically on the tissue and finite element basis functions on both sides of the vessel segment are involved which causes this effect.

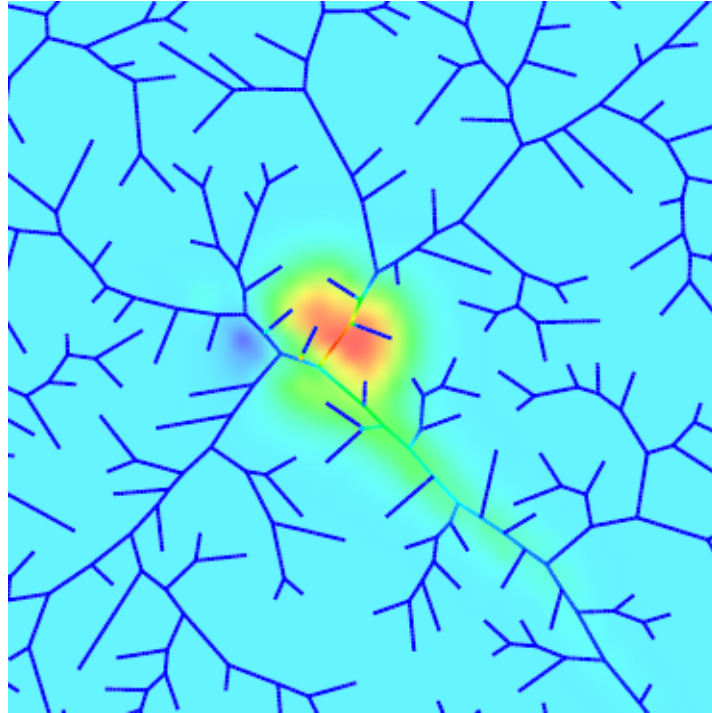


Figure 5.2: An RF probe placed near the venous vessel tree: Vessel temperatures from 0 (blue) to 1 (red), tissue temperatures from  $-0.3$  (blue) to 1 (red) showing two limitations of our model

- The terminal segments lying close to the probe only show nonzero temperature at their downflow end.

Due to their very low flow velocity, they accumulate mass and temperature very slowly. The temperature in the last grid cell of one of these terminal segments is computed using a basis function of its parent segment, this explains the jump of temperature at the end.

Also due to the low flow velocity, their influence on the parent segment is small, so the discontinuity does not cause significant numerical artefacts.

Potentially, very short segments may create other numerical artefacts because they are discretized with grids of only few grid points. This problem was not observed in the computations of this chapter.

A future extension of our model will have to deal with these problems.

When showing the results of some simulations in the next subsection, we restrict the temperature intervals to  $[0, 1]$  and we only plot vessel segments with flow velocity bigger than some threshold so that the problems described here are not visible.

### 5.3.2 Results

We present results of simulations of different scenarios:

1. a pulse of warm blood flowing into our system through the arterial tree

2. pulses of warm blood flowing in with pulsed flow velocities
3. a probe located near one branch of the arterial vessels with constant inflow temperature and constant velocities
4. a probe located in the center of the domain
5. a probe located near the venous vessel tree

where we use the pair of vessel trees with 512 terminal segments each and velocities shown in Figure 2.11.

We discretize the tissue with a grid of level 7 ( $129 \times 129$ ) and the vessels with grids of level 9 (grid spacings  $\leq 1/512$ ). The time step is  $\tau \approx 0.00166727 \approx \frac{1}{599.784}$ .

### Inflowing Warm Blood, Constant Velocities

In this simulation, we start with zero initial temperature of our system (tissue and vessels) and let set the inflow condition of the arterial tree,  $u_{\text{root}}(t)$  such that the corresponding temperature is

$$\theta_{\text{root}}(t) = \begin{cases} \frac{1 - \cos\left(\frac{2\pi t}{200\tau}\right)}{2} & \text{for } t \in [0, 200\tau] \\ 0 & \text{else.} \end{cases}$$

This is a  $C^{1,1}$  function of  $t$ , i. e.  $\theta_{\text{root}} \in C^1 \wedge \theta'_{\text{root}} \in C^{0,1}$ .

Heat transmittivity  $\kappa_{\text{trans}}$  and heat conduction coefficient  $\kappa$  were set to reasonable values such that there is still a significant temperature difference between blood reaching terminal segments and the surrounding tissue and such that energy transport by diffusion is slower than energy transport by advection.

Figures 5.3 and 5.4 show some time steps of this simulation. The vessel structures are thin, so the thermal impact of the temperature difference between vessels and tissue is small. In our setting, the maximal temperature in the tissue is about three orders of magnitude smaller than the maximal temperature in the vessels. To produce a combined plot anyway, we use two different color scales. Temperature in the vessels ranges from 0 (blue) to 1 (red), temperature in the tissue ranges from 0 (blue) to 0.00125 (red).

We can see that the volume of warm blood is advected through our vessel system, being split at bifurcations. Heat is transmitted from the vessels into surrounding tissue, leading to a slow decrease in temperature in the vessels and to a heating of the tissue near the vessel.

Near bifurcations, there are more than one segment heating certain parts of the tissue, in these locations we observe stronger heating than away from bifurcations. Moreover, heating is stronger at those segments with lower flow velocities.

At bifurcations where one daughter segment has a very small flow velocity (flow splitting ratio close to zero), we observe almost no influence of the volume of warm blood passing that bifurcation. Only very little warm blood enters this daughter and due to the small flow velocity, heat transmission out of the segment dominates.

### Inflowing Warm Blood, Pulsed Velocities

The next simulation assumes that there are several pulses of warm blood flowing in while all flow velocities  $v_j$  change periodically:

$$\theta_{\text{root}}(t) = \begin{cases} \frac{1 - \cos\left(\frac{2\pi t}{1000\tau}\right)}{2} & \text{for } t \in \bigcup_{k \in \{0,1,2,3,4\}} [4000\tau k, 4000\tau k + 1000\tau] \\ 0 & \text{else} \end{cases}$$

$$v_j(t) = v_j \cdot \left(0.6 + 0.4 \cos\left(\frac{2\pi t}{1000\tau}\right)\right).$$

Again, we show timesteps in Figures 5.5 and 5.6 using two different color scales, temperature in the vessels ranges from 0 (blue) to 1 (red), temperature in the tissue ranges from 0 (blue) to 0.0286 (red). The time steps shown here are the second volume of warm blood flowing in and span almost three pulsations of velocity.

Similar effects as for the simulation before can be observed, additionally, the flow velocities vary periodically.

Each time new warm blood flows into our system, thermal energy is added. Heat diffusion leads to a relatively uniform temperature in the center of the domain after one volume of warm blood has been advected through the vessel system and before the next one arrives.

Due to the different color scales, we cannot see how the venous tree is influenced by the rise of temperature in the domain, but after 30000 time steps it can be observed that the tissue becomes warmer near the root of the venous vessel tree but not in the top-right and bottom-right corner of the domain.

Pulsation is visible better if all images produced in this simulation are combined to an mpeg video clip. This and video clips for the other simulations will be available on the INS website, see below.

### Probe near the Arterial Tree

As a further scenario, we start in zero initial state and place a probe source near one branch of the arterial tree. Inflow temperature into our system is zero and flow velocities are kept constant. Except for the probe source term, our system is linear (and for probe source, we only need to shift the temperature threshold), so this corresponds to body temperature as initial state and blood of body temperature flowing in while an RF probe is being used.

Results are shown in Figure 5.7 where we can now use the same color scale for both tissue and vessels: temperatures range from 0 (blue) to 1 (red). We only plotted those vessel segments with flow velocity greater than a threshold (0.0005).

Here, we can see that the blood flowing through the vessel near the probe is heated by heat transmission from the tissue and the tissue near the vessel is cooled correspondingly. Heat is transported through part of the arterial tree and we can see how the tissue near that part is affected as well.

Heat diffuses through the tissue and reaches the venous vessel tree after a while. It is advected through the venous tree, also transmitted to tissue near the arterial tree and finally, we can also observe an increasing temperature of the blood flowing out of our system (through the root segment of the venous tree).

### **Probe in the Center**

Next, we use the same scenario as before but move the probe to the center of our domain where both arterial and venous vessel tree are present. Again, we use combined tissue-vessel plots with the same color scales for both tissue and vessels and only plot vessel segments with flow velocity greater than 0.0005: see Figure 5.8.

Now the flow through the arterial vessel tree leads to some cooling of the tissue heated by the probe, also heat is advected further through the arterial vessel tree.

The venous vessel tree is affected immediately by the rising temperature and advects heat towards its root segment, also transmitting energy to its surrounding tissue.

### **Probe near the Venous Tree**

Finally, we place the probe near the venous tree. Again, we use combined tissue-vessel plots with the same color scales, do not plot vessel segments with very small flow velocities and show results of this computation in Figure 5.9.

Again, venous vessel segments near the probe are heated (as energy is transmitted from the tissue to the vessels), heat is advected through the venous vessel tree, heating the surrounding tissue of the downflow segments.

Even though we have clipped temperature to  $[0, 1]$ , the artificial cooling effect mentioned above in Section 5.3.1 can be observed opposite venous vessels near the location of the probe.

The venous vessel tree is relatively far away from the source so that no effect of or on the arterial vessels is visible in the output.

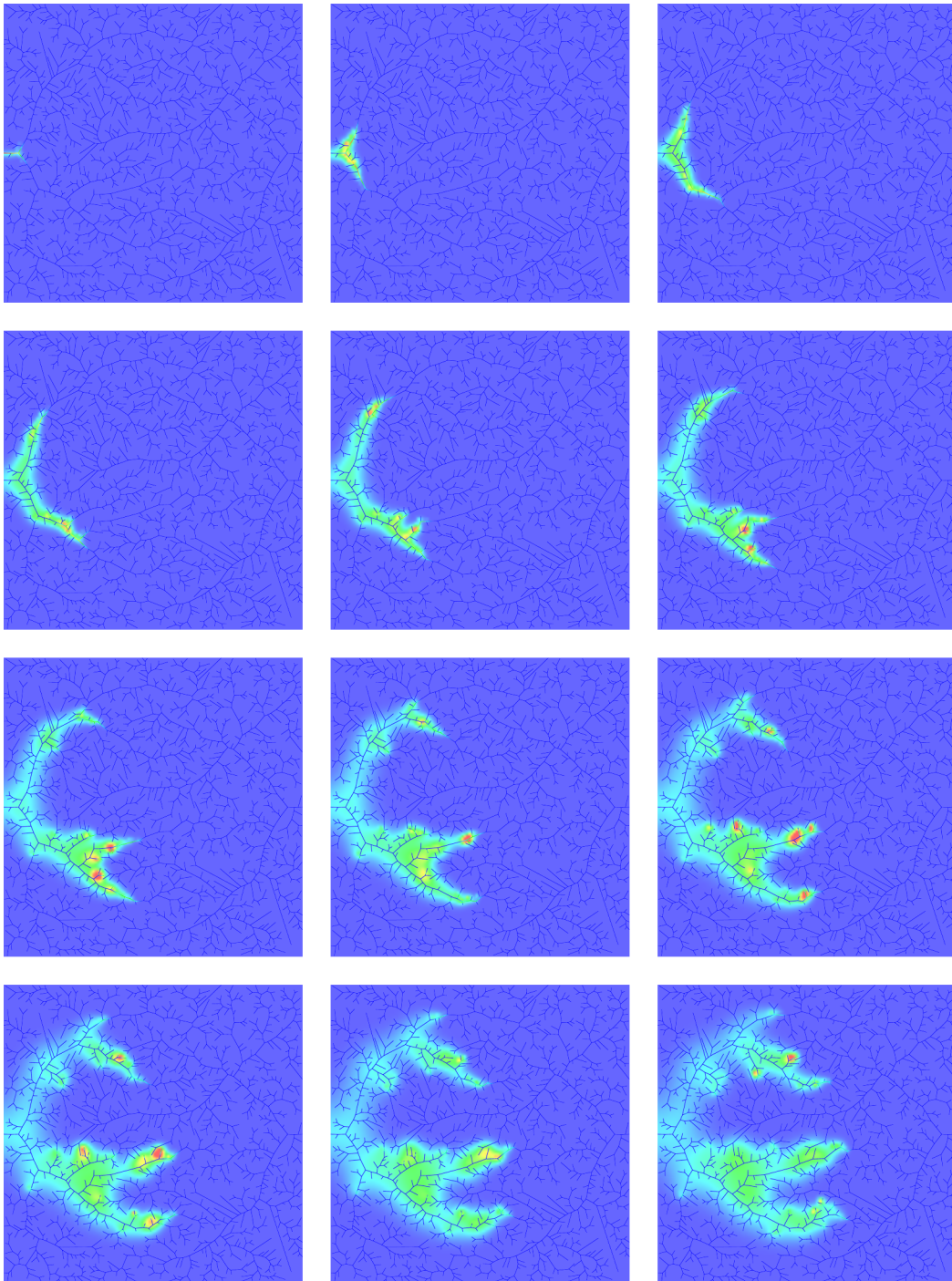


Figure 5.3: Advection-diffusion for inflowing warm blood (constant velocities) on a 1024-tree: Time steps 100, 200,  $\dots$ , 1100, 1200. These combined plots show temperature in the vessels and temperature in the tissue on two different color scales.

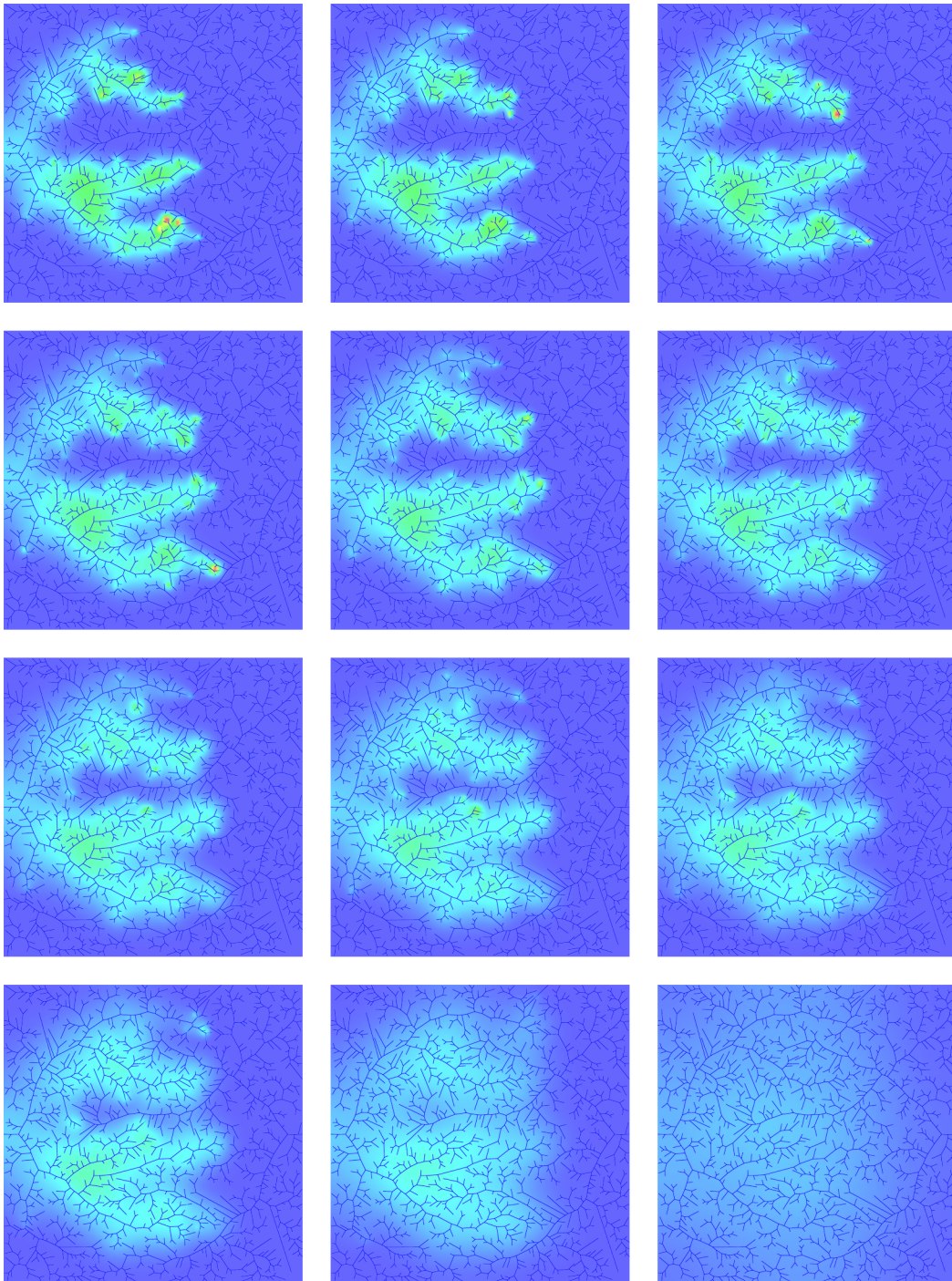


Figure 5.4: Advection-diffusion for inflowing warm blood (constant velocities) on a 1024-tree: Time steps 1300, 1400, . . . , 2100, 2200, 3000, 10000. These combined plots show temperature in the vessels and temperature in the tissue on two different color scales.

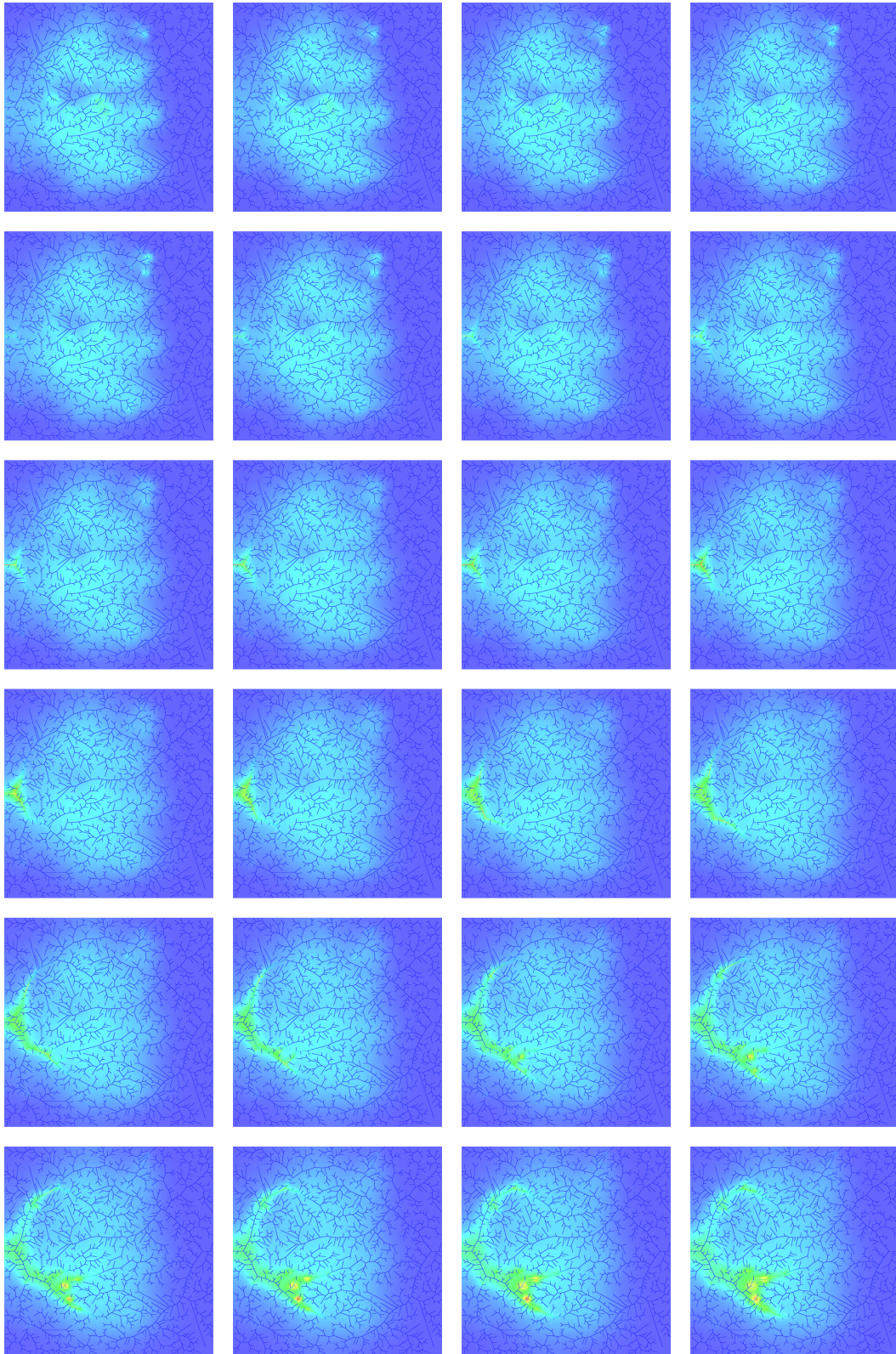


Figure 5.5: Advection-diffusion with pulsed inflow and pulsed velocities on a 1024-tree:  
 Time steps 4000, 4060, . . . , 5320, 5380.  
 These combined plots show temperature in the vessels and temperature in the  
 tissue on two different color scales.

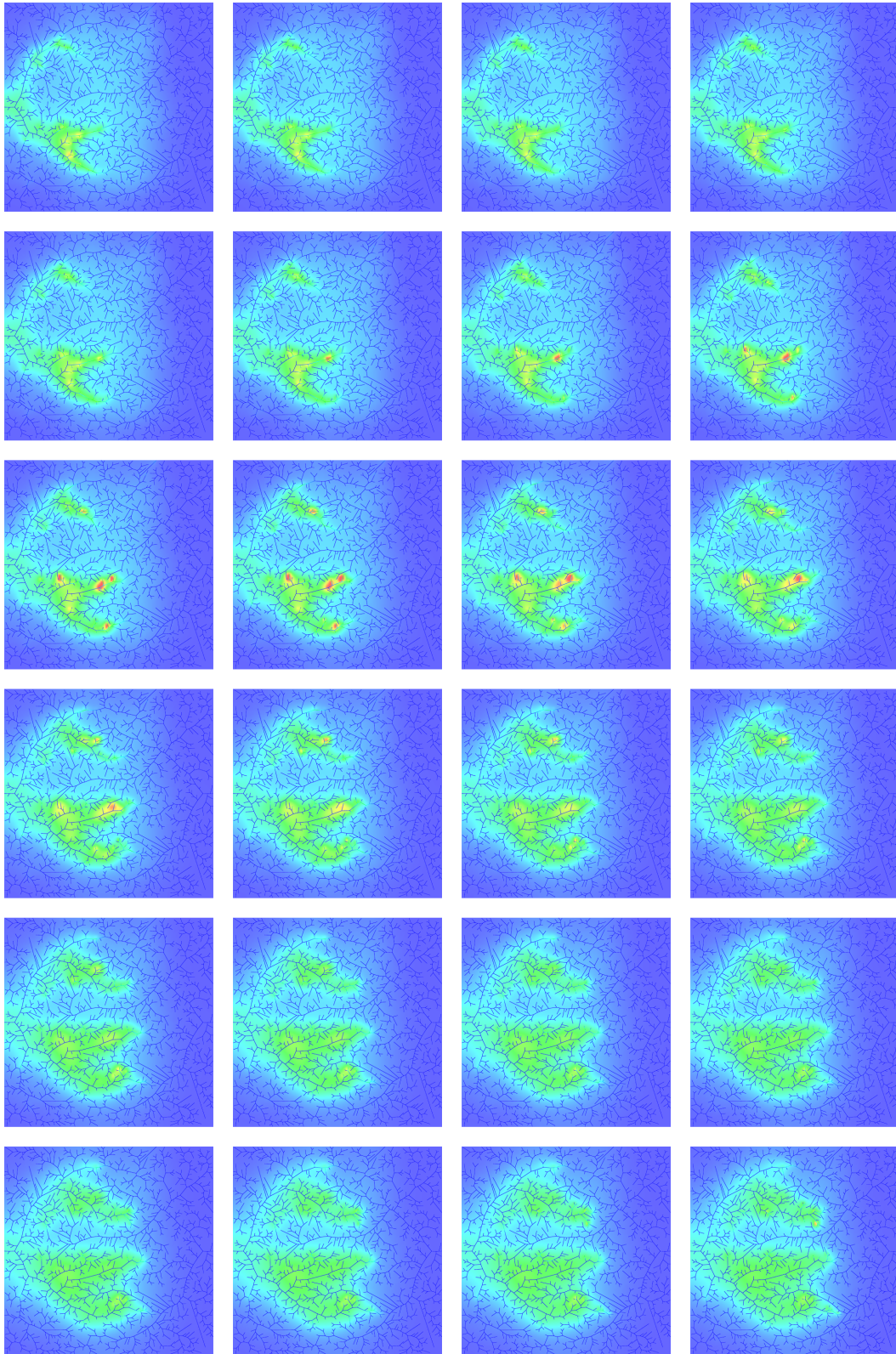


Figure 5.6: Advection-diffusion with pulsed inflow and pulsed velocities on a 1024-tree: Time steps 5440, 5500, . . . , 6760, 6820. These combined plots show temperature in the vessels and temperature in the tissue on two different color scales.

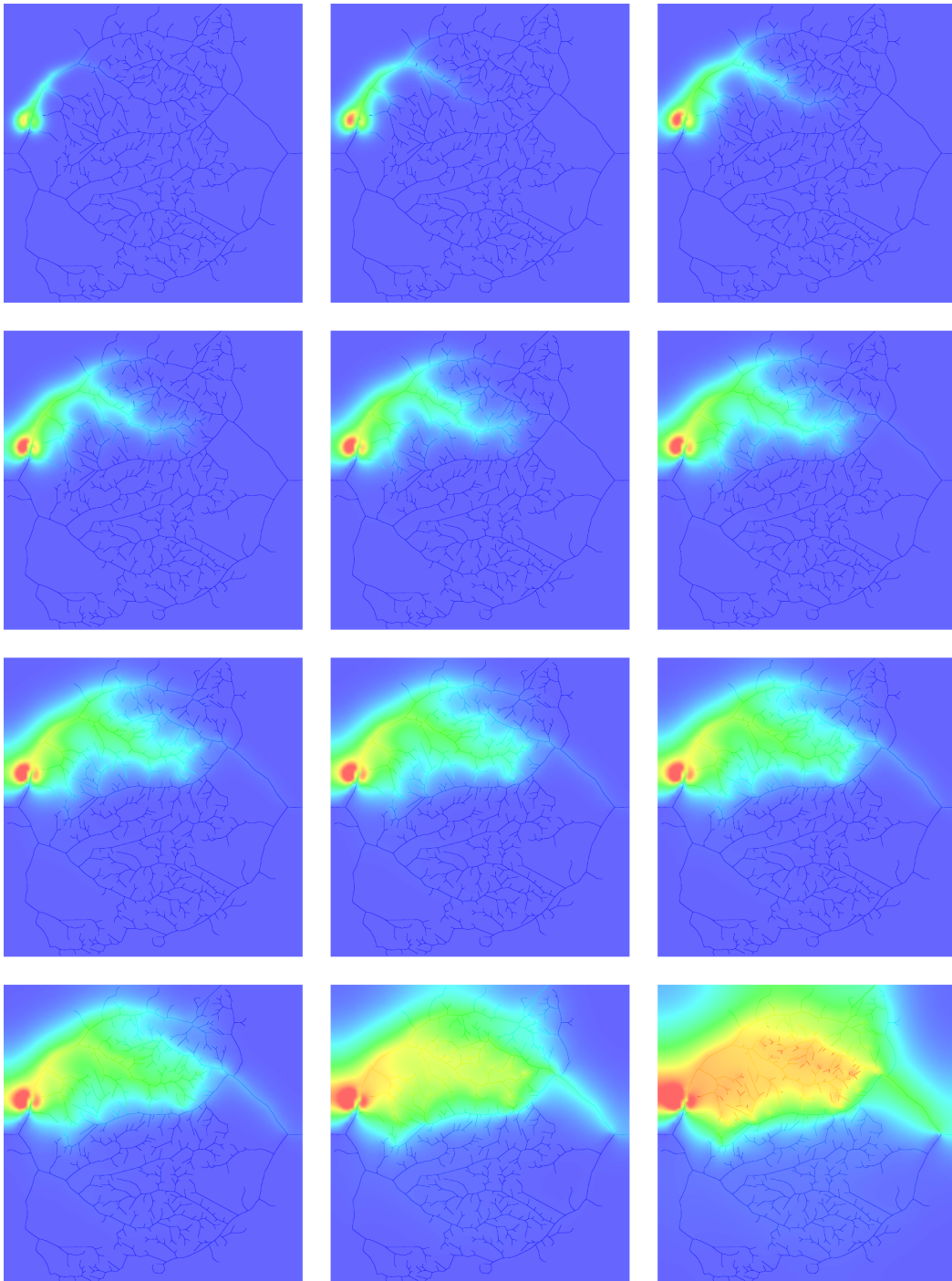


Figure 5.7: Advection-diffusion with a source near the arterial vessel tree and constant velocities on a 1024-tree: Time steps 3000, 6000,  $\dots$ , 27000, 30000, 50000, 90000. These combined plots show temperature in the vessels and in the tissue on the same color scale.

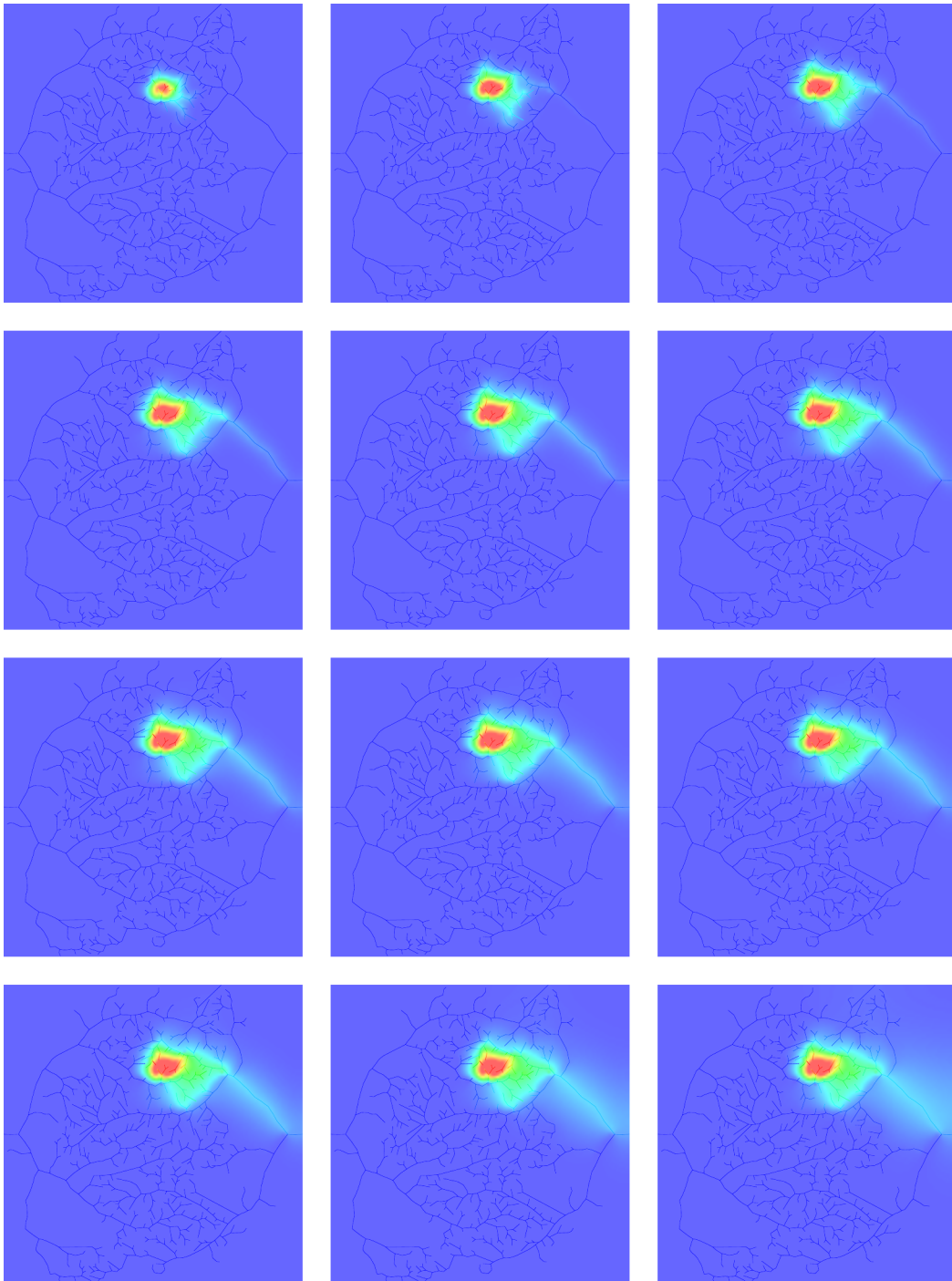


Figure 5.8: Advection-diffusion with a source near the center of the tissue and constant velocities on a 1024-tree: Time steps 3000, 6000, . . . , 27000, 30000, 50000, 90000. These combined plots show temperature in the vessels and in the tissue on the same color scale.

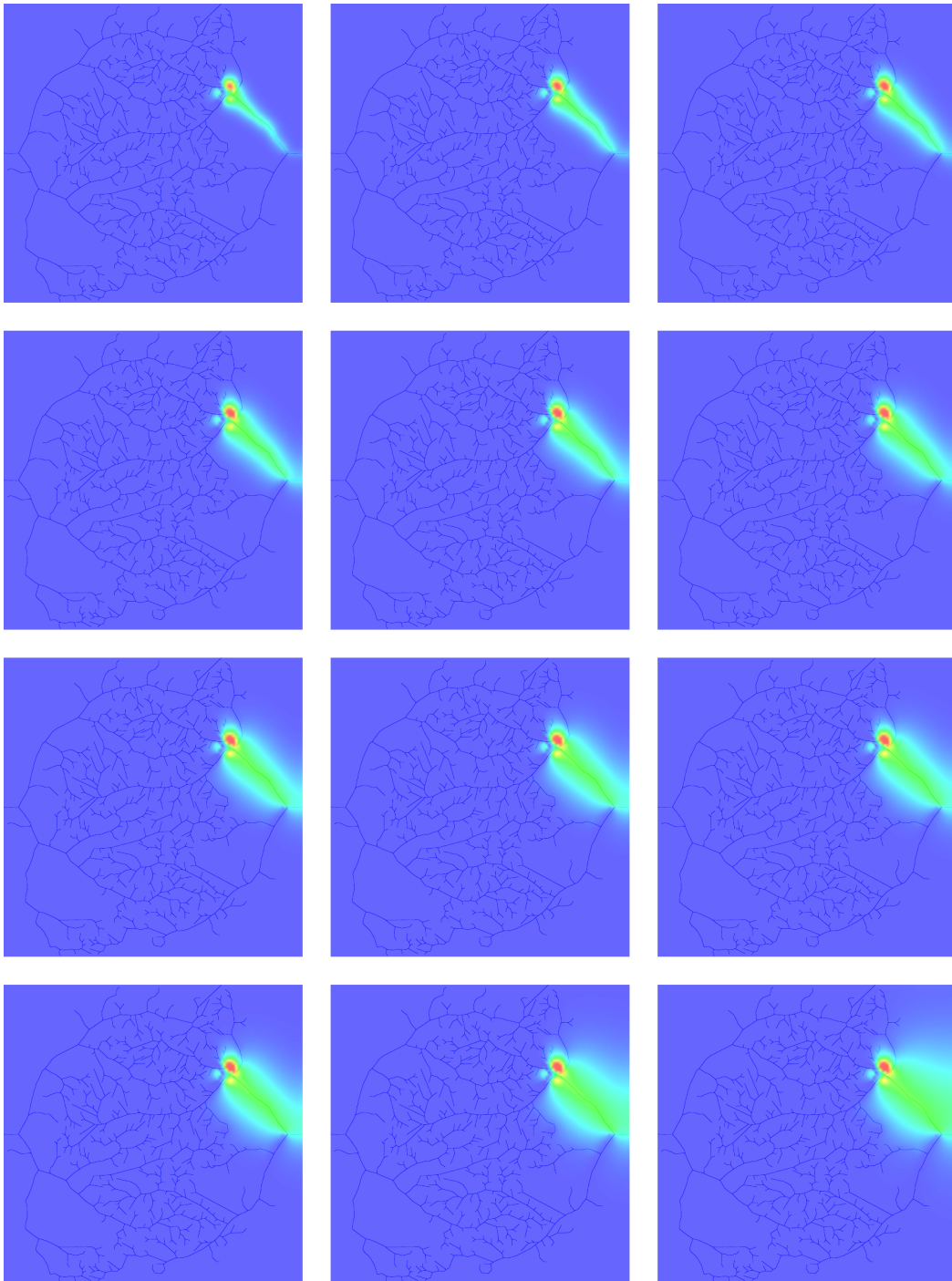


Figure 5.9: Advection-diffusion with a source near the venous vessel tree and constant velocities on a 1024-tree: Time steps 3000, 6000,  $\dots$ , 27000, 30000, 50000, 90000. These combined plots show temperature in the vessels and in the tissue on the same color scale.

test case	16 term segm cputime (s) per time step	512 term segm cputime (s) per time step
1	0.266	2.83
2	0.330	3.41
3	0.300	2.83
4	n/a	2.91
5	0.322	2.81

Table 5.1: cputime per time step of the advection-diffusion simulation

In Table 5.1, we compared how long the computation of one time step of our computation took in the five different cases on a desktop PC with 1 GHz Athlon CPU. The actual calculations here were performed on several PCs at the INS, University of Bonn. For comparison, this table also shows computation times for the same scenarios with a pair of 16-trees.

More time steps of these calculations were combined to video clips that are available on the INS web page:

<http://numod.ins.uni-bonn.de/people/schwen/advectdiffuse.html>

We also show results of a simulation with probes located in the same positions as above with pulsed flow velocities.

# 6 Mathematical Background

## 6.1 Numerical Integration

**Proposition 6.1.1** (Lobatto's rule).

$$\int_0^1 f(x) \, dx \approx \frac{1}{6}f(0) + \frac{2}{3}f(0.5) + \frac{1}{6}f(1)$$

is exact if  $f$  is a polynomial of order 3, see [7].

*Proof.* Let  $a, b, c, d \in \mathbb{R}$ ,  $f(x) = a + bx + cx^2 + dx^3$  be a polynomial of order three. Then

$$\begin{aligned} \int_0^1 f(x) \, dx &= \int_0^1 a + bx + cx^2 + dx^3 \, dx \\ &= \left[ ax + \frac{1}{2}bx^2 + \frac{1}{3}cx^3 + \frac{1}{4}dx^4 \right]_0^1 \\ &= a + \frac{1}{2}b + \frac{1}{3}c + \frac{1}{4}d \end{aligned}$$

and

$$\begin{aligned} \frac{1}{6}f(0) + \frac{2}{3}f(0.5) + \frac{1}{6}f(1) &= \frac{1}{6}a + \frac{2}{3} \left( a + \frac{1}{2}b + \frac{1}{4}c + \frac{1}{8}d \right) + \frac{1}{6}(a + b + c + d) \\ &= \left( \frac{1}{6} + \frac{2}{3} + \frac{1}{6} \right) a + \left( \frac{2}{6} + \frac{1}{6} \right) b + \left( \frac{2}{12} + \frac{1}{6} \right) c + \left( \frac{2}{24} + \frac{1}{6} \right) d \\ &= a + \frac{1}{2}b + \frac{1}{3}c + \frac{1}{4}d \end{aligned}$$

□

On a different domain of integration  $[\alpha, \beta]$ , the quadrature formula is

$$\int_{\alpha}^{\beta} f(x) \, dx \approx \frac{1}{6} \left[ f(\alpha) + 4 \cdot f\left(\frac{\alpha + \beta}{2}\right) + f(\beta) \right].$$

## 6.2 Sobolev Spaces

### 6.2.1 $L^p$ Spaces

Let  $S$  be any subset of  $\mathbb{R}^n$ ,  $\Omega$  be an open subset of  $\mathbb{R}^n$ . Then define the following function spaces:

$$\begin{aligned}
C^0(S) &:= \{f : S \rightarrow \mathbb{R} \mid f \text{ is continuous on } S\} \\
C^{0,\alpha}(S) &:= \left\{ f : S \rightarrow \mathbb{R} \mid \sup_{x \neq y \in S} \frac{|f(x) - f(y)|}{|x - y|^\alpha} < \infty \right\} && \forall 0 < \alpha \leq 1 \\
C^m(\Omega) &:= \{f : \Omega \rightarrow \mathbb{R} \mid f \text{ is } m \text{ times continuously differentiable on } \Omega\} && \forall m \in \mathbb{N} \cup \{\infty\} \\
C_0^m(\Omega) &:= \{f \in C^m(\Omega) \mid \text{supp } f = K \subset \Omega \text{ is a compact set}\} \\
L^p(\Omega) &:= \left\{ f : \Omega \rightarrow \mathbb{R} \text{ measurable} \mid \|f\|_{L^p(\Omega)} := \left( \int_{\Omega} |f|^p \right)^{\frac{1}{p}} < \infty \right\} && \forall p \in \mathbb{R}, p \geq 1 \\
L^\infty(\Omega) &:= \left\{ f : \Omega \rightarrow \mathbb{R} \text{ measurable} \mid \|f\|_{L^\infty(\Omega)} := \inf_{\lambda(N)=0} \sup_{\Omega \setminus N} |f| < \infty \right\}
\end{aligned}$$

Functions in  $C^{0,\alpha}$  are called *Hölder continuous*, functions in  $C^{0,1}$  are called *Lipschitz continuous*.

For compact sets  $K \subset \mathbb{R}^n$ ,  $C^m(K)$  consists of  $C^m$  functions on the interior of  $K$  for which all partial derivatives up to  $m$ th order have a continuous extension to the boundary. As boundaries of compact sets in  $\mathbb{R}^n$  are sets of ( $n$ -dimensional) measure zero,  $L^p$  spaces on compact sets can also be defined.

We quote the following results from [2, Chapter 1]:

- Lemma 6.2.1.**
1.  $\|\cdot\|_{L^p(\Omega)}$  are norms for  $1 \leq p \leq \infty$ .
  2.  $L^p(\Omega)$  are Banach spaces for  $1 \leq p \leq \infty$ .
  3.  $L^2(\Omega)$  with the scalar product  $(f, g)_{L^2(\Omega)} := \int_{\Omega} fg$  is a Hilbert space.

The following lemma is the imbedding theorem for  $L^p$  spaces over domains with finite volume [1, Thm. 2.8]:

**Lemma 6.2.2.** Let  $\Omega \subset \mathbb{R}^n$  be open and satisfy  $\text{vol } \Omega < \infty$ ,  $1 \leq p \leq q \leq \infty$ . If  $u \in L^q(\Omega)$ , then  $u \in L^p(\Omega)$  and

$$\|u\|_{L^p(\Omega)} \leq (\text{vol } \Omega)^{\frac{1}{p} - \frac{1}{q}} \|u\|_{L^q(\Omega)}$$

### 6.2.2 $H^m$ spaces

Let  $\Omega$  be an open subset of  $\mathbb{R}^n$ ,  $f \in C^\infty(\Omega)$ . Then

$$\int_{\Omega} \partial^s f \cdot \varphi = (-1)^{|s|} \int_{\Omega} f \cdot \partial^s \varphi \quad \forall \varphi \in C_0^\infty(\Omega) \quad (6.1)$$

and all multiindices  $s = (s_1, \dots, s_n)$ ,  $s_i \in \mathbb{N} \cup 0 \quad \forall i \in \{1, \dots, n\}$  where  $|s| = s_1 + \dots + s_n$  and  $\partial^s f = \partial_{x_1}^{s_1} \dots \partial_{x_n}^{s_n} f(x_1, \dots, x_n)$ .

However,  $f$  need not be differentiable (not even continuous) for the right hand side of (6.1) to make sense.

Let

$$H^m(\Omega) := \left\{ f \in L^2(\Omega) \mid \forall |s| \leq m \exists f^{(s)} \in L^2(\Omega) : \int_{\Omega} f \cdot \partial^s \varphi = (-1)^{|s|} \int_{\Omega} f^{(s)} \cdot \varphi \forall \varphi \in C_0^\infty(\Omega) \right\}$$

$H^m(\Omega)$  is called *Sobolev space*<sup>1</sup>,  $f^{(s)}$  is called *weak derivative* of  $f$ .

Here, we identify equivalence classes of functions in  $L^2(\Omega)$  with their representatives.

We quote some results from [2, Chapter 1]:

**Lemma 6.2.3.** 1. If  $f$  is  $C^m$ ,  $f^{(s)} = \partial^s f \forall |s| \leq m$ . So weak derivatives are a generalization of classical derivatives.

2. For  $k \leq m$ , a semi-norm on  $H^m(\Omega)$  is defined:

$$|u|_{k,\Omega} := \sqrt{\sum_{|s|=k} \|f^{(s)}\|_{L^2(\Omega)}^2} \quad (6.2)$$

3. A norm on  $H^m(\Omega)$  is defined by

$$\|u\|_{H^m(\Omega)} := \sqrt{\sum_{|s| \leq m} \|f^{(s)}\|_{L^2(\Omega)}^2} \quad (6.3)$$

4.  $H^m(\Omega)$  with this norm is a Banach space.

5.  $C^\infty(\Omega)$  is a dense subset of  $H^m(\Omega)$ .

The dual of  $H^m$  is denoted  $H^{-m}$  and it is described in [1, Chapter 3]:

**Lemma 6.2.4.** Let  $H^m(\Omega)$  be a Sobolev space as above, then its dual is denoted by  $H^{-m}(\Omega)$ .

$H^m(\Omega)$  is a subspace of  $L^2(\Omega)$ , so  $(L^2(\Omega))' = L^2(\Omega)$  is a subspace of  $H^{-m}(\Omega)$  and for  $f \in L^2(\Omega)$ ,

$$\|f\|_{H^{-m}} = \sup_{0 \neq v \in H^m} \frac{|\int_{\Omega} f v|}{\|v\|_{H^m}}$$

**Definition 6.2.5.**  $\Omega \subset \mathbb{R}^n$  has *Lipschitz boundary* if there is a finite open cover  $\bigcup_{i=0}^n U_i \supset \bar{\Omega}$  such that for each  $i$ ,  $\partial\Omega \cap U_i$  is graph of a Lipschitz continuous function.

A counterexample is a domain with a *cusps*,  $\Omega_2$  in Figure 6.1.

**Definition 6.2.6.**  $\Omega \subset \mathbb{R}^n$  satisfies the *cone condition* if there exists a bounded cone with positive angle that can be moved within the domain to touch each boundary point such that the cone lies inside the domain.

This means that all inner angles are positive. A counterexample is  $\Omega_1$  in Figure 6.1, the complement of a domain with a cusp.

<sup>1</sup>More generally, Sobolev spaces  $H^{m,p}$  can be defined based on  $L^p$  for  $p \neq 2$ . We only use  $H^{m,2}$  spaces and drop the 2.

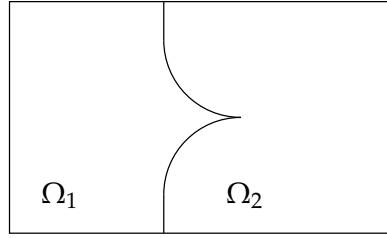


Figure 6.1: A cusp.  $\Omega_1$  does not satisfy the cone condition, both  $\Omega_{1,2}$  do not have Lipschitz boundary.

**Lemma 6.2.7** (A Friedrich's Inequality). *Let  $\Omega \subset \mathbb{R}^n$  be open, satisfy a cone condition and have Lipschitz boundary. Then for  $v \in H^1(\Omega)$ ,*

$$\|v\|_{L^2(\Omega)} \leq C(\bar{v} + |v|_{1,\Omega}) \quad (6.4)$$

where  $\bar{v} = \frac{1}{\text{vol}\Omega} \int_{\Omega} v$  and  $C$  only depends on  $\Omega$ .

*Proof.* For a proof, we refer to [5, Section II.1]. □

**Lemma 6.2.8** (Hölder's Inequality). *Let  $\Omega \subset \mathbb{R}^n$  be open and bounded,  $u, v \in L^2(\Omega)$ . Then*

$$\left( \int_{\Omega} |u(x)v(x)| \, dx \right) \|uv\|_{L^1(\Omega)} \leq \|u\|_{L^2(\Omega)} \cdot \|v\|_{L^2(\Omega)}. \quad (6.5)$$

*Proof.* For a more general form of Hölder's inequality and a proof, we refer to [3, Chapter 1]. □

**Proposition 6.2.9** (Continuity of Sobolev functions). *Let  $\Omega \subset \mathbb{R}^n$  open and bounded with  $\partial\Omega$  Lipschitz,  $m \geq 1$ .*

*If  $m - \frac{n}{2} > k \in \mathbb{N} \cup \{0\}$ , there is an embedding of  $H^m(\Omega)$  into  $C^k(\bar{\Omega})$ .*

*Proof.* For a proof, we refer to [2, Chapter 8]. □

In particular,  $H^m, m \geq 1$ , functions in dimension  $n = 1$  have continuous representatives and  $H^m$  spaces can be defined on compact sets in 1D.

**Definition 6.2.10.** Let  $H$  be a Hilbert space,  $a : H \times H \rightarrow \mathbb{R}$  bilinear.  $a$  is *coercive* if there exist  $C > 0, c > 0$  such that

1.  $a(u, v) = a(v, u)$  (symmetric)
2.  $|a(u, v)| \leq C\|u\|_H\|v\|_H \quad \forall u, v \in H$  (continuous)
3.  $a(v, v) \geq \alpha\|v\|_H^2 \quad \forall v \in H$  (elliptic)

**Proposition 6.2.11** (Lax-Milgram Theorem for convex sets). *Let  $H$  be a Hilbert space,  $V \subset H$  closed and convex,  $a : H \times H \rightarrow \mathbb{R}$  bilinear and coercive,  $l : H \rightarrow \mathbb{R}$  linear and continuous. Then*

$$J(v) := \frac{1}{2}a(v, v) - l(v) \longrightarrow \min! \quad (6.6)$$

*has a unique solution  $v^* \in V$ .*

*Proof.* For a proof, we refer to [5, Section II.2].  $\square$

**Proposition 6.2.12** (Trace Theorem). *Let  $\Omega \subset \mathbb{R}^n$  be an open, bounded set with  $\partial\Omega$  Lipschitz.*

*Then there is a unique linear mapping  $B : H^1(\Omega) \rightarrow L^2(\partial\Omega)$  such that  $Bu = u|_{\partial\Omega}$  for  $u \in H^1(\Omega) \cap C^0(\bar{\Omega})$ .*

*Proof.* For a proof, we refer to [2, Section A5].  $\square$

So Sobolev functions have boundary values in  $L^2$  sense. For continuous functions on the closure of  $\Omega$ , these coincide with classical boundary values.

We need the following inequalities:

**Lemma 6.2.13.** *Let  $f \in C^\infty(0, \ell) \cap C^0([0, \ell])$  for some  $0 < \ell \in \mathbb{R}$ . Then*

1.  $\|f\|_{L^2(0, \ell)} \geq \frac{1}{\sqrt{\ell}} \|f\|_{L^1(0, \ell)}$
2.  $\|f'\|_{L^2(0, \ell)} \geq \frac{1}{\sqrt{\ell}} |f(\ell) - f(0)|$
3.  $\|f\|_{H^1(0, \ell)}^2 \geq \frac{1}{\ell} \left[ \|f\|_{L^1(0, \ell)}^2 + |f(\ell) - f(0)|^2 \right]$

*This lemma also holds for intervals  $[a, a + \ell]$ ,  $a \in \mathbb{R}$ .*

*Proof.* 1. By Lemma 6.2.2 we have

$$\begin{aligned} \|f\|_{L^1(0, \ell)} &\leq \text{vol}([0, \ell])^{\frac{1}{2}-\frac{1}{2}} \|f\|_{L^2(0, \ell)} \\ &= \sqrt{\ell} \|f\|_{L^2(0, \ell)} \end{aligned}$$

for  $f \in L^2(0, \ell) \supset C^\infty(0, \ell) \cap C^0([0, \ell])$ , division by  $\sqrt{\ell}$  proves the first inequality.

2. By 1.,

$$\begin{aligned} \|f'\|_{L^2(0, \ell)} &\geq \frac{1}{\sqrt{\ell}} \|f'\|_{L^1(0, \ell)} \\ &= \frac{1}{\sqrt{\ell}} \int_0^\ell |f'| \\ &\geq \frac{1}{\sqrt{\ell}} \int_0^\ell f' \\ &= \frac{1}{\sqrt{\ell}} (f(\ell) - f(0)) \end{aligned}$$

Also,

$$\begin{aligned} \|f'\|_{L^2(0, \ell)} &\geq \frac{1}{\sqrt{\ell}} \|f'\|_{L^1(0, \ell)} \\ &= \frac{1}{\sqrt{\ell}} \int_0^\ell |f'| \\ &\geq \frac{1}{\sqrt{\ell}} \int_0^\ell (-f') \\ &= \frac{1}{\sqrt{\ell}} (f(0) - f(\ell)) \end{aligned}$$

Together,

$$\|f'\|_{L^2(0,\ell)} \geq \frac{1}{\sqrt{\ell}} |f(\ell) - f(0)|$$

3.  $\|f\|_{H^1(0,\ell)}^2 = \|f\|_{L^2(0,\ell)}^2 + \|f'\|_{L^2(0,\ell)}^2$ , then use 1. and 2. to bound these two expressions.  $\square$

**Lemma 6.2.14.** *Let  $f \in C^\infty(0,\ell) \cap C^0([0,\ell])$  for some  $0 < \ell \in \mathbb{R}$ ,  $|g(0)| = \eta$  or  $|g(\ell)| = \eta$  for some  $\eta \geq \tilde{\eta} > 0$ . Then*

$$\|g\|_{H^1(0,\ell)} \geq \min\left(\frac{1}{2\sqrt{\ell}}\eta, \frac{\sqrt{\ell}}{4}\eta\right) \geq \min\left(\frac{1}{2\sqrt{\ell}}\tilde{\eta}, \frac{\sqrt{\ell}}{4}\tilde{\eta}\right) \quad (6.7)$$

*Proof.* Let  $\theta = \frac{\eta}{4}$ . By the preceding Lemma 6.2.13,

$$\|g\|_{H^1(0,\ell)}^2 \geq \frac{1}{\ell}\|g\|_{L^1(0,\ell)}^2 + \|g'\|_{L^2(0,\ell)}^2 \quad (6.8)$$

Now consider two cases:

1.  $\|g\|_{L^1(0,\ell)} \geq \theta\ell$ , then  $\|g\|_{H^1(0,\ell)}^2 \geq \frac{1}{\ell}\|g\|_{L^1(0,\ell)}^2 \geq \frac{1}{\ell}(\theta\ell)^2 = \frac{\ell\eta^2}{16}$ .

2.  $\|g\|_{L^1(0,\ell)} < \theta\ell$ , then  $M := \{x \in [0,\ell] \mid |g(x)| > 2\theta\}$  satisfies  $\text{vol}(M) < \frac{1}{2}\ell$ .

So  $\exists \gamma \in (0,\ell) : |g(\gamma)| = 2\theta$  (intermediate value theorem for continuous function [31]).

$\|g\|_{H^1(0,\ell)}^2 \geq \|g'\|_{L^2(0,\ell)}^2$  and at least one of the following four cases holds:

a)  $g(0) = +\eta, g(\gamma) = +2\theta$ :

$$\begin{aligned} \|g'\|_{L^2(0,\ell)} &\geq \|g'\|_{L^2(0,\gamma)} \\ &\stackrel{(6.2.11(2))}{\geq} \frac{1}{\sqrt{\gamma}}(g(0) - g(\gamma)) \\ &= \frac{1}{\sqrt{\gamma}}(\eta - 2\theta) = \frac{1}{\sqrt{\gamma}}\frac{1}{2}\eta \\ &\geq \frac{1}{2\sqrt{\ell}}\eta \end{aligned}$$

b)  $g(0) = -\eta, g(\gamma) = -2\theta$ :

$$\begin{aligned} \|g'\|_{L^2(0,\ell)} &\geq \|g'\|_{L^2(0,\gamma)} \\ &\stackrel{(6.2.11(2))}{\geq} \frac{1}{\sqrt{\gamma}}(g(\gamma) - g(0)) \\ &= \frac{1}{\sqrt{\gamma}}(-2\theta - (-\eta)) = \frac{1}{\sqrt{\gamma}}\frac{1}{2}\eta \\ &\geq \frac{1}{2\sqrt{\ell}}\eta \end{aligned}$$

$$\text{c) } g(\ell) = +\eta, g(\gamma) = +2\theta:$$

$$\begin{aligned} \|g'\|_{L^2(0,\ell)} &\geq \|g'\|_{L^2(\gamma,\ell)} \\ &\stackrel{(6.2.11(2))}{\geq} \frac{1}{\sqrt{\ell-\gamma}}(g(\ell) - g(\gamma)) \\ &= \frac{1}{\sqrt{\ell-\gamma}}(\eta - 2\theta) = \frac{1}{\sqrt{\ell-\gamma}}\frac{1}{2}\eta \\ &\geq \frac{1}{2\sqrt{\ell}}\eta \end{aligned}$$

$$\text{d) } g(\ell) = -\eta, g(\gamma) = -2\theta:$$

$$\begin{aligned} \|g'\|_{L^2(0,\ell)} &\geq \|g'\|_{L^2(\gamma,\ell)} \\ &\stackrel{(6.2.11(2))}{\geq} \frac{1}{\sqrt{\ell-\gamma}}(g(\gamma) - g(\ell)) \\ &= \frac{1}{\sqrt{\ell-\gamma}}(-2\theta - (-\eta)) = \frac{1}{\sqrt{\ell-\gamma}}\frac{1}{2}\eta \\ &\geq \frac{1}{2\sqrt{\ell}}\eta \end{aligned}$$

$$\text{So, } \|g\|_{H^1(\Omega)}^2 \geq \left(\frac{\eta}{2\sqrt{\ell}}\right)^2 = \frac{\eta^2}{4\ell}.$$

So, either  $\|g\|_{H^1(0,\ell)}^2 \geq \frac{\ell\eta^2}{16}$  or  $\|g\|_{H^1(0,\ell)}^2 \geq \frac{\eta^2}{4\ell}$  which proves the claim.  $\square$

**Lemma 6.2.15.** For  $a, b \in \mathbb{R}, \delta = a + b > 0, |a| \geq \frac{\delta}{2}$  or  $|b| \geq \frac{\delta}{2}$ .  
For  $a, b, c \in \mathbb{R}, \delta = a + b + c > 0, |a| \geq \frac{\delta}{3}, |b| \geq \frac{\delta}{3}$  or  $|c| \geq \frac{\delta}{3}$ .

## 6.3 Finite Elements

For the discretization of the interval  $[0, 1]$  in one space dimension, we use equidistant grids with grid spacing  $h = \frac{1}{N}$ , i. e.  $x_j = jh$  and piecewise linear nodal basis functions satisfying  $\varphi_i(x_j) = \delta_{ij}$ .

Typically, the number of unknowns is of the form  $N = 2^g + 1$  where  $g$  is the grid level.

For  $[0, 1] \times [0, 1]$  in two space dimensions, we use an equidistant grid in both directions, order the grid points lexicographically, and use piecewise bilinear nodal basis functions, again satisfying  $\varphi_i(x_j) = \delta_{ij}$ .

These basis functions form a partition of unity.

In finite element framework, a *mass matrix*  $M$  and *stiffness matrix*  $L$  are defined

$$\begin{aligned} M &= \left( \int_{\Omega} \varphi_i \varphi_j \right)_{i,j=0,\dots,N} \\ L &= \left( \int_{\Omega} \nabla \varphi_i \nabla \varphi_j \right)_{i,j=0,\dots,N} \end{aligned}$$

where  $\Omega$  is the domain discretized.

In 1D,

$$M = h \begin{bmatrix} 2 & 1 & & & \\ 1 & 4 & 1 & & \\ & \ddots & \ddots & \ddots & \\ & & 1 & 4 & 1 \\ & & & 2 & 1 \end{bmatrix}$$

$$L = \frac{1}{h} \begin{bmatrix} 1 & -1 & & & \\ -1 & 2 & -1 & & \\ & \ddots & \ddots & \ddots & \\ & & -1 & 2 & -1 \\ & & & -1 & 1 \end{bmatrix}$$

*Remark 6.3.1.* 1. In higher space dimension  $d$ ,  $M$  and  $L$  have a more complex sparsity structure depending on the ordering of the unknowns.  $M$  scales with  $h^d$ ,  $L$  with  $h^{d-2}$ .

2.  $M$  and  $L$  matrices are symmetric, which can be seen immediately in the definition.
3. Like in the proof of Lemmas 4.3.2 and 4.3.4, using the definition of positive definiteness and combining terms such that only squared terms remain, it can be seen easily that  $M$  is positive definite. This is also true in higher space dimensions.
4. Multiplying  $L$  with the all-ones vector, it can be seen that  $L$  is singular. This is also true in higher space dimensions.
5. The eigenvalues of  $L$  are the eigenvalues of the negative Laplacian corresponding to those eigenfunctions of the Laplacian that can be represented on the grid [19]. So  $L$  is positive semi-definite and the zero eigenvalue has multiplicity 1.

## 7 Conclusions and Outlook

We have seen that our finite element method for 2D heat diffusion works well for sources given on 1D line segments.

The ELLAM for transport in 1D on a branching structure also works well unless there are discontinuities. In the medical application, initial data is continuous, so most of the problems we have seen do not arise. Discontinuities in the combination of flow do arise due to the nature of the problem, numerical effects of this may have to be dealt with.

Many aspects in the models used here can be refined to obtain more realistic model of the physical and medical effects.

- The structure of the vessels and vessel trees can be refined:
  - Real blood vessels are curved, this can be approximated either by using several line segments and connecting them by monofurcations or by curved segments. The authors of [18] suggest cubic splines for this purpose.
  - Multifurcations can be allowed rather than successive bifurcations with short segments—if this is realistic or useful in some way.
  - The cross section area can vary along the segment.
  - The segments can be viewed as 2D / 3D tubes rather than 1D line segments.
  - The inner structure of the flow within the blood vessels can be modeled more accurately [12]
- In the blood vessels, diffusion can be modeled in addition to advection. Also for advection-diffusion in 1D vessels, ELLAM can be used [11], convergence for this type of method is treated in [36].
- In the tissue, advection can be modeled in addition to diffusion. ELLAM for 2D advection-diffusion is treated in [38].
- The 2D tree generation and flow velocity determination could be extended and the optimization methods used can be improved, but this is not necessary as we want to use real vessel trees in 3D for calculations.
- The methods have to be extended to three-dimensional tissue and vessel trees in 3D where the shape of the domain and boundary effects need to be adapted to the anatomy.
- Material parameters of tissue and vessels vary nonlinearly depending on temperature. For temperatures higher than a certain threshold, proteins start to coagulate [26, 25], which is an irreversible process and changes their material properties, at even higher temperatures, nitrogen and water vaporize.
- Heating by the RF probe can be modeled more accurately [16]. Also, a response of the body to this heating, e. g. an increase in blood flow, can be taken into consideration.

## 7 *Conclusions and Outlook*

- As always in numerical simulations, the more computing resources are available, the finer the discretization and the more accurate the simulation can be.
- Finally, the simulations need to be validated by experiments.

# Acknowledgements

I would like to thank my advisor, Prof. Martin Rumpf at the Institute for Numerical Simulation (INS), University of Bonn, for his help with this thesis.

Also, I am grateful to Dr. Tobias Preusser at MeVis in Bremen for long discussions about ELLAM and the advection problem and Dipl.-Math. Martin Lenz at INS who could always help me with questions concerning c++ programming and the quocmesh library.

Finally, I would like to thank Dipl.-Math. Benjamin Berkels at INS for many critical comments about a draft of this thesis.



# Bibliography

- [1] Robert A. Adams. *Sobolev Spaces*. Academic Press, New York / San Francisco / London, 1975.
- [2] Hans Wilhelm Alt. *Lineare Funktionalanalysis*. Springer, Berlin / Heidelberg, 1992.
- [3] Kendall Atkinson and Weimin Han. *Theoretical Numerical Analysis*. Springer, New York / Berlin / Heidelberg, 2001.
- [4] Dimitri P. Bertsekas. *Nonlinear Programming*. Athena Scientific, Belmont, MA, 2nd edition, 1999.
- [5] Diedrich Braess. *Finite Elemente*. Springer, Berlin / Heidelberg / New York, 1997.
- [6] Achi Brandt. Multi-level adaptive solutions to boundary-value problems. *Mathematics of Computation*, 31(138):333–390, 1977.
- [7] I. N. Bronštein, K. A. Semendjajew, Gerhard Musiol, and Heiner Mühlig. *Taschenbuch der Mathematik*. Harri Deutsch, Thun / Frankfurt (Main), 2001.
- [8] M. A. Celia, T. F. Russell, I. H. Herrera, and R. E. Ewing. An Eulerian-Lagrangian localized adjoint method for the advection-diffusion equation. *Adv Water Resources*, 13(4):187–206, 1990.
- [9] Richard Courant, Kurt Friedrichs, and Hans Levy. über die partiellen Differenzgleichungen der Mathematischen Physik. *Math. Ann.*, 100(1):32–7, 1928.
- [10] E. Cuthill and J. McKee. Reducing the bandwidth of sparse symmetric matrices. In *Proc. 24th Nat. Conf. Assoc. Comput. Mach.*, pages 157–172. ACM Publ., 1969.
- [11] Helge K. Dahle, Richard E. Ewing, and Thomas F. Russell. Eulerien-Lagrangian localized adjoint methods for a nonlinear advection-diffusion equation. *Comput. Methods Appl. Mech. Engrg.*, 122(3-4):223–250, 1995.
- [12] Luca Formaggia, Daniele Lamponi, and Alfio Quarteroni. One-dimensional models for blood flow in arteries. *Journal of Engineering Mathematics*, 47:251–276, 2003.
- [13] Horst Karl Hahn. Makroskopische Morphometrie und Dynamik der Lebergefäße des Menschen. Diploma thesis, Mevis, University of Bremen, 1999.
- [14] Magnus R. Hestenes and Eduard Stiefel. Methods of conjugate gradients for solving linear systems. *Journal of Research of the National Bureau of Standards*, 49(6):409–436, 1952.
- [15] Harro Heuser. *Gewöhnliche Differentialgleichungen*. Teubner, Stuttgart, 3rd edition, 1995.

- [16] Medit K. Jain and Patrick D. Wolf. A three-dimensional finite element model of radiofrequency ablation with blood flow and its experimental validation. *Annals of Biomedical Engineering*, 28:1075–1084, 2000.
- [17] A. N. T. J. Kotte, G. M. J van Leeuwen, and J. J. W Lagendijk. Modelling the thermal impact of a discrete vessel tree. *Phys. Med. Biol.*, 44:57–74, 1999.
- [18] Alexis Kotte, Gerard van Leeuwen, Jacob de Bree, John van der Koijk, Hans Crezee, and Jan Langendijk. A description of discrete vessel segments in thermal modelling of tissue. *Phys. Med. Biol.*, 41:865–884, 1996.
- [19] Randall J. LeVeque. Finite difference methods for differential equations. Course Notes for AMath 585, 586, University of Washington, Seattle, 2004.
- [20] Florian Liehr. Ein effizienter Löser für elastische Mikrostrukturen. Diploma thesis, University Duisburg, 2004.
- [21] Franz Locher. Numerische Mathematik I. Studententext 1271, FernUniversität Hagen, 1989.
- [22] Roberto Maass-Moreno and Carl F. Rothe. Distribution of pressure gradients along hepatic vasculature. *Am. J. Physiol. (Heart. Circ. Physiol.)*, 272, Issue 6(41):H2826–H2832, 1997.
- [23] Friederike Neumann, Wolfgang Schreiner, and Martin Neumann. Computer simulation of coronary arterial trees. *Advances in Engineering Software*, 28:353–357, 1997.
- [24] Felix Otto. The geometry of dissipative evolution equations: the porous medium equation. *Comm. Partial Differential Equations*, 26(1-2):101–174, 2001.
- [25] Tobias Preusser, H-O Peitgen, Florian Liehr, Martin Rumpf, Ulrich Weikard, and Stefan Sauter. Simulation of radio-frequency ablation using composite finite element methods. In *Proceedings of the Scientific Workshop Medical Robotics, Navigation and Visualization. RheinAhr-Campus Remagen*, 2004.
- [26] Tobias Preusser, Andreas Weihusen, and Heinz-Otto Peitgen. On the modelling of perfusion in the simulation of RF-ablation. In *Proceedings of Simulation and Visualization (SimVis)*, Magdeburg, 2005.
- [27] Alfio Quarteroni and A. Valli. *Numerical Approximation of Partial Differential Equations*. Springer, Berlin / New York, 1994.
- [28] R. Tyrell Rockafellar. *Network Flows and Monotropic Optimization*. Athena Scientific, Belmont, MA, 1998.
- [29] Thomas F. Russel and Michael A. Celia. An overview of research on Eulerian-Lagrangian localized adjoint methods (ELLAM). *Advances in Water Resources*, 25:1215–1231, 2002.
- [30] Wolfgang Schreiner, Martin Neumann, Friederike Neumann, Susanne M. Roedler, Adelheid End, P. Buxbaum, Michael R. Müller, and Paul Spieckermann. The branching angles in computer-generated optimized models of arterial trees. *J. Gen. Physiol.*, 105:975–989, 1994.

- [31] W. I. Smirnow. *Lehrgang der Höheren Mathematik, Teil 1*. VEB Deutscher Verlag der Wissenschaften, Berlin, 1960.
- [32] Joel Smoller. *Shock Waves and Reaction-Diffusion Equations*. Springer, New York / Heidelberg / Berlin, 1983.
- [33] Ulrich Trottenberg, Cornelis Osterlee, and Anton Schüller. *Multigrid*. Academic Press, San Diego / London, 2001.
- [34] Supan Tungjitkusolmun, S. Tyler Staelin, Dieter Haemmerich, Jan-Zern Tsai, Hong Cao, John G. Webster, Fred T. Lee Jr., David M. Mahvi, and Vicken R. Vorperian. Three-dimensional Finite-Element analyses for radio-frequency hepatic tumor ablation. *IEEE Transactions on Biomedical Engineering*, 49(1):3–9, 2002.
- [35] W. J. Vankan, J. M Huyghe, J. D Janssen, A. Huson, W. J. G Hacking, and W. Schreiner. Finite element analysis of blood flow through biological tissue. *Int. J. Engng. Sci.*, 35(4):375–385, 1997.
- [36] Hong Wang. A family of ELLAM schemes for advection-diffusion-reaction equations and their convergence analyses. *Numer Meth PDE*, 14:739–780, 1998.
- [37] Hong Wang. An optimal-order error estimate for an ELLAM scheme for two-dimensional linear advection-diffusion equations. *SIAM J Numer Anal*, 37(4):1338–1368, 2000.
- [38] Hong Wang, Helge K. Dahle, Richard E. Ewing, Magne S. Espedal, Robert C. Sharpley, and Shushuang Man. An ELLAM scheme for advection-diffusion equations in two dimensions. *SIAM Journal on Scientific Computing*, 20(6):2160–2194, 1999.
- [39] M Zamir. Nonsymmetrical bifurcations in arterial branching. *J. Gen. Physiol.*, 72:837–845, 1978.
- [40] M Zamir. The branching structure of arterial trees. *Comments Theor. Biol.*, 1(1):15–37, 1988.
- [41] Liang Zhu and Sheldon Weinbaum. A model for heat transfer from embedded blood vessels in two-dimensional tissue preparation. *J Biomech Engrg*, 117:64–73, 1995.

## *Bibliography*

# Index

- $C^m$  space, 118
- $C^{0,\alpha}$  space, 118
- $L^p$  space, 118
- $n$ -tree, 9
  
- advection equation, 45
- alpha mask, 104
- apparent cross section area, 84
- arcs, 7
- Armijo step size rule, 13, 23
- arterial tree, 8
  
- Backward Euler time stepping, 34
- Banach space, 118
- banded solvers, 77
- binary tree, 7
  
- capillaries, 99
- CFL condition, 80
- coercive, 120
- conditional gradient method, 22
- cone condition, 119
- conjugate gradient solver, 38
- constrained constructive optimization, 13
- continuous, 120
- convex polyhedron, 23
- cross section area, 9
- cusp, 119
- Cuthill-McKee algorithm, 78
  
- daughter segment, 7
- descent direction, 22
- diagonally preconditioned conjugate gradient solver, 38
- diameter, 9
- directed graph, 7
- dissipation, 19, 21
- dual space, 32
  
- ELLAM, 43, 48
  
- elliptic, 120
- energy content, 43
- explicit, 104
  
- feasible direction, 22
- feasible direction method, 22
- fill-in, 78
- flow splitting ratio, 9
- flow splitting ratios, 43
- Frank-Wolfe method, 22
- friction, 19, 21
- Friedrich's inequality, 120
  
- Gaussian bell curve, 78
- Gaussian elimination, 62, 77
- grid spacing in domain, 19
- grid spacings on tree, 91
  
- Hölder continuous, 118
- Hölder space, 118
- Hölder's inequality, 120
- heat conduction, 31
- heat equation, 31
- heat transmittivity, 98
- Hilbert space, 118
- homogeneous blood supply, 11
- hsv transition, 29
  
- initial guess, 22
- isotropic heat conduction, 31
  
- kinetic energy, 19, 21
  
- Lagrange multiplier, 37
- Lax-Milgram theorem, 36, 120
- level of domain discretization, 19
- level of node, 8
- level of tree discretization, 91
- linear convergence, 24
- linear optimization problem, 23
- Lipschitz boundary, 119

- Lipschitz continuous, 118
- liver carcinoma, 5
- Lobatto quadrature, 35
- Lobatto's rule, 117
  
- mass conservation, 43
- mass matrix, 123
- multigrid methods, 24
- multiplicity, 7
  
- node, 8
  - initial, 7
  - terminal, 7
- nodes, 7
- numerical diffusion, 80
- numerical dissipation, 80
  
- parent segment, 7
- path, 7
- pnmcomp, 104
- polyhedron, 23
- porous medium, 20
- pressure, 20
- prolongation, 24
  
- restriction, 24
- RF ablation, 5
- RF probe, 5
- root, 7
- root segment, 8
  
- segment, 8
- siblings, 7
- Sobolev space, 119
- spd matrix, 69
- steady state, 36
- steepest descent method, 13
- stiffness matrix, 123
- symmetric, 120
  
- terminal node, 8
- terminal segment, 8
- trace theorem, 121
- tree, 10
  
- valid pair of trees, 9
- venous tree, 8
- vertex, 23
- vessel tree, 8
  
- weak derivative, 119

**Erklärung gemäß §19(8) der Diplomprüfungsordnung für den integrierten Studiengang  
Mathematik / Wirtschaftsmathematik / Technomathematik vom 10. Dezember 1996**

Ich versichere, dass ich diese Arbeit selbständig verfasst und keine anderen als die angegebenen Quellen und Hilfsmittel benutzt sowie Zitate kenntlich gemacht habe.

Duisburg, 15. November 2005

Lars Ole Schwen